

***Ab initio* based spectroscopic and reactive studies of small
molecular systems**

I n a u g u r a l d i s s e r t a t i o n

zur

Erlangung des akademischen Grades

doctor rerum naturalium (Dr. rer. nat.)

an der Mathematisch-Naturwissenschaftlichen Fakultät

der

Ernst-Moritz-Arndt-Universität Greifswald

vorgelegt von

Robert Warmbier

geboren am 28.08.1984

in Stralsund, Deutschland

Greifswald, 05.05.2011

Dekan: Prof. Dr. rer. nat. Klaus Fesser
1. Gutachter: Prof. Dr. rer. nat. Ralf Schneider
2. Gutachter: Prof. Mario Capitelli
Tag der Promotion: 07.06.2011

Ex Astris Scientia

—

Contents

1	Introduction	1
2	Basic Physics and Methods	5
2.1	<i>Ab initio</i> quantum mechanics	5
2.1.1	Born-Oppenheimer and adiabatic approximations	6
2.1.2	Self-Consistent Field Hartree-Fock	8
2.1.3	Basis functions	14
2.1.4	Post-Hartree-Fock methods	15
2.1.4.1	Excited Slater determinants	16
2.1.4.2	Configuration Interaction	16
2.1.4.3	Coupled Cluster theory	18
2.1.4.4	Multi-reference techniques	20
2.2	Potential energy surface	21
2.2.1	Internuclear distance coordinates	22
2.2.2	Potential representation	22
2.2.3	Fitting	24
2.2.4	Dipole moment surface	26
2.3	Lagrange-Mesh Method	26
2.4	Recap	29
3	Potential energy surfaces for small hydrocarbons	31
3.1	Choice of <i>ab initio</i> method	32
3.2	Potential energy surfaces	34
3.3	Application	40
3.3.1	CH ₃	41
3.3.2	CH ₄	43
3.4	Recap	48

4	Spectroscopic and photodissociation studies of magnesium hydride	49
4.1	Methods	49
4.1.1	Choice of <i>ab initio</i> method	50
4.1.2	Lagrange Mesh Solver for the molecular Schrödinger equation	51
4.1.3	Radiative oscillator strength and photodissociation cross sections	55
4.2	Results	55
4.2.1	<i>Ab initio</i>	55
4.2.2	Rovibrational states	62
4.2.3	Spectroscopic data	64
4.2.4	Photodissociation	70
4.3	Recap	72
5	Reactive studies of the Methylidyne cation	75
5.1	Properties of the CH_2^+ reactive system	76
5.2	Methods	78
5.2.1	Choice of <i>ab initio</i> method	78
5.2.2	Potential energy surface	80
5.2.3	Dynamics	81
5.2.4	ABC: quantum reactive scattering	86
5.3	Results	86
5.3.1	Potential energy surface	86
5.3.2	Sensitivity studies for the potential energy surface	91
5.3.3	Cross sections	93
5.3.3.1	Comparative study of QCT weightings	93
5.3.3.2	Quasi classical trajectory	94
5.3.3.3	Quantum scattering	101
5.3.4	Rate coefficients	103
5.4	Recap	106
	Conclusions	109
	Appendix A - MgH	111
1	Rovibrational transitions	111
2	Photo dissociation cross sections	112
	Bibliography	123

1 Introduction

There is no older field of physics nor any that has cast its spell over so many people than astronomy. Most physical systems are complex. This includes planetary and stellar atmospheres, interstellar clouds and most other places where small scale molecules can be found. Complex in the sense, that different processes compete and interact with each other and that processes take place at different time and length scales. Depending on the type of a star, it can take many years for the energy produced by fusion in the centre of the star to reach the stars' outer atmosphere. Radiative processes and reactions caused by photons and electrons just take femtoseconds or picoseconds. Furthermore, the physical conditions in astrophysical systems are sometimes beyond our experimental capabilities, e.g. temperatures, pressures, dimensions, magnetic fields. The areas of physics involved include plasma physics, fluid dynamics, chemical physics, electrodynamics and probably many more. Clearly, to understand the large thing, we have to understand the small things first.

The aim of this work is to use computational techniques to calculate molecular data that can be used to improve the understanding of astrophysical systems. Understanding of spectroscopic and reactive behaviour is crucial for many systems of astrophysical interests like stars, interstellar medium and comets. Especially stellar atmospheres are of interest, because the complex physics of stars are not yet completely understood. Stars are in an unstable balance of gravitation and radiation pressure. The atmospheric dynamics have been the subject of extensive modelling. This modelling tries to reproduce the physics of different types of stars. Complete and accurate spectroscopic information of the atoms and molecules in these atmospheres is necessary for this attempt. In addition, the only information we have about astrophysical systems is light which is emitted or absorbed by particles in these media. This is not only true for astrophysics. In plasma physics sometimes the usage of invasive diagnostics, like Langmuir probes, is not wanted because they disturb the system. In these cases some information of the system can be regained by passively measuring infrared spectra of the plasma or by active induction of electronic transition like the laser-induced fluorescence method. Another remote sensing application is the measurement of the atmospheric composition on earth. Here, larger particles

in the atmosphere as well as greenhouse gases are of current interest. Unfortunately, the experimental spectroscopic data, which is needed for the understanding and interpretation of the measured spectra, is often incomplete. This gap can be, to some extent, filled by computational chemical physics.

In this work I use methods of computational chemical physics to study some small molecules and molecular systems of astrophysical interest. The general work flow, as illustrated in figure 1.1, is as follows. First, electronic structure calculations are performed. These give insight into the general bonding behaviour of molecules and offer inherent information about the molecule, like equilibrium configurations, dissociation energies, polarisabilities, ionisation energies, dipole and higher moments etc. In the context of chemical physics the electronic potential and dipole moments are of special interest. These are calculated in a specific region of the configuration space. For spectroscopic purposes the region around the equilibrium configuration is needed. If chemical reactions shall be surveyed, the relevant configuration space is much larger and covers the reagent and product configurations as well as a possible intermediate complex and the whole reaction path in between. The computational time for a point in the configuration space ranges between seconds and hours. The number of configurations included in

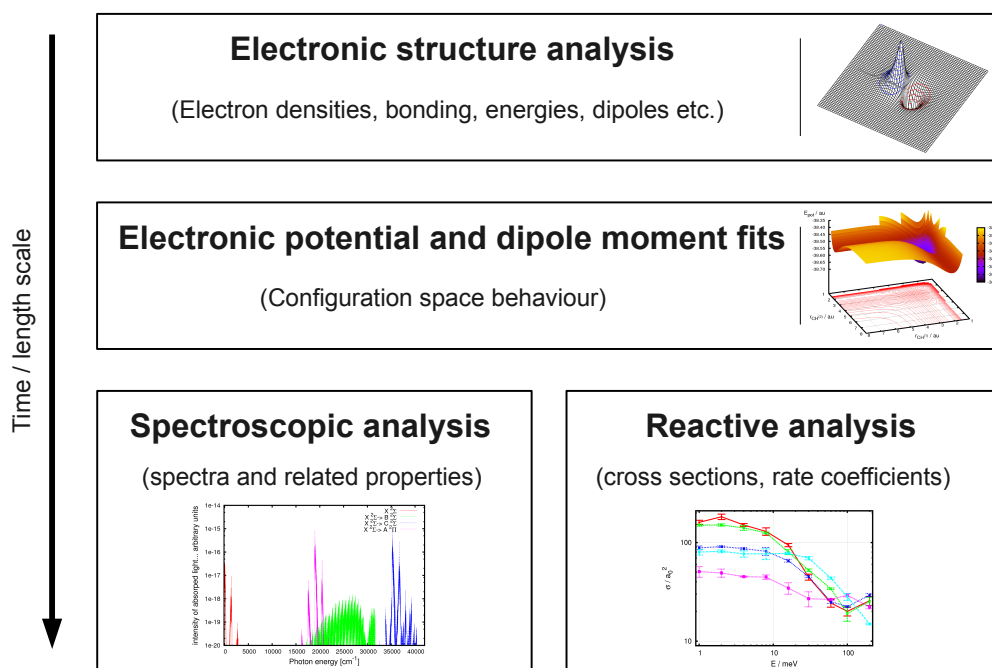


Figure 1.1: Work flow chart for spectroscopic and reactive calculations within this work.

spectroscopic (CH_4) or reaction calculations (CH_2^+) can easily reach the order millions. Naturally an on-the-fly calculation of *ab initio* data is not possible. Therefore, a number of *ab initio* configurations are calculated, which are then fitted to potential energy and dipole moment surfaces. These surfaces become multi-dimensional even for small systems. For example, a potential energy surface of CH_3 has six dimensions, for CH_4 nine or ten, depending on the choice of coordinates. These surfaces become increasingly difficult to construct. Even worse, the diagnostics is difficult for these surfaces. Due to the intrinsic physical and numerical complexity for *ab initio* calculations and the fits, these are the most challenging parts of the work. An introduction to *ab initio* techniques and a description of the surface fitting is given in the second chapter.

Using these techniques, the further procedure depends on the problem at hand. In this work typical tasks are addressed, which can be solved by computational chemical physics. These include infrared rovibrational spectroscopy, rovibronic spectroscopy, photodissociation and reaction dynamics. These calculations are performed for systems of current astrophysical interest.

In the third chapter potential energy surfaces for small hydrocarbons are constructed. The potential surface method used in this work can be applied to local spectroscopic and global reactive surfaces, which are both of interest for hydrocarbons. Small hydrocarbons can be found almost everywhere in the universe. Information about their behaviour is of interest e.g. in astrophysics and plasma physics. This means especially the spectra of these molecules. Obtained by remote sensing, the analysis of the spectra of a plasma or a star compared to the spectra of the molecules inside offers information about abundances, temperatures and pressures in the system. As hydrocarbons are highly reactive, reaction rates are also important for the correct description of chemical equilibria. In the third chapter basic considerations are presented for the choice of *ab initio* methods and the fitting procedure. Capabilities and limitations of the methods at hand are pointed out. The quality of the potential surfaces and their possible application to infrared spectroscopy are shown for CH_3 and CH_4 .

The next chapter shows an implementation of diatomic rovibronic spectroscopy and photodissociation. The spectroscopy is in the energy range of near ultraviolet and visible light. Diatomic metal hydrides and oxides can be found in astrophysical systems. Their absorption lines in stellar atmosphere spectra allow insight into the chemical composition of the atmosphere, temperatures and pressures. Furthermore, they add opacity to the radiation transport simulations. Magnesium hydride (MgH) is chosen for this investigation. There is already numerical data available for the lowest three electronic states of MgH , which are used for validation purposes. The quality of the spectra was considerably improved to previous numerical studies. In addition, two extra electronic states could be included. With these the frequency range could be expanded from visible to

the near ultraviolet region. Tests with atmospheric models show a strong opacity in this region. A higher opacity means less energy transport through the atmosphere and therefore a changed temperature profile. The new line lists allow therefore better modelling of radiation transport in atmospheres, where this molecule is present.

In the last chapter the $\text{H} + \text{CH}^+$ reaction is surveyed. While CH^+ can be found often in interstellar media and comets, its abundance is not fully understood. Motivated by new measurements, which are in conflict with previous numerical studies, I calculated reaction cross sections and rate coefficients. In the standard model the cross sections for the $\text{H} + \text{CH}^+ \rightarrow \text{C}^+ + \text{H}_2$ reaction diverge in the limit of weak collisions and small internal energies. New experimental rate coefficients indicate an inhibited reaction for temperatures well below 50 K. This is contradictory to the standard model. The results achieved in this thesis indicate that previous numerical results overestimated the reaction rates by a factor of two, but they are not able to explain the experimental results either.

The major results are discussed in a final conclusion and a placement of this work for the general physics picture is given.

This work explores the capabilities of computational chemical physics methods in their application to astrophysical relevant systems and questions. The focus was on the application of *ab initio* based fitted potential energy surfaces. Such potentials have been successfully used for the calculation of rovibrational and rovibronic line lists, photodissociation and reaction dynamics. These are four of the most important types of molecular data used in astrophysics and other remote sensing applications.

2 Basic Physics and Methods

This chapter gives introductions into basic physics and methods used in this work. The first part introduces the idea and techniques of *ab initio* quantum mechanics. These are methods, which solve the electronic Schrödinger equation approximately. Secondly, a potential energy surface fitting is introduced, which allows to fit *ab initio* potential energies over the configuration space. At the end, the Lagrange-mesh technique for solving the molecular Schrödinger equation is introduced.

2.1 *Ab initio* quantum mechanics

The inherent properties of molecules, like binding energies, ionization energies, vibrational and rotational motions, dipole moments, polarisability and their thermodynamic behaviour, depend mainly on the electronic configuration and the interaction potentials of all the particles of the molecule. The Schrödinger equation describes non-relativistic quantum systems and is therefore the equation of choice for most molecular systems. This equation can not be solved analytically for more than one electron in the system. Therefore, approximations, like the Born-Oppenheimer approximation, have to be introduced generating numerically solvable equations. The first order solution of the electronic Schrödinger equation, assuming a mean-field potential for the electron-electron interaction, is the Hartree-Fock energy. Improvements to this solution can be done either by adding functionals to the potential descriptions, referred to as density functional theory, or by applying approximative methods to simulate the true electron-electron correlation. The later ones can be referred to as *ab initio* techniques which are discussed in this section. The field of *ab initio* methods is broad and the detailed implementations of the various methods are sophisticated. As these methods are used as tools in this work, only a basic introduction is given. The description will mostly follow Jensen [1], where also more detailed descriptions can be found.

2.1.1 Born-Oppenheimer and adiabatic approximations

A non-relativistic molecular system is described exactly by the complete molecular Schrödinger equation

$$\hat{H}(\mathbf{r}, \mathbf{R})\Psi(\mathbf{r}, \mathbf{R}) = [(\hat{T}_N(\mathbf{R}) + \hat{T}_e(\mathbf{r}) + \hat{V}_{eN}(\mathbf{r}, \mathbf{R}) + \hat{V}_{NN}(\mathbf{R}) + \hat{V}_{ee}(\mathbf{r}))]\Psi(\mathbf{r}, \mathbf{R}), \quad (2.1)$$

where \mathbf{r} and \mathbf{R} are the coordinates of all electrons and nuclei, respectively. $\hat{T}_e(\mathbf{r})$ and $\hat{T}_N(\mathbf{R})$ are the corresponding kinetic energy operators. Besides the electron-electron potential $\hat{V}_{ee}(\mathbf{r})$ and nuclei-nuclei potential $\hat{V}_{NN}(\mathbf{R})$ there is also a term for the interaction of electrons and nuclei: $\hat{V}_{eN}(\mathbf{r}, \mathbf{R})$. While this interaction is not negligible it couples the differential equations for the nuclei and electrons leaving a computationally infeasible task. Nevertheless, approximations to equation (2.1) can be applied. Arguing that the differential operators ∇_e and ∇_N operate roughly over the same dimensions, the ratio of kinetic energies and masses of the particles can be estimated by $\frac{T_N}{T_e} \propto \frac{m_N}{m_e}$. The mass ratio of protons and electrons is roughly 1836. The ratio is getting larger for heavier atoms. Following this fact one can argue further, that the electrons move much faster and therefore immediately adjust to any change of the nuclei configuration. In this picture R can be considered as fixed with $T_N = 0$:

$$\hat{H}_{\text{fixed}}(\mathbf{r}; \mathbf{R})\Psi(\mathbf{r}; \mathbf{R}) = [(\hat{T}_e(\mathbf{r}) + \hat{V}_{eN}(\mathbf{r}; \mathbf{R}) + \hat{V}_{NN}(\mathbf{R}) + \hat{V}_{ee}(\mathbf{r}))]\Psi(\mathbf{r}; \mathbf{R}). \quad (2.2)$$

In equation (2.2) the wave function $\Psi(\mathbf{r}; \mathbf{R}) \approx \Phi_e(\mathbf{r})\Phi_N(\mathbf{R})$ can be separated. Inserting this into equation (2.1) delivers

$$\begin{aligned} & \Phi_e \hat{T}_N \Phi_N + \Phi_N \hat{T}_e \Phi_e + \Phi_N \hat{V}_{ee} \Phi_e + \Phi_N \hat{V}_{NN} \Phi_e + \Phi_N \hat{V}_{eN} \Phi_e \\ & - \left\{ \sum_N \frac{1}{2m_N} (2\nabla_N \Phi_e \nabla_N \Phi_N + \Phi_N \nabla_N^2 \Phi_e) \right\} = E \Phi_e \Phi_N. \end{aligned} \quad (2.3)$$

In the term in curly brackets the kinetic energy operator of the nuclei acts on the electronic wave function. Following again the argument that $\nabla_N \Phi_e$ and $\nabla_e \Phi_e$ give results of similar dimension the factor $\frac{1}{m_N}$ is important. As $m_e/m_N \ll 1$, the term is neglected.

The equations for electrons and nuclei are now completely separated and one has derived the standard equations of the Born-Oppenheimer approximation[2]:

$$\hat{H}_e \Phi_e(\mathbf{r}; \mathbf{R}) = [\hat{T}_e(\mathbf{r}) + \hat{V}_{eN}(\mathbf{r}; \mathbf{R}) + \hat{V}_{NN}(\mathbf{R}) + \hat{V}_{ee}(\mathbf{r})]\Phi_e(\mathbf{r}; \mathbf{R}) = E_e(\mathbf{R})\Phi_e(\mathbf{r}; \mathbf{R}) \quad (2.4a)$$

$$\hat{H}_{\text{tot}} \Phi(\mathbf{R}) = [\hat{T}_N(\mathbf{R}) + E_e(\mathbf{R})]\Phi_N(\mathbf{R}) = E_{\text{tot}} \Phi_N(\mathbf{R}) \quad (2.4b)$$

Within this approximation the nuclei move on a potential energy surface given by the solution of the electronic Schrödinger equation, which is independent of the nuclear masses. In a general system the separation of electronic and nuclear coordinates introduces a mass-polarisation term

$$\hat{H}_{mp} = -\frac{1}{M_{\text{tot}}} \left(\sum_e \nabla_e \right)^2, \quad (2.5)$$

where M_{tot} is the total mass of all the nuclei. Within the Born-Oppenheimer approximation this term can be neglected following the same argument as before.

So far the problem was restricted to one electronic state and the possibility of coupling of electronic states was neglected. Assuming that the full set of solutions of the electronic Schrödinger equation is known. The total wave function can be represented now as

$$\Psi(\mathbf{r}; \mathbf{R}) = \sum_{i=1}^{\infty} \Phi_{ni}(\mathbf{R}) \Phi_i(\mathbf{r}; \mathbf{R}), \quad (2.6)$$

where i are the orthonormal eigenstates of the electronic Schrödinger equation. Using this wave function terms of the kind $\langle \Phi_i | \nabla^2 | \Phi_j \rangle$ may occur. These can be neglected as before in the case of the nuclear momentum operator, leaving the Born-Oppenheimer approximation intact. In the case of the electronic momentum operator, this can not be done ad-hoc and the mass-polarisation has to be included. The total Schrödinger equation takes the form

$$\begin{aligned} \sum_{i=1}^{\infty} [\hat{T}_N + \hat{H}_e + \hat{H}_{mp}] \Phi_{ni} \Phi_i &= E_{\text{tot}} \sum_{i=1}^{\infty} \Phi_{ni} \Phi_i \\ &\vdots \\ \sum_{i=1}^{\infty} \left\{ \sum_N -\frac{1}{2m_N} (\Phi_i \nabla_n^2 \Phi_{ni} + 2 \nabla_n \Phi_i \nabla_n \Phi_{ni} + \Phi_{ni} \nabla_n^2 \Phi_i) + \Phi_{ni} E_i \Phi_i + \Phi_{ni} \hat{H}_{mp} \Phi_i \right\} &= E_{\text{tot}} \sum_{i=1}^{\infty} \Phi_{ni} \Phi_i \end{aligned} \quad (2.7)$$

Multiplying this equation with Φ_j^* and integrating over the electronic coordinates results in

$$\hat{T}_n \Phi_{nj} + E_j \Phi_{nj} + \sum_{i=1}^{\infty} \left\{ \sum_N -\frac{1}{2m_N} (2 \langle \Phi_j | \nabla_n | \Phi_i \rangle \nabla_n \Phi_{ni} + \langle \Phi_j | \nabla_n^2 | \Phi_i \rangle \Phi_{ni}) + \langle \Phi_j | \hat{H}_{mp} | \Phi_i \rangle \Phi_{ni} \right\} = E_{\text{tot}} \Phi_{nj} \quad (2.8)$$

The nuclear kinetic energy and electronic energy terms are the same as before. The first and second term in brackets are the first- and second-order non-adiabatic coupling elements.

In the adiabatic approximation, the total wave function is restricted to one electronic

surface and the off-diagonal coupling elements are zero. The diagonal first-order non-adiabatic coupling constants are zero, except for spatially degenerate wave functions. In the adiabatic approximation also the mass-polarisation can be neglected leaving

$$\left(\hat{T}_n + E_j + \sum_N -\frac{1}{2m_N} \langle \Phi_j | \nabla_n^2 | \Phi_j \rangle \right) \Phi_{nj} = E_{\text{tot}} \Phi_{nj}. \quad (2.9)$$

The difference between the adiabatic and the Born-Oppenheimer approximation is now the diagonal second-order correction. It is roughly $\frac{m_N}{m_e}$ smaller than E_e , as the other neglected terms. Therefore, it is reasonable to stay with the Born-Oppenheimer approximation for most cases.

Although both approximations are very reliable for most cases they break down where two or more solutions of the electronic Schrödinger equation have similar energies.

2.1.2 Self-Consistent Field Hartree-Fock

In order to solve the electronic Schrödinger equation for a specific system the form of the electronic potential has to be known and a technique to solve the equation has to be chosen.

An electron can be considered a point-like particle or be described by a probability distribution, depending on the purpose and the system under consideration. In any case the Pauli principle has to be taken into account. The principle states that fermions are indistinguishable objects which are described by antisymmetric wave functions. In other words, electrons with identical quantum numbers tend to spatially avoid each other.

The electronic Hamiltonian given by equation (2.4a) can be written as the sum of one-electron and two-electron terms.

$$\hat{H}_1^{\text{core}} = \hat{T}_e + \hat{V}_{eN} + \hat{V}_{NN} = \sum_i \hat{h}_i + \hat{V}_{NN} \quad , \text{ with } \hat{h}_i = -\frac{1}{2} \nabla_i^2 + \sum_n \frac{Z_n}{r_{in}} \quad (2.10)$$

$$\hat{H}_2 = \hat{V}_{ee} = \sum_{i>j} \frac{1}{r_{ij}} \quad (2.11)$$

These equations are written in atomic units, which are generally assumed, if not stated otherwise. Within the Hartree theory the Coulomb interaction between electrons is approximated by the total charge density. It has to be mentioned, that after calculating the total charge density, the density of electron i has to be subtracted when calculating the two-electron integrals for this electron. The electrons are not explicitly coupled and therefore the wave function can be written as a product of one-electron functions. Therefore,

the Hartree-Fock theory is an independent particle theory. These functions are generated by \hat{h}_i satisfying

$$\hat{h}_i\phi_j(x_i) = \varepsilon_j\phi_j(x_i). \quad (2.12)$$

The ϕ_j are one-electron spin orbital functions, but also orthogonal spatial orbital functions could be used. The issue of orbital functions in *ab-initio* calculations is covered in section 2.1.3, here generic definitions are used. Since the total wave function Ψ has to be antisymmetric for the exchange of electrons it can be written as a Slater determinant as proposed by Fock [3] and Slater [4]:

$$\Phi = \frac{1}{\sqrt{N!}} \begin{vmatrix} \phi_1(1) & \phi_2(1) & \cdots & \phi_N(1) \\ \phi_1(2) & \phi_2(2) & \cdots & \phi_N(2) \\ \vdots & \vdots & \ddots & \vdots \\ \phi_1(N) & \phi_2(N) & \cdots & \phi_N(N) \end{vmatrix} \quad (2.13)$$

The electronic energy is written as the solution of a matrix eigenvalue problem and the matrix elements are integrals. The usage of one-electron building blocks for the wave function and their orthogonality, does significantly simplify the evaluation of the Hamiltonian. The one-electron and two-electron integrals do not depend on the complete wave function, but just the terms which include these electrons. The one-electron integrals

$$\sum_i \langle \Phi | \hat{h}_i | \Phi \rangle = \sum_i \langle \phi_i | \hat{h}_i | \phi_i \rangle \quad (2.14)$$

are completely separable. In the case of two-electron integrals the $\frac{1}{r_{ij}}$ operator prevents total separation, so that two orbitals are coupled:

$$\langle \Phi | \hat{V}_{ee} | \Phi \rangle = \sum_{i>j} \langle \Phi | \frac{1}{r_{ij}} | \Phi \rangle \quad (2.15)$$

Taking a two-electron system as example, the anti-symmetrised two-electron integral can be written down easily.

$$\begin{aligned} & \langle \phi_1(1)\phi_2(2) | \frac{1}{r_{12}} | \phi_1(1)\phi_2(2) \rangle \\ &= \frac{1}{2} \int [\phi_1(1)\phi_2(2) - \phi_1(2)\phi_2(1)] \frac{1}{r_{12}} [\phi_1(1)\phi_2(2) - \phi_1(2)\phi_2(1)] d1d2 \\ &= \int \frac{1}{2} \phi_1(1)\phi_2(2) \frac{1}{r_{12}} \phi_1(1)\phi_2(2) d1d2 - \int \frac{1}{2} \phi_1(1)\phi_2(2) \frac{1}{r_{12}} \phi_1(2)\phi_2(1) d1d2 \\ & \quad - \int \frac{1}{2} \phi_1(2)\phi_2(1) \frac{1}{r_{12}} \phi_1(1)\phi_2(2) d1d2 + \int \frac{1}{2} \phi_1(2)\phi_2(1) \frac{1}{r_{12}} \phi_1(2)\phi_2(1) d1d2 \\ &= \frac{1}{2} [\langle 12|12 \rangle - \langle 12|21 \rangle - \langle 21|12 \rangle + \langle 21|21 \rangle] = \langle 12|12 \rangle - \langle 12|21 \rangle = \langle 12 || 12 \rangle \end{aligned} \quad (2.16)$$

In this notation $\langle 12|12\rangle$ is a short form of the two-electron integral including the r_{12}^{-1} operator and $\langle 12||12\rangle$ is a short form of the anti-symmetrised two-electron integral. The Hartree-Fock energy equation can now be written down as

$$E_{\text{HF}} = \langle \Phi | \hat{H}_e | \Phi \rangle = \langle \Phi | \hat{H}_1^{\text{core}} + \hat{H}_2 | \Phi \rangle = \sum_i \langle \phi_i | \hat{h}_i | \phi_i \rangle + \sum_{i>j} \langle ij | ij \rangle. \quad (2.17)$$

Up to now, the wave function was considered generic of form $\phi_i(x_j) = \phi_i(j)$, where x could represent spatial as well as spin functions. Now ϕ shall be defined as a product of the spatial function ψ times the spin function, which is denoted α for spin-up and β for spin down:

$$\phi_1(x) = \psi_1(r)\alpha \quad \text{and} \quad \phi_2(x) = \psi_1(r)\beta \quad (2.18)$$

This leads to the following two-electron state notation in one spatial orbital with opposite spins:

$$|\phi_1(1)\phi_2(2)\rangle = |\psi_1(r_1)\bar{\psi}_1(r_2)\rangle = |\psi_1\bar{\psi}_1\rangle \quad (2.19)$$

The integrals have to be determined for this basis, too. The one-electron integral does not change at all, because the spin function can be integrated easily giving factors of 1 for each integral. In the apparent basis each spatial orbital is doubled, as it can be occupied by spin-up and spin-down electrons. There are three distinguishable states: The orbital is doubly occupied (docc) by two electrons with opposite spin or the orbital is singly occupied (socc) with an α or β electron.

$$\begin{aligned} \sum_i \langle \Phi | \hat{h}_i | \Phi \rangle &= \langle \psi_1 | \hat{h}_1 | \psi_1 \rangle + \langle \bar{\psi}_1 | \hat{h}_1 | \bar{\psi}_1 \rangle + \langle \psi_2 | \hat{h}_2 | \psi_2 \rangle + \dots \\ &= (\psi_1 | \hat{h}_1 | \psi_1) + (\bar{\psi}_1 | \hat{h}_1 | \bar{\psi}_1) + (\psi_2 | \hat{h}_2 | \psi_2) + \dots \\ &= 2h_{11} + h_{22} + \dots \\ &= 2 \sum_i^{\text{docc}} h_{ii} + \sum_i^{\text{socc}} h_{ii} \end{aligned} \quad (2.20)$$

A new notation is introduced here: $\langle \bar{\psi}_1 | \hat{h}_1 | \bar{\psi}_1 \rangle = (\psi_1 | \hat{h}_1 | \psi_1)$. At the right-hand side the spin integration has been executed and only the spatial integration is left.

For the inspection of the two-electron integral again a two electron system is shown first with different spins but identical spatial orbits:

$$\langle \phi_1\phi_2 | \phi_1\phi_2 \rangle = \langle \psi_1\bar{\psi}_1 | \psi_1\bar{\psi}_1 \rangle = (\psi_1\psi_1 | \psi_1\psi_1) \quad (2.21)$$

$$\langle \phi_1\phi_2 | \phi_2\phi_1 \rangle = \langle \psi_1\bar{\psi}_1 | \bar{\psi}_1\psi_1 \rangle = 0 \quad (2.22)$$

The two-electron integral between identical states, also called two-electron expectation matrix (element), is reduced to the spatial integral immediately, because the spin integral is not perturbed by the spatial $\frac{1}{r_{12}}$ operator. In the case of opposite spin, the spin integral can not be separated. As in the integral two different states are "compared", the integral is now called two-electron transition matrix (element). In this case the integral has to be zero, as these spin states are orthogonal. Two-electron systems with parallel spin require different spatial orbitals.

$$\langle \Psi_1 \Psi_2 | \Psi_1 \Psi_2 \rangle = \langle 12 | 12 \rangle = \langle 12 | 12 \rangle - \langle 12 | 21 \rangle = (12 | 12) - (12 | 21) = J_{12} - K_{12} \quad (2.23)$$

The Coulomb integral J_{ij} accounts for the classically known Coulomb repulsion of electrons in orbitals i and j . The exchange integral K_{ij} , however, has no classical equivalent, nor even a true physical interpretation. The total Hartree-Fock energy equation in molecular orbitals can now be written as sums over N electron terms as

$$E_{HF} = \sum_i^{N_{elec}} h_i + \sum_{i,j}^{N_{elec}} (J_{ij} + K_{ij}) + V_{NN}. \quad (2.24)$$

The task is now to find a set of molecular orbitals with respect to which the energy is stationary, or better minimal, for variations of the orbitals. The variational theory delivers the corresponding tools. As the molecular orbitals must stay orthonormal, the Lagrangian takes the form

$$\mathcal{L} = E - \sum_{ij}^{N_{elec}} \lambda_{ij} (\langle \phi_i | \phi_j \rangle - \delta_{ij}). \quad (2.25)$$

The variational condition forces the variation of the Lagrangian to be zero. The variation is applied to the energy and the orbitals:

$$\delta \mathcal{L} = \delta E - \sum_{ij}^{N_{elec}} \lambda_{ij} (\langle \delta \phi_i | \phi_j \rangle - \langle \phi_i | \delta \phi_j \rangle) \quad (2.26)$$

The variation of the energy can be expressed in one-electron and two-electron terms

$$\delta E = \sum_i (\langle \delta \phi_i | \hat{h}_i | \phi_i \rangle + \langle \phi_i | \hat{h}_i | \delta \phi_i \rangle) + \sum_{ij} (\langle \delta \phi_i | \hat{J}_j - \hat{K}_j | \phi_i \rangle + \langle \phi_i | \hat{J}_j - \hat{K}_j | \delta \phi_i \rangle). \quad (2.27)$$

If one defines the Fock operator, an effective one-electron operator, as

$$\hat{F}_i = \hat{h}_i + \sum_j (\hat{J}_j - \hat{K}_j), \quad (2.28)$$

the variation of the energy can be written shortly as

$$\delta E = \sum_i (\langle \delta\phi_i | \hat{F}_i | \phi_i \rangle + \langle \phi_i | \hat{F}_i | \delta\phi_i \rangle). \quad (2.29)$$

Accordingly, the variation of the Lagrangian becomes

$$\begin{aligned} \delta\mathcal{L} &= \sum_i (\langle \delta\phi_i | \hat{F}_i | \phi_i \rangle + \langle \phi_i | \hat{F}_i | \delta\phi_i \rangle) - \sum_{ij}^{N_{elec}} \lambda_{ij} (\langle \delta\phi_i | \phi_j \rangle + \langle \phi_i | \delta\phi_j \rangle) \\ &= \sum_i \langle \delta\phi_i | \hat{F}_i | \phi_i \rangle - \sum_{ij}^{N_{elec}} \lambda_{ij} \langle \delta\phi_i | \phi_j \rangle + \sum_i \langle \delta\phi_i | \hat{F}_i | \phi_i \rangle^* - \sum_{ij}^{N_{elec}} \lambda_{ij} \langle \delta\phi_i | \phi_j \rangle^* = 0. \end{aligned} \quad (2.30)$$

As the variation of either $\langle \delta\phi |$ or its complex conjugate has to make the variation of the Lagrangian zero, either the first two terms must cancel, or the last two. If one subtracts the complex conjugates of the third and fourth term one gets

$$\sum_{ij} (\lambda_{ij} - \lambda_{ji}^*) \langle \delta\phi_i | \phi_j \rangle = 0. \quad (2.31)$$

This means that the Lagrange multipliers are part of a Hermitian matrix. The Hartree-Fock equations now take the form

$$\hat{F}_i \phi_i = \sum_j \lambda_{ij} \phi_j. \quad (2.32)$$

Physically this equation is sufficient. Yet, for the computation it is advantageous to introduce a unitary transformation of the molecular orbitals such that the λ_{ij} are diagonal. In this canonical orbitals, ϕ' , the Hartree-Fock equations take the form of pseudo-eigenvalues equations

$$\hat{F}_i \phi'_i = \varepsilon_i \phi'_i. \quad (2.33)$$

The final Hartree-Fock energy equation can be written as the sum of Fock effective one-electron energies and the two Coulomb interaction terms J and K :

$$E = \sum_i \varepsilon_i + \frac{1}{2} \sum_{ij} (J_{ij} - K_{ij}) + V_{NN}, \quad (2.34)$$

with

$$\varepsilon_i = h_i + \sum_j (J_{ij} - K_{ij}). \quad (2.35)$$

Unfortunately, the value of one Fock integral can only be obtained, if the values of all other Fock integrals are known. The solution for this is an iterative self-consistent field (SCF) approach, as illustrated in figure 2.1. Starting from an initial guess, usually the

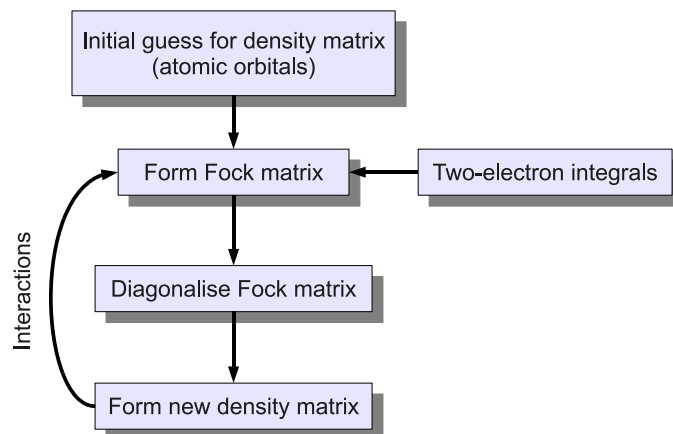


Figure 2.1: Illustration of the Self-consistent field (SCF) cycle.

atomic orbitals, the two-electron integrals are calculated and the Fock matrices are solved. The resulting molecular orbitals/electron densities are taken as input for the next iteration. Two-electron integrals and Fock matrices are evaluated in this cycle, until convergence is reached. This iterative procedure is usually converging fast to the correct Hartree-Fock energy. Nevertheless, convergence or convergence to a minimum are not guaranteed.

The molecular orbital functions are optimised during the SCF cycles, but their functional form was not discussed up to now. Usually these functions are expanded in a set of atomic orbitals, forming a linear combination of atomic orbitals (LCAO)

$$\phi_i = \sum_{\alpha}^{M_{basis}} C_{\alpha i} \chi_{\alpha}, \quad (2.36)$$

where M_{basis} is the number of atomic basis functions χ_{α} and $C_{\alpha i}$ are the coefficients of the expansion. The Fock equations in atomic orbitals is written

$$\hat{F}_i \sum_{\alpha}^{M_{basis}} C_{\alpha i} \chi_{\alpha} = \epsilon_i \sum_{\alpha}^{M_{basis}} C_{\alpha i} \chi_{\alpha}. \quad (2.37)$$

Multiplying left-hand-side with the basis functions and executing the integrals one ends with the Roothaan-Hall equations

$$\bar{F}\bar{C} = \bar{S}\bar{C}\bar{\epsilon}, \quad (2.38)$$

which are the Hartree-Fock equations in atomic orbitals. The orbital overlap matrix is defined as $S_{\alpha\beta} = \langle \chi_\alpha | \chi_\beta \rangle$ and the Fock matrix as

$$\begin{aligned} F_{\alpha\beta} &= \langle \chi_\alpha | \hat{F} | \chi_\beta \rangle = \langle \chi_\alpha | \hat{h} | \chi_\beta \rangle + \sum_j^{occ.MO} \langle \chi_\alpha | \hat{J}_j - \hat{K}_j | \chi_\beta \rangle \\ &= \langle \chi_\alpha | \hat{h} | \chi_\beta \rangle + \sum_{\gamma\delta}^{M_{basis}} D_{\gamma\delta} (\langle \chi_\alpha \chi_\gamma | \hat{g} | \chi_\beta \chi_\delta \rangle - \langle \chi_\alpha \chi_\gamma | \hat{g} | \chi_\delta \chi_\beta \rangle), \end{aligned} \quad (2.39)$$

with $g_{ij} = \frac{1}{|\vec{r}_i - \vec{r}_j|}$ and $D_{\gamma\delta} = \sum_j^{occ.MO} C_{\gamma j} C_{\delta j}$, where *occ.MO* are the occupied molecular orbitals. The energy equation in atomic orbitals, which can be realised in computer programs, is

$$E = \sum_{\alpha\beta}^{M_{basis}} D_{\alpha\beta} h_{\alpha\beta} + \frac{1}{2} \sum_{\alpha\beta\gamma\delta}^{M_{basis}} (D_{\alpha\beta} D_{\gamma\delta} - D_{\alpha\delta} D_{\gamma\beta} \langle \chi_\alpha \chi_\gamma | \vec{g} | \chi_\beta \chi_\delta \rangle) + V_{NN}. \quad (2.40)$$

2.1.3 Basis functions

One intrinsic approximation of all *ab initio* methods is the expansion of an unknown, like the molecular orbitals (MO), in basis functions. If the expansion was infinite, this is no approximation, but in reality only truncated expansions can be calculated. As described in the previous section, the MO orbitals are unknown functions, described in the n -dimensional space spanned by the basis functions. *Ab initio* methods usually scale at least with the fourth power of the number of basis functions. This strongly limits realistic sizes of basis sets. Therefore it is very important to choose functions which converge fast and are also easy to calculate. This is important as one- and two electron integrals are calculated using these functions, which can be very time consuming.

The optimal basis type depends on the problem at hand. For small molecular systems Gaussian type basis sets[5] are nowadays the standard general purpose basis sets. These bases can be written in polar coordinates

$$\chi_{\zeta,n,l,m}(r, \theta, \varphi) = N Y_{l,m}(\theta, \varphi) r^{2n-2-l} e^{-\zeta r^2} \quad (2.41)$$

or in Cartesian coordinates

$$\chi_{\zeta,l_x,l_y,l_z}(x, y, z) = N x^{l_x} y^{l_y} z^{l_z} e^{-\zeta r^2}. \quad (2.42)$$

The $Y_{l,m}$ are spherical harmonic functions, N is a normalisation constant. The parameter ζ is optimised in the basis sets to yield optimal results.

Basis sets are classified according to their size. The smallest possible basis set has one

function for each electron. For example, this would be one s orbital for hydrogen and two s and one p orbital for carbon. The next improvement is the doubling of all orbitals. Such a basis is called Double Zeta (DZ) type. Using more than doubling one obtains Triple Zeta (TZ), Quadruple Zeta (QZ), Quintuple Zeta (5Z) basis sets, and so on. The core electrons are relatively unimportant for the chemical behaviour. Therefore, valuable functions can be saved if these are not included into the doubling scheme. Such basis sets are called Valence X Zeta (VXZ, $X = D, T, \dots$). Another effect, which has to be taken into account is polarisation. The chemical bonding between two atoms changes the electron density distribution. Assuming that s electrons are responsible for a bonding, then these s orbitals can not describe the different electron densities along and perpendicular to the bond axis. This polarisation can be described by a p orbital. Further d orbitals describe the polarisation for p electrons and so forth.

A popular line of basis sets are the correlation consistent (polarised) basis sets (cc-pVxZ) by Dunning and co-workers[6, 7]. These sets are tailored such that the functions which add approximately the same amount of correlation energy are included in one step. Improvements to these bases can be done by adding either tight and/or diffuse functions. Tight functions have large exponents and help to take the core-core and core-valence correlations into account. These bases are abbreviated as cc-pCVXZ. Diffuse functions have a small exponent and are important for the description of loosely bound electrons or whenever tails of the wave functions are important. These bases are called augmented (aug-cc-pVXZ).

2.1.4 Post-Hartree-Fock methods

The Hartree-Fock (HF) self-consistent field method does not describe chemical bondings correctly, as described in section 2.1.2. A variety of treatments have been developed over the decades, which aim at the recovery of the correlation energy. The HF method determines the lowest energy one-determinant trial wave function. This section focuses on methods, which contain more than one determinant. The trial wave functions are then written as

$$\Psi = a_0\Phi_{HF} + \sum_{i=1} a_i\Phi_i. \quad (2.43)$$

The different post-HF methods are distinguished by how they derive the a_i . The three most common methods are Møller-Plesset (MP) perturbation theory, configuration interaction (CI) and coupled cluster (CC). The latter two methods are described in the following, as these are used in this work.

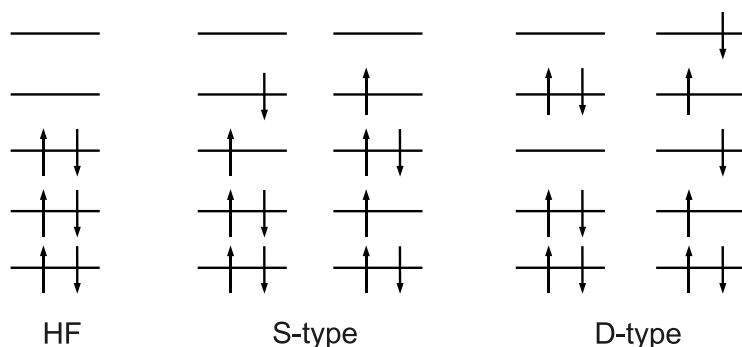


Figure 2.2: Excited Slater determinants obtained from a Hartree-Fock reference.

2.1.4.1 Excited Slater determinants

If the chosen basis set is not minimal, one can distinguish between occupied and unoccupied molecular orbitals (MO). Orbitals which are not occupied in Hartree-Fock are called virtual orbitals. The additional Slater determinants in equation (2.43) are obtained by replacing one or more occupied orbitals by virtual ones. Depending on the number of replaced MO the determined are referred to as Singles (S), Doubles (D), Triples (T) etc.

Figure 2.2 shows how these determinants are generated. On the left side there is spin free (singlet) Hartree-Fock reference occupation with three closed orbitals. A single excitation can come from any of the occupied orbitals in any virtual ones. The second S-type determinant is not spin free (triplet), as the excited orbital switched its spin. Double excitations can come from one or two orbitals, there are no restrictions if all types of excitations are allowed.

2.1.4.2 Configuration Interaction

The Configuration Interaction (CI) method is the oldest and one of the simplest approaches for post-HF calculations. The CI wave function is linearly expanded in the (excited) Slater determinants

$$\Psi_{CI} = a_0\Phi_{HF} + \sum_S a_S\Phi_S + \sum_D a_D\Phi_D + \sum_T a_T\Phi_T + \dots = \sum_{i=0} a_i\Phi_i. \quad (2.44)$$

These determinants are obtained from a previous HF run. The molecular orbitals (MO) are fixed and not further optimised. The CI energy can be obtained with variational approaches. Using Lagrange multipliers the problem can be written as

$$\mathcal{L} = \langle \Psi_{CI} | \hat{H} | \Psi_{CI} \rangle - \lambda (\langle \Psi_{CI} | \Psi_{CI} \rangle - 1). \quad (2.45)$$

If one inserts the definition of the CI wave function as expansion in Slater determinants, one gets an equation of the energy eigenvalues

$$\langle \Psi_{CI} | \hat{H} | \Psi_{CI} \rangle = \sum_{i=0} \sum_{j=0} a_i a_j \langle \Phi_i | \hat{H} | \Phi_j \rangle = \sum_{i=0} a_i^2 E_i + \sum_{i=0} \sum_{j \neq i} a_i a_j \langle \Phi_i | \hat{H} | \Phi_j \rangle \quad (2.46)$$

and an equation for the normalisation constraint

$$\langle \Psi_{CI} | \Psi_{CI} \rangle = \sum_{i=0} \sum_{j=0} a_i a_j \langle \Phi_i | \Phi_j \rangle = \sum_{i=0} a_i^2. \quad (2.47)$$

If the wave function is expanded, like in equation (2.46), the problem takes the form of matrix equations with $H_{ij} = \langle \Phi_i | \hat{H} | \Phi_j \rangle$. The diagonal elements can be calculated directly, as these are the eigenenergies of the Slater determinants. The variational approach is to restrict the derivative of the Lagrangian with respect to the a_i equal to zero:

$$\frac{\partial \mathcal{L}}{\partial a_i} = 2 \sum_j a_j H_{ij} - 2\lambda a_i = 0 \quad (2.48)$$

This can be further simplified to

$$a_i(E_i - \lambda) + \sum_{j \neq 0} a_j H_{ij} = 0 \quad (2.49)$$

for each a_i . The next step is to transform the equation into a form, where only one- and two-electron integrals are present, like in section 2.1.2.

A remark has to be given about the Slater determinants. The MO are spin-orbitals, that means that excited Slater determinants have a spin. There are α and β spin-MOs, depending on whether they have spin up or spin down. Not all excited Slater determinant fulfil the condition of being eigenfunction of \hat{S}^2 . To circumvent this, linear combinations of excited Slater determinants with the same spatial occupation, but opposite spin function are formed. These are called Configurational State Functions (CSF), as the spin is separated out.

Now, the procedure is similar to the Hartree-Fock case. All matrix elements between CSFs which differ by more than two MO are zero, as there are only one- and two-electron integrals and the functions are orthogonal. Also, matrix elements between the HF reference CSF and Singles CSFs are zero, due to Brillouin's theorem. There are ways to reduce the number of integrals further by symmetry and spin considerations.

The number of terms in the CI expansion in equation 2.44 is directly given by the size of the basis set. A Full CI, where the expansion is complete, can only be used for small molecules (meaning few electrons) and small basis sets. For real applications the expan-

sion must be truncated. This is usually done at the Doubles level (CISD), which scales with the number of basis functions like M_{basis}^6 . All truncated CIs lack two very important features: Size Consistency and Size Extensivity. Size consistent means that the summed energy of two or more compounds obtained from independent calculations is the same as the energy from one calculation in which all compounds are present, but they are separated. Far away in this context is a distance longer than the interaction distance, like $100a_0$. A simple example would be a D-type excitation in two H_2 molecules. These excitations can act on one molecule or on one orbital from each molecule, also for large distances. Multiplying the result for one H_2 by two, would generate results like CISDTQ for 2 H_2 . This example leads to the second short-coming, the lack of size extensivity. Truncated CI methods recover less and less correlation energy with increasing number of (interacting) electrons in the system.

2.1.4.3 Coupled Cluster theory

The Coupled Cluster (CC) theory[8, 9] is an alternative approach, which is always size consistent and size extensive. The idea is to include all corrections of a given type (like Doubles), up to an infinite order in perturbation theory. The Coupled Cluster theory has some similarities with CI, and Coupled Cluster and Full CI are equivalent in the limit of completeness. In CI the expansion of the wave function was directly written down, in Coupled Cluster one first defines an excitation operator

$$\hat{T} = \hat{T}_1 + \hat{T}_2 + \hat{T}_3 + \dots + \hat{T}_{N_{elec}} \quad (2.50)$$

as a sum of excitation operators \hat{T}_i . Each \hat{T}_i generates all i -times excited Slater determinants from the Hartree-Fock reference wave function. For Singles and Doubles these are

$$\hat{T}_1 \Phi_0 = \sum_i \sum_a^{occ\ vir} t_i^a \Phi_i^a \quad (2.51)$$

and

$$\hat{T}_2 \Phi_0 = \sum_{i < j} \sum_{a < b}^{occ\ vir} t_{ij}^{ab} \Phi_{ij}^{ab}. \quad (2.52)$$

Orbitals which are occupied in the reference functions are counted with i, j, \dots and the virtual ones with a, b, \dots . The expansion coefficients t are conventionally called amplitudes. With these operators the CI wave function (2.44) could be written as

$$\Psi_{CI} = (\hat{1} + \hat{T}) \Phi_0. \quad (2.53)$$

The CC wave functions are generated in a more sophisticated way:

$$\Psi_{CC} = e^{\hat{T}} \Phi_0 = \left(\hat{1} + \hat{T} + \frac{1}{2} \hat{T}^2 + \frac{1}{6} \hat{T}^3 + \dots \right) \Phi_0 \quad (2.54)$$

If one enters the expansion of the excitation operator in the expansion of the exponential, the terms are ordered according to their total excitation level:

$$e^{\hat{T}} = 1 + \hat{T}_1 + \left(\hat{T}_2 + \frac{1}{2} \hat{T}_1^2 \right) + \left(\hat{T}_3 + \hat{T}_2 \hat{T}_1 + \frac{1}{6} \hat{T}_1^3 \right) + \dots \quad (2.55)$$

Doubles can be connected, \hat{T}_2 , or disconnected, \hat{T}_1^2 . This corresponds to the simultaneous excitation of two interacting electrons and the excitation of two non-interacting electrons respectively. At all excitation levels also products of lower levels are included. This ensures the size consistency of the Coupled Cluster equations.

As the Schrödinger equation $\hat{H} e^{\hat{T}} \Phi_0 = E e^{\hat{T}} \Phi_0$ can not conveniently be solved by variational techniques, it is usually projected onto the reference wave function:

$$\langle \Phi_0 | \hat{H} e^{\hat{T}} | \Phi_0 \rangle = E_{CC} \langle \Phi_0 | e^{\hat{T}} \Phi_0 \rangle \quad (2.56)$$

The integral on the right-hand side is unity, as the wave functions are orthogonal. In this equation all but \hat{T}_1 and \hat{T}_2 vanish, as the Hamiltonian only contains one- and two-electron operators. After inserting the expansion of the excitation operator and some algebra one obtains an equation for the Coupled Cluster energy in terms of the Singles and Doubles amplitudes and two-electron integrals:

$$E_{CC} = E_0 + \sum_{i < j}^{occ} \sum_{a < b}^{vir} \left(t_{ij}^{ab} + t_i^a t_j^b - t_i^b t_j^a \right) \left(\langle \Phi_i \Phi_j | \Phi_a \Phi_b \rangle - \langle \Phi_i \Phi_j | \Phi_b \Phi_a \rangle \right) \quad (2.57)$$

Equations for the amplitudes can be formed by projecting the Schrödinger equation onto the spaces of the excited determinants:

$$\begin{aligned} \langle \Phi_m^e | e^{-\hat{T}} \hat{H} e^{\hat{T}} | \Phi_0 \rangle &= 0 \\ \langle \Phi_{mn}^{ef} | e^{-\hat{T}} \hat{H} e^{\hat{T}} | \Phi_0 \rangle &= 0 \\ &\vdots \end{aligned} \quad (2.58)$$

The explicit equations are lengthy and therefore not written down here.

Truncated CCs are generated by truncating the expansion of \hat{T} , while the expansion of the exponential is complete with the truncated \hat{T} . This causes higher excitations to occur in the expansion than indicated by the truncation level, because of the product/disconnected

excitations. CCSD scales with M_{basis}^6 , CCSDT with M_{basis}^8 . The latter one is usually not applicable. A broadly used variation is CCSD(T), where first a CCSD calculation is performed and the Triples contribution is obtained by perturbation theory. This level scales with M_{basis}^7 .

The Coupled Cluster theory is superior in accuracy compared with configuration interaction of the same level. There is, however, a crucial drawback. The standard CC methods are based on a single HF reference determinant. If the HF wave function is not a good approximation of the real wave function, the Coupled Cluster will lose its reliability similar to perturbation theory. As the Singles mimic an orbital relaxation, they can be used to measure the multi-reference character of the wave function. A popular method is the T_1 -diagnostic[10] for CCSD wave functions:

$$T_1 = \frac{1}{\sqrt{N_{elec}}} |\vec{t}_1|. \quad (2.59)$$

The norm of the Single amplitudes vector normalised by the square root of the number of the electrons is not a strict measure of the quality of CC. Experience shows, that CCSD(T) is expected to give results near the Full CI limit for $T_1 < 0.02$. If T_1 is larger, a multi-reference method should be used. Coupled Cluster is usually reliable around the equilibrium of the molecule, but it is going to fail if one approaches dissociation. Due to the way how the Coupled Cluster state is constructed, only the lowest eigenstate for each symmetry can be calculated. There are also multi-reference CC methods and methods which allow excited states, like equation-of-motion coupled cluster (EOM-CC), but these are limited, e.g. to singlet states, and not widely used.

2.1.4.4 Multi-reference techniques

As discussed, the Hartree-Fock wave function is not always a good trial wave function. This is the case in the (pre-)dissociation regions, where the actual electronic state is a mixture of the bound and dissociated molecule. Other examples are avoided crossing and other phenomena, where two electronic states have similar eigenvalues. Naturally, the Hartree-Fock wave function is not suited for excited electronic state calculations.

In order to overcome this problem, so-called multi-reference (MR) methods are used. The most common methods are based on CI theory, rather than coupled cluster. Although CC offers superior qualities, as discussed in 2.1.4.3, MR-CC methods are complicated to derive and to implement. Therefore, they are not widely used up to now and deliver only limited applicability.

Multi-Configuration Self Consistent Field. The simplest multi-reference method, is the Multi-Configuration Self-Consistent Field (MCSCF) method[11, 12]. It is, to some extent, a CI method, where also the molecular orbitals are optimised. Starting from Hartree-Fock orbitals, the orbitals are optimised self-consistently in CI calculations. This is a very time-consuming procedure if all electrons and orbitals are included. It is much more efficient to invest into expanding a standard CI to higher excitations. Therefore, MCSCF is usually only used for qualitative calculations, with restricted sets of excitations. The most common approach is to divide the molecular basis in active and inactive orbitals. Inactive orbitals are either fully occupied or empty. Active orbitals are allowed to have any occupation number (0,1,2). This Complete Active Space Self-Consistent Field (CASSCF) method is further classified by the number of electrons n which are distributed into m active orbitals, [n,m]-CASSCF. This method is valuable for physical studies of the electron density, orbital occupations etc. It also offers analytical solutions for diabatic couplings and spin-orbit couplings, which are not available in CI or CC implementations. The MCSCF method has a major disadvantage. As it is based on an SCF optimisation, there is no guaranty of convergence to a minimum, or to the correct minimum. The Hartree-Fock methods has the same limitations, but advanced methods were developed, that help the convergence for one Slater determinant. For MCSCF convergence problems are more common.

Multi-Reference Configuration Interaction. The Multi-Reference Configuration Interaction (MRCI) is the most advanced commonly used multi-reference method[13, 14]. The standard CI uses a wave function generated by excitations from a reference Hartree-Fock wave function. MRCI uses all the Configuration State Functions (CSF) from a MCSCF calculation. MRCI is therefore able to calculate energies for the whole configuration space and many excited states[15]. As the number of CSFs can easily reach millions or hundreds of millions, truncation methods are used. These remove CSFs internally, which are not important, according to some criteria. Still, the computational costs of a MR-CISD calculation are much larger than for a single reference CCSD(T) calculation.

2.2 Potential energy surface

Within the limits of the Born-Oppenheimer approximation (see 2.1.1), the motion of the nuclei in a molecular complex is taking place in an effective electronic potential. This potential is the solution of the electronic Schrödinger equation including nuclei-nuclei and electron-nuclei interaction with the coordinates of the nuclei as parameters. These potentials are $(3N - 6)$ -dimensional, where N is the number of nuclei in the molecular complex. In the case of linear configurations the number of degrees of freedom is $3N - 5$.

The numerical determination/exploration and representation of high dimensional potential energy surfaces (PES) is a challenging task and subject of ongoing research.

This work uses an approach developed by B.J. Braams[16, 17]. It aims at a general description of the potential, valid for many different molecules but still taking advantage of inherent molecular symmetry properties.

2.2.1 Internuclear distance coordinates

For the description of potential energy surfaces the choice of coordinates is very crucial. The set of coordinates should adapt the symmetry and/or geometry of the system surveyed to reduce dimensionality. For the PES we do not have to choose coordinates, where the Hamiltonian is represented efficiently, but only the potential itself, suggesting some kind of affine/relative coordinates. The coordinate system should be a good choice for all the configuration space under consideration and usually a minimal set of coordinates is preferable.

For potentials used for spectroscopy, often called force fields in this context, symmetry adapted internal coordinates are a common choice. They present the most natural choice of a minimal set of coordinates accounting for the symmetry of the molecule as well as for the symmetry of the fundamental molecular motions, namely the normal mode vectors. While this is sufficient for most spectroscopic cases, these coordinates become inappropriate for large amplitude motions and reactive behaviours, since every molecule has a different set of symmetry-adapted internal coordinates.

Internuclear distances coordinates present a far more general and flexible alternative. A molecular system of N atoms has $\frac{(N-1)N}{2}$ unique internuclear distances $d(i, j) = d(j, i) = \|\vec{r}_i - \vec{r}_j\|$, where i and j are different atoms and \vec{r} are their coordinates in a Cartesian coordinate system. Only $3N - 6$ of these coordinates are independent, because the representation is invariant to translation or rotation of the molecule. The quadratic increase of coordinates restricts the application to small- and medium-sized systems. Nevertheless, it is a favourable choice, where it is computationally treatable, because it allows the potential to be formulated invariant against exchange of like nuclei. In addition the coordinate system is identical for any configuration of the N atom system, especially the fragment (meaning reactant and product) and complex region for a reactive system.

2.2.2 Potential representation

The invariant theory offers the generators for non-orthogonal polynomials for N -atom systems. While it is possible to use these polynomials directly, further optimizations can

be done.

For potentials used only for spectroscopic purposes it is sufficient to stay with one polynomial expansion. In the case of reactive surfaces a many-body expansion, also called cluster expansion, is beneficial. For a system consisting of m atoms of type X and n atoms of species Y the expansion has the form

$$V = V_X + V_Y + V_{X_2} + V_{Y_2} + V_{XY} + \dots + V_{X_m Y_n}. \quad (2.60)$$

This form allows a better description of the local potential of the fragments and dissociation energies. Also, it reduces the calculation time for the PES when only fragment data is asked for. Which terms of the expansion are included is user-defined. When a many-body expansion is used, each function is meant to govern certain regions in the configuration space. The smooth switching between the potential terms is guaranteed by a damping function t_0 . First, an average internuclear distance is defined as

$$d = \sqrt{\frac{1}{(N-1)N} \sum_{j=2}^N \sum_{i=1}^{j-1} (r^2(i,j) + r^2(j,i))} = \sqrt{\frac{2}{(N-1)N} \sum_{j=2}^N \sum_{i=1}^{j-1} r^2(i,j)}. \quad (2.61)$$

The damping function is defined as

$$t_0 = \max\left(0, \frac{(1-d/a)^k}{d^l}\right), \quad (2.62)$$

where k and l are integer parameters, usually taken as 3 or 5 and 0 or 1, respectively. If d is larger than the cut-off length a , which is usually chosen as $a = 8a_0$, the corresponding term will not contribute to the total potential. Figure 2.3 shows the behaviour of the damping function for typical combinations of parameters. While the choice of k only slightly influences the slope, the functions with $l = 1$ decrease much stronger and therefore effectively remove the corresponding term much earlier from the complete potential.

The general form of the potential contributions is

$$V_{X_m Y_n} = \sum_{i_1 < \dots < i_m \in X'} \sum_{j_1 < \dots < j_n \in Y'} f_{X_m Y_n}(r_{i_1 i_2}, \dots, r_{i_{m-1} i_m}, r_{i_1 j_1}, \dots, r_{i_m j_n}, r_{j_1 j_2}, \dots, r_{j_{n-1} j_n}), \quad (2.63)$$

where

$$f = p(y) \cdot t_0, \text{ with } y = e^{-r/\lambda}. \quad (2.64)$$

The polynomial p is now expressed in terms of Morse-like variables. If there is more than one possibility to produce a certain fragment from the complete molecular system, functions f from all these permutations have to be included, as indicated by (2.63). For

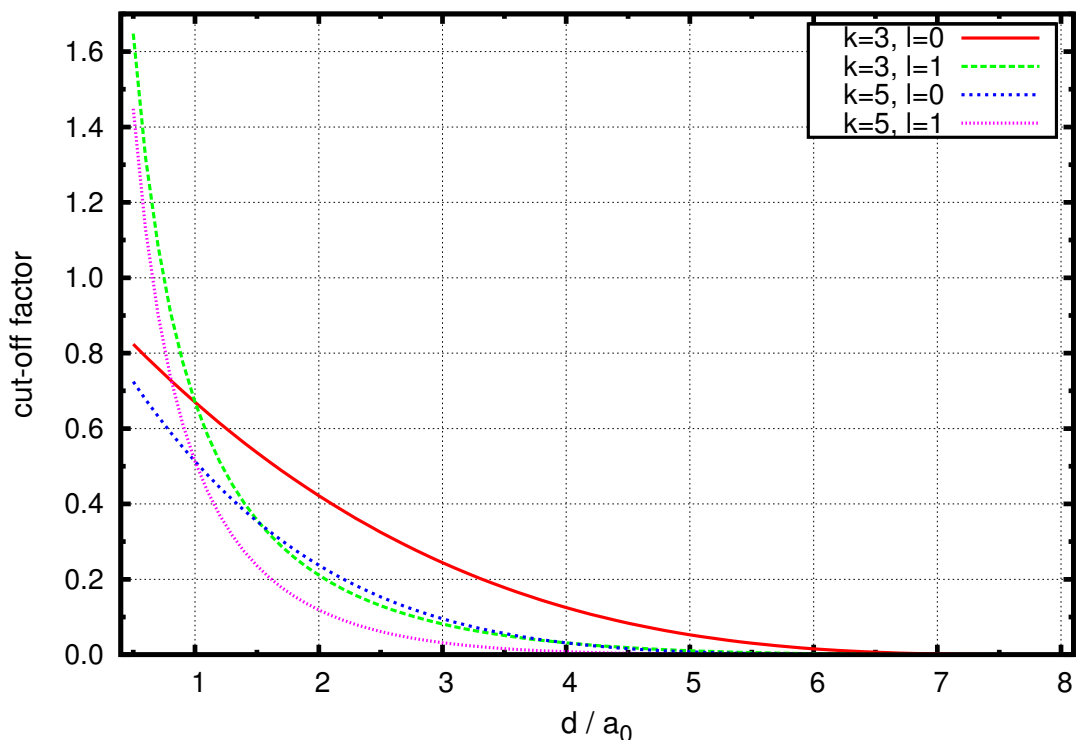


Figure 2.3: Damping function according to (2.62) with $a = 8a_0$ with distances in atomic units.

example, having a CH_2 molecule, there are two combinations to form a CH fragment. The one-body terms are simply the product of the atomic energy times the number of atoms of this species in the system: $V_X = E_X \cdot n_X$.

2.2.3 Fitting

The potential is fitted by computing the minimum-norm solution to a real linear least-squares problem using the Lapack DGELSX¹ routine. It minimizes $\|A * X - B\|$, where A is a $n_b \times n$ matrix with n_b being the number of unknowns and n the number of configurations used for the least-squares system. B is the vector containing the n calculated potential values and X is the solution vector containing the n_b coefficients of the polynomial.

In the fitting process itself all regions are equally weighted, but in some applications not always all regions of the configuration space are equally important. For example, wave functions usually show higher sensitivity to low energy regions of the potential. In strictly bounded cases their expectation value should be zero for higher energy regions. Therefore, a weighting according to the energy of a configuration is justified. The weighting

¹See <http://www.netlib.org/lapack/double/dgelsx.f>

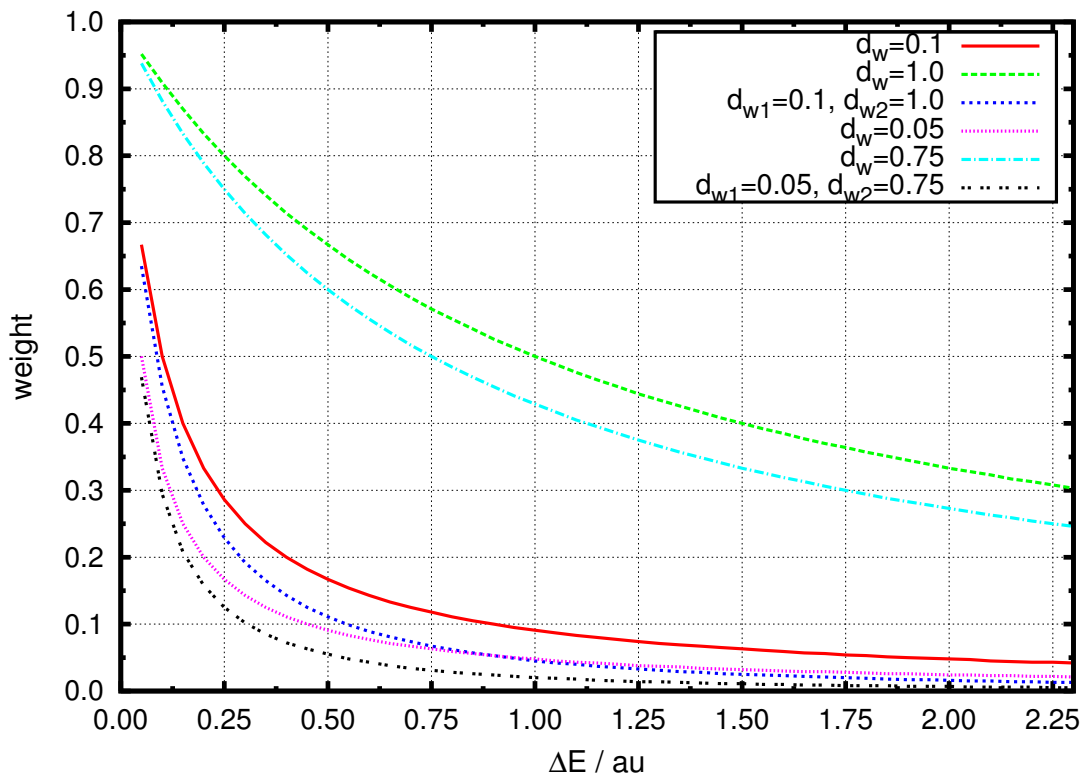


Figure 2.4: Weight according to (2.65) for different weight parameters as a function of relative energy above the global minimum. The energy is given in atomic units.

function $w(i)$ of the i -th's configuration is defined as

$$w(i) = \frac{d_{w1}}{d_{w1} + E_i - E_{min}} \cdot \frac{d_{w2}}{d_{w2} + E_i - E_{min}}, \quad (2.65)$$

where d_{w1} and d_{w2} are the weighting parameters and E_{min} is the lowest energy of the set. Finding appropriate parameters is entirely empirical. The standard choice is $d_{w1} = 0.1$ hartree and $d_{w2} = 1.0$ hartree. As shown in figure 2.4 among other choices, this combination gives strong weight for the low energy region only, but contains reasonable weight for configurations up to ≈ 0.5 hartree. Such a compromise gives rise to sufficient accuracy around the global minimum, but includes also the energy scales typical for reaction paths and other minima. In the case of high energy reaction paths this choice has to be adjusted. A test with the alternative set $d_{w1} = 0.05$ hartree and $d_{w2} = 0.75$ hartree showed no significant improvement for the spectroscopic properties of the methane PES.

The matrix A is filled as $A'(i, j) = w(i) \cdot f(i, j)$ and B is written as $B(i) = w(i) \cdot (E_i - E_{min})$. The entries in A' can differ by many orders of magnitude, causing an ill conditioning of the numerical problem. The matrix is normalized row-wise $A(*, j) = A'(*, j)/s(j)$ with $s(j) = \sqrt{\frac{1}{n} \sum_i A'(i, j)^2}$ to circumvent this problem. The coefficient vector is normalized in the same manner after applying the DGELSX routine: $X'(j) = X(j)/s(j)$. It appears that

despite the measures taken, an ill-conditioning of the system can be found when going to higher order polynomials, like 9'th order in the case of methane.

2.2.4 Dipole moment surface

The presented routines are adjusted for the construction of dipole moment surfaces (DMS) as well. The dipole moment is a vector property and may not directly be expressed in terms of polynomials over internuclear distance coordinates. Therefore, the dipole moment is internally defined as the product of the Cartesian coordinates and the effective atomic charge of the system. With this the same set of invariants as for the PES can be used for the DMS. In the case of the PES for each configuration one vector with length n_b is used to fill the coefficient matrix A . In the case of the DMS a matrix M with dimensions $N \times n_b$ contains the polynomials. The coefficient matrix is filled with a $4 \times n_b$ matrix for each configuration. Three rows contain the product of the Cartesian coordinates with M having the dipole moment components as right-hand side. The fourth row contains the sum over all nuclei of each term of the polynomials having the right-hand side set to zero. This ensures neutrality of the system. This DMS of a certain degree includes significant more coefficients than a PES. Fortunately, dipole moment surfaces are less complex and can be handled with polynomials of lower order.

2.3 Lagrange-Mesh Method

The analytical solution of the one-dimensional Schrödinger equation is a computationally difficult task. Therefore, methods for approximate solutions have been developed for many decades. Many of them use mesh methods to replace the analytical integral by numerical quadrature. The following introduction is based on an article of Baye[18], which gives a good introduction to this topic.

Harris *et al.*[19] first introduced a simple approximate way to calculate potential matrix elements by using values of the potential at discrete values of the coordinate, which was later linked with the Gauss quadrature by Dickinson and Certain[20]. Lill *et al.*[21] and Light *et al.*[22] simplified this idea into a method known as the discrete-variable representation (DVR). In this approach one works directly with representations for which the approximate potential matrix is diagonal. The non-diagonal kinetic-energy matrix is calculated by transformations from another representation. Both representations are related by a Gauss quadrature formula. This method was developed further over the years and was also expanded to multi-dimensional systems. Another path was followed by Schwartz[23], who constructed global interpolation functions which vanish at all but one

mesh point. He showed that such functions naturally lead to mesh equations when a Gauss quadrature is employed. The concept of a Lagrangian basis, which is used in this work, was introduced by Baye and Heenen[24] in 1986. The indefinitely differentiable basis functions are very similar to Schwartz's interpolation functions but, in addition, the basis is required to be orthogonal. This requirement introduces strict conditions on possible meshes. It allows us to interpret the mesh equations as an approximate variational calculation involving a basis of square-integrable functions. The Lagrange-mesh method became applicable to realistic problems after Vincke *et al.*[25] proposed the idea of regularisation in order to eliminate singularities which are not compatible with the conditions of accuracy of the Gauss approximation.

As mentioned before the Lagrange-mesh method has strict conditions for basis functions. For the introduction of this method one starts with a set of N indefinitely differentiable basis functions $\phi_k(x)$ which satisfy the orthonormality conditions

$$\langle \phi_k | \phi_l \rangle = \int_a^b \phi_k^*(x) \phi_l(x) dx = \delta_{kl} \quad (2.66)$$

over a given interval $[a,b]$ of x values. The square root of the normalisation factors are included in the definition of the $\phi_k(x)$. For this basis N mesh points x_i are selected in the interval. Each mesh point is given a weight

$$\lambda_i = \left[\sum_{k=1}^N |\phi_k(x_i)|^2 \right]^{-1}. \quad (2.67)$$

These mesh points and corresponding weights define an approximate Gauss type quadrature rule

$$\int_a^b g(x) dx \approx \sum_{i=1}^N \lambda_i g(x_i). \quad (2.68)$$

The quality of this approximate quadrature rule depends on the choice of the mesh points x_i . If chosen properly, as will be shown, the quadrature can be made exact for any $g(x) = \phi_k^*(x) \phi_l(x)$. It is then expected to be a good approximate quadrature rule for all indefinitely differentiable functions $g(x)$.

Baye defined another set of N basis functions $f_i(x)$, which are build from the former:

$$f_i(x) = \lambda_i^{1/2} \sum_{k=1}^N \phi_k^*(x_i) \phi_k(x). \quad (2.69)$$

These functions satisfy the orthogonality relations

$$\langle f_i | f_j \rangle = \lambda_j^{1/2} f_i^*(x_j) = \lambda_i^{1/2} f_j^*(x_i). \quad (2.70)$$

This equation relates the scalar product of f , a global property defined over the whole interval, to the value of f at mesh points, which are a local property of the basis functions. The functions $f_i(x)$, as defined in equation (2.69), are called Lagrange functions if they satisfy the Lagrange conditions

$$f_i(x_j) = \lambda_i^{-1/2} \delta_{ij}. \quad (2.71)$$

If inserted into equation (2.70) this directly provides the orthonormality relation

$$\langle f_i | f_j \rangle = \delta_{ij} \quad (2.72)$$

for these basis functions. This is the condition, that the approximate Gauss quadrature rule (2.68) is exact for any product $f_i(x)f_j(x)$ or $\varphi_k(x)\varphi_l(x)$.

If one applies the Lagrange and orthonormality conditions to the definition of the basis functions f_i in equation (2.69) this yields $N(N-1)/2$ conditions for the N mesh points x_i . For $N \geq 4$ the number of conditions is larger than N . For all real applications N is larger than four. Therefore, no Lagrange meshes need to exist for any set of indefinitely differentiable basis functions. If one combines equations (2.67) and (2.69) under the conditions above, one finds

$$\sum_{k=1}^N \varphi_k^*(x_i) \varphi_k(x_j) = \lambda_i^{-1} \delta_{ij}. \quad (2.73)$$

This equation is automatically satisfied, if the Gauss quadrature rule (2.68) is exact for $\langle \varphi_k | \varphi_l \rangle$. If these conditions are true one has

$$\sum_{i=1}^N \lambda_i \varphi_k^*(x_i) \varphi_l(x_i) = \delta_{kl}. \quad (2.74)$$

This implies the matrix with elements $\lambda_i^{1/2} \varphi_k(x_i)$ is unitary and that equation (2.73) is satisfied [20, 22]. Lagrange functions always exist when some Gauss-like approximation is exact for $\langle \varphi_k | \varphi_l \rangle$.

The Lagrange functions provide a variational basis for the study of Hamiltonians of the form

$$H = -\frac{d^2}{dx^2} + V(x) \quad (2.75)$$

for some given boundary conditions. The wave function is expanded as

$$\Psi(x) = \sum_{i=1}^N \lambda_i^{1/2} \Psi(x_i) f_i(x). \quad (2.76)$$

If the variational basis is large enough, the variational coefficients $\Psi(x_i)$ are accurate approximate values of the wave function at the mesh points.

The matrix elements of the kinetic energy operator $T = -d^2/dx^2$ are written as

$$T_{ij} = \langle f_i | T | f_j \rangle, \quad (2.77)$$

while those of the potential $V(x)$ are approximated as

$$V_{ij} = \langle f_i | V | f_j \rangle \approx V(x_i) \delta_{ij}. \quad (2.78)$$

With this, the variational system for the Schrödinger equation is

$$\sum_{j=1}^N \{ T_{ij} + V(x_i) \delta_{ij} - E \delta_{ij} \} \lambda_j^{1/2} \Psi(x_j) = 0. \quad (2.79)$$

This equation has the usual form of mesh equations, as obtained, for example, in a finite difference method. However, these equations are obtained from a variational approach and are expected to be much more accurate for a given number of points. They provide not only energies and values of the wave function at mesh points, but also values of the approximate wave function over the whole interval, if desired. These equations are very simple to generate as they do not require any analytical integration.

2.4 Recap

In this chapter the basic methods used in this work were introduced. In the following these methods are applied to applications of increasing complexity. Different *ab initio* methods are major tools used in the following. The polynomial fit ansatz for the potential energy surfaces will be used for spectroscopic and reactive studies of hydrocarbons. As a next step multiple electronic states for MgH are calculated using the Lagrange-mesh method to obtain energies and transition moments. With them line lists and photodissociation cross sections will be calculated for MgH. In the last chapter, extensive reactive studies will be presented based on a global *ab initio* potential energy surface of CH_2^+ .

3 Potential energy surfaces for small hydrocarbons

Hydrocarbons are among the most common molecules in the universe. Hydrogen, as the most common element in the universe, can be found practically everywhere since the beginning of time. Carbon is generated by fusion in stars. It is spread by novae and can be found in stars, interstellar dust, comets, planets etc. Both elements are very reactive and tend to form a large variety of molecules. This makes them interesting candidates for the computational chemical physics. Small hydrocarbons have the advantage, that high level methods can be applied, which are too costly for larger molecules. In order to survey spectroscopic and reactive behaviours, reliable potential energy surfaces are needed.

In this chapter potential energy surfaces (PES) for small hydrocarbons of the type CH_x , with $x = 1, 2, 3, 4$, are presented. The potentials are based on the internuclear distances fit approach of B.J. Braams (see 2.2). The surfaces are primarily designed for spectroscopic purposes, but reactant data were included where possible. This offers limited access to reaction dynamics. The emphasis of this chapter is on the capabilities and bottlenecks of *ab initio* methods and potential fits. It delivers a classification of the fundamental methods used throughout the thesis. This corresponds to the first two steps of the multi-step work flow, as presented in figure 1.1.

The CH_x potential energy surfaces are designed to have a similar accuracy, which implies the usage of the same *ab initio* methods for all levels. The best results can be obtained with Coupled Cluster methods (see 2.1.4.3), as their implementations recover most correlation energy of all methods. In contrast to Configuration Interaction methods, they are size consistent and extensive. If the surfaces shall be used for reaction dynamics, they should include fragment data for the reactants. This also means, that the cluster expansion (or many body expansion) should be used (see section 2.2). As Coupled Cluster methods do not converge, or converge to wrong results, for the dissociation regions, they are rarely used for reaction dynamics potentials. On the other hand, they have to be used for the cluster expansion, as configuration interaction is not size consistent and size extensive.

As the focus is on spectroscopic applicability and high quality, a Coupled Cluster method

was chosen for this work. As a consequence not all reaction channels could be included for some molecules, as will be shown. For some of the potentials test calculations for rovibrational energies were performed.

3.1 Choice of *ab initio* method

The best Coupled Cluster methods which can be applied to all molecules in this chapter, are the explicit correlated methods. The quality of *ab initio* calculations depends very much on the basis set. Unfortunately, the convergence to the basis set limit is very slow for increasing basis size. It is approximated to converge with the maximal angular momentum l_{max} in the basis function as l_{max}^{-3} . The reason lies in the short-range interaction of two electrons. If two electrons approach each other the potential diverges with one over their distance. In order to keep the results finite, the kinetic energy must cancel the infinite potential at the pole. This causes the wave function to have a discontinuous derivative at this point, and a linear behaviour at near distances. These are poorly represented by the expansion of the wave function in terms of Slater determinants with Gaussian type basis sets. Explicit correlated wave functions are wave functions which depend explicitly on the distance between two electrons. The exact implementation involves three- and four-electron integrals, which are computationally much too expensive. The many-electron integrals are approximately expressed in terms of sums of products of simpler two-electron integrals. The current state-of-art approximation, the F12 method[26, 27], uses the exponential expression $F_{12} = e^{-\beta r_{12}}$ for the explicit correlation. The geminal coefficient β , must be given as input parameter. In Coupled Cluster theory the wave function is generated by excitations from a Hartree-Fock wave function. In the case of the CCSD level, the excitation operator is restricted to $e^{\hat{T}_1 + \hat{T}_2}$. The one-electron excitation operator is not changed in the F12 theory, as it aims at two-electron correlation effects. The two-electron operator in standard Coupled Cluster theory was defined in equation (2.52) as

$$\hat{T}_2\Phi_0 = \sum_{i < j}^{occ} \sum_{a < b}^{vir} t_{ij}^{ab} \Phi_{ij}^{ab}, \quad (3.1)$$

where i, j are occupied orbitals and a, b virtual orbitals. In the F12 theory the Coupled Cluster wave function gets its explicit correlation terms by additional excitation operators from a standard Hartree-Fock reference wave function:

$$\hat{T}_2\Phi_0 = \sum_{i < j}^{occ} \sum_{a < b}^{vir} t_{ij}^{ab} \Phi_{ij}^{ab} + \sum_{i < j}^{occ} \sum_{\alpha < \beta}^{complete} \mathcal{T}_{ij}^{\alpha\beta} \Phi_{ij}^{\alpha\beta}. \quad (3.2)$$

α and β refer to a complete basis set. As there is no complete basis set in an *ab initio* calculation, the additional amplitudes $\mathcal{T}_{ij}^{\alpha\beta}$ are approximated by

$$\mathcal{T}_{ij}^{\alpha\beta} = \langle \alpha\beta | \hat{Q}_{12} \hat{F}_{12} | kl \rangle t_{ij}^{kl}. \quad (3.3)$$

The operator \hat{Q} is designed to ensure orthogonality of the additional Slater determinants to the reference wave function and the standard Doubles. There are different implementations of the CC-F12 method, each with different additional assumptions and approximations, which shall not be discussed here. For convenience and reproducibility the standard implementation of the MOLPRO2010 *ab initio* program package was used[28], called by the "RCCSD(T)-F12a" directive with enabled Triples correction (scale_trip=1). Furthermore, the innermost *s*-shell electrons of carbon were included in the optimisation. Only results with a T_1 diagnostic of less than 0.025 were included for the potential fitting.

In conjunction to the CC-F12 method, a specialised basis set was chosen. The cc-pVXZ-F12 basis sets[29, 30] correspond to the standard aug-cc-pVXZ basis sets of Dunning and co-workers, but the exponents are tuned for the usage with F12 methods. Normal basis sets have to account for the missing explicit short-range two-electron correlation in the wave function expansions, which is no longer needed, if F12 methods are used. Therefore, these new basis sets improve the quality for CC-F12 calculations even further, without the addition of basis functions. In this work triple- ζ basis sets were used, cc-pCVTZ-F12 for carbon and cc-pVTZ-F12 for hydrogen. The results have the quality of at least CCSD(T)/aug-cc-pCV5Z level.

Table 3.1: Fit parameters and root-mean-square (rms) error estimates. The damping parameter a and the coordinate transformation parameter λ are used according to equations (2.62) and (2.64). The errors estimates are given for the intervals [0,0.1), [0.1,0.2) and [0.2,0.5) atomic units above the global minimum. Weighted errors are given according to weighting function (2.65).

	coeff.	degr.	a / a_0	λ / a_0	rms / 10^{-4} au	fragments
H ₂	10	9	8	1.8	0.012 / 0.020 / 0.135 / w: 0.013	H
CH	10	9	9	2.0	0.099 / 0.287 / 0.196 / w: 0.066	H, C
CH ₂	308	13	10	2.5	2.43 / 8.53 / 3.72 / w: 2.16	H, C, H ₂ , CH
CH ₃	960	9	10	2.8	2.04 / 6.55 / 7.73 / w: 1.76	H, C, H ₂ , CH
CH ₄	4685	9	1e36	2.3	2.94 / 11.0 / 21.9 / w: 3.28	-

3.2 Potential energy surfaces

In the standard application of the Braams potential surface all coefficients are calculated simultaneously during the least-squares fit, also if the cluster expansion is used. This has two disadvantages which can have impact on the quality. In the Braams polynomial potential representation each polynomial has five input parameters. The three most important ones are the order/degree of the polynomial, the damping length a from equation (2.62) and the coordinate transformation parameter λ from equation (2.64). In the standard procedure, all fragments with the same number of atoms are fitted using the same parameters. This limits the number of parameters, which has to be determined by trial-and-error. On the other hand, each molecule has a specific combination of optimal parameters, which are influenced by the equilibrium distances and the internuclear separation needed to reach the asymptotic dissociation energy. Second, the weight given to a configuration depends on its energy relative to the global minimum. Fragment data with relative large energies might not be represented properly due to that. In this work, the fitting scheme was changed to allow a successive fitting of the fragments. Optimal fits for the fragments are taken as given for a certain molecule, so that only one term of the cluster expansion has to be calculated at once. A side remark should be given to the fitting for molecules with different dissociation channels. In theory each channel has different optimal fit parameters, yet this can not be realised with this kind of invariant polynomial fits. Compromises for the parameters have to be used. Experience suggests increased root-mean-square errors by factors 2 to 3 due to this. The fit parameters as well as the root-mean-square (rms) error estimates for the fits can be found in table 3.1.

The build up of potential energy surfaces of hydrocarbons start with the asymptotic atomic energies of hydrogen (2S) and carbon (3P). For the chosen method these are -0.499946 au and -39.844523 au, respectively. The hydrogen potential is near the analytic limit of -0.5 au. The aug-cc-pVTZ basis set for comparison, gives a value of

Table 3.2: Equilibrium distances, angles and dissociation energies, compared with experimental results.

	r_e / a_0	α_e	D_e / eV	r_e^{exp} / a_0	α_e^{exp}	D_e^{exp} / eV
H ₂	1.402	—	4.759	1.401	—	???
CH	2.113	—	3.653	2.116	—	???
CH ₂	2.032	133.87°	3.511 ^b / 4.615 [†]	2.050	135.5°	4.301 [†]
CH ₃	2.034	120.00°	4.947 [‡] / 5.091 [#]	2.039	120.0°	4.871 [#]
CH ₄	2.052	109.47	n.a.	2.054	109.47	4.363 [‡]

^b C + H₂; [†] H + CH; [‡] CH + H₂; [#] H + CH₂; [‡] H + CH₄

-0.499821 au, which is one order less converged. The aug-cc-pVTZ is an often used standard basis set and was also used by me for a previous version of a methane potential.

H₂, CH. The H₂ potential was built from 649 *ab initio* points in the interval between $0.48a_0$ and $3.445a_0$. As one can see in figure 3.1 the *ab initio* data covers most of the potential well, but the Coupled Cluster fails near the dissociation limit. Fortunately, the asymptotic potential value is known, so that a fair representation of that region could be found. Typical weighted errors and errors in the first interval between zero and 0.1 au above the global minimum are typically in the order of few 10^{-4} au for Braams polynomial potential energy surfaces. For H₂ values of $1.28 \cdot 10^{-6}$ au and $1.16 \cdot 10^{-6}$ au are significantly better. If there is no *ab initio* data for a larger piece of the configuration space, the fit is free to take any form, which allows better fitting of the neighbored parts of the configuration space. Yet, within this region the fit tends to take non-physical form. In that sense, the fit with the lowest possible rms errors is not necessarily the best one.

The second two-body potential is the CH potential energy curve. It was built from 500 *ab initio* points in the interval from $0.5675a_0$ to $4.29a_0$. The Hartree-Fock part of the *ab initio* calculations is failing in the dissociation up to almost $10a_0$. Afterwards the calculations converge, but to the singlet state of carbon. Therefore, these data had to be

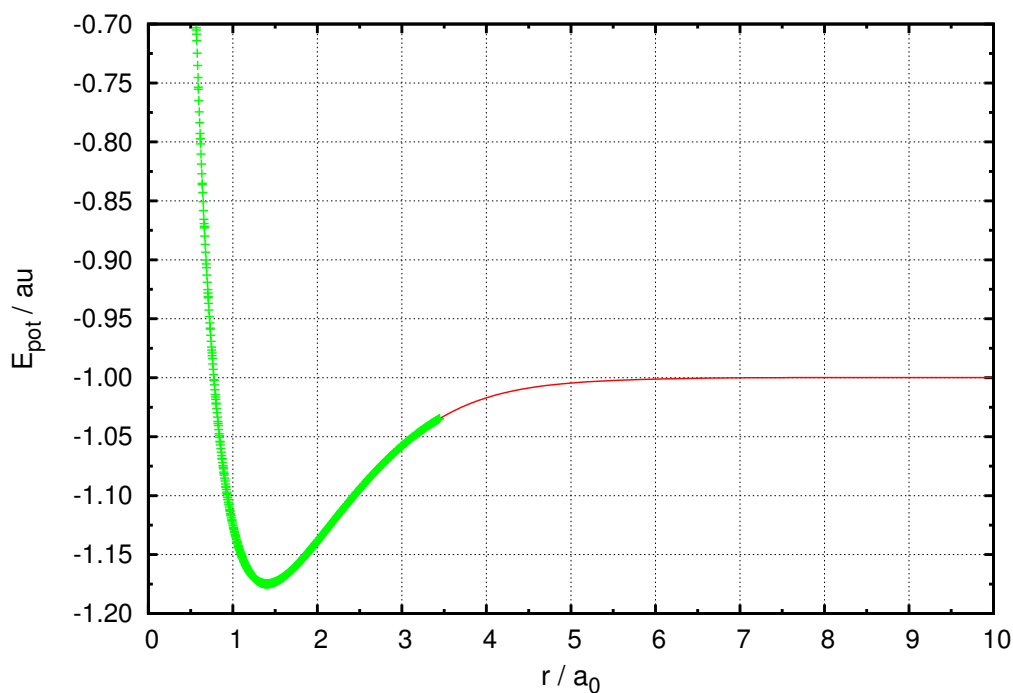


Figure 3.1: Potential energy curve for H₂. *Ab initio* data is drawn with green crosses.

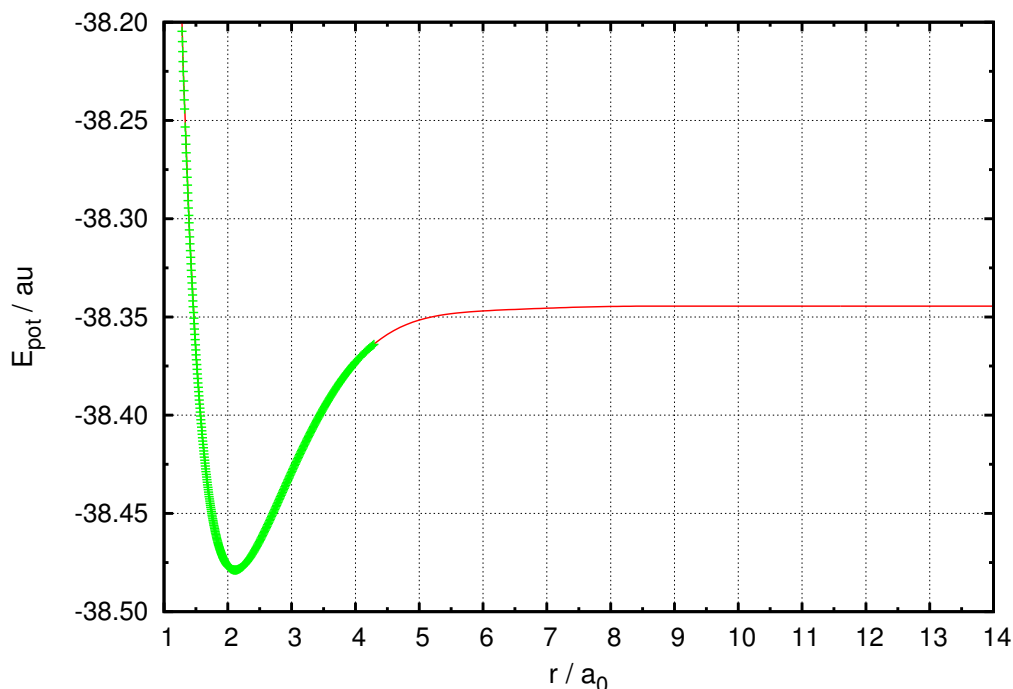


Figure 3.2: Potential energy curve for CH. *Ab initio* data is drawn with green crosses.

removed from the data set. Accordingly, the fit was forced smoothly to the atomic energies, as for hydrogen. The fit errors are in the order of 10^{-5} au. The manual adjustment of the potential in the dissociation regions can not replace proper *ab initio* data. In these cases the consequences reduce to slightly changed energies highly rovibrationally excited levels, which are rarely important. MRCI methods would converge in these areas of the configuration space, where CC did not. But MRCI has a significantly reduced accuracy. An alternative would be to fill only those parts of the configuration space with MRCI energies, where CC results are not available. While this idea is appealing, practical implementations suffer from the risk of side effects. The MRCI results must be somehow scaled and shifted to fit the CC data. In general, it is difficult to find such regions and properly adjust the data for high-dimensional molecules.

CH₂. The first three-body term in the cluster expansion is H₃. As H₃ is not a stable molecule this term is omitted. The other three-body term is CH₂. This molecule has a triplet ground state, X^3B_1 , and an excited state, \tilde{a}^1A_1 , which is only 0.396 eV = 3191 cm⁻¹ higher in the present calculations. Both states have been subject to previous numerical studies, e.g. Alexander *et al.* [31], Bunker *et al.* [32], Neugebauer and Häfelfinger [33], Dawes *et al.* [34]. For the ground state 9896 *ab initio* points were calcu-

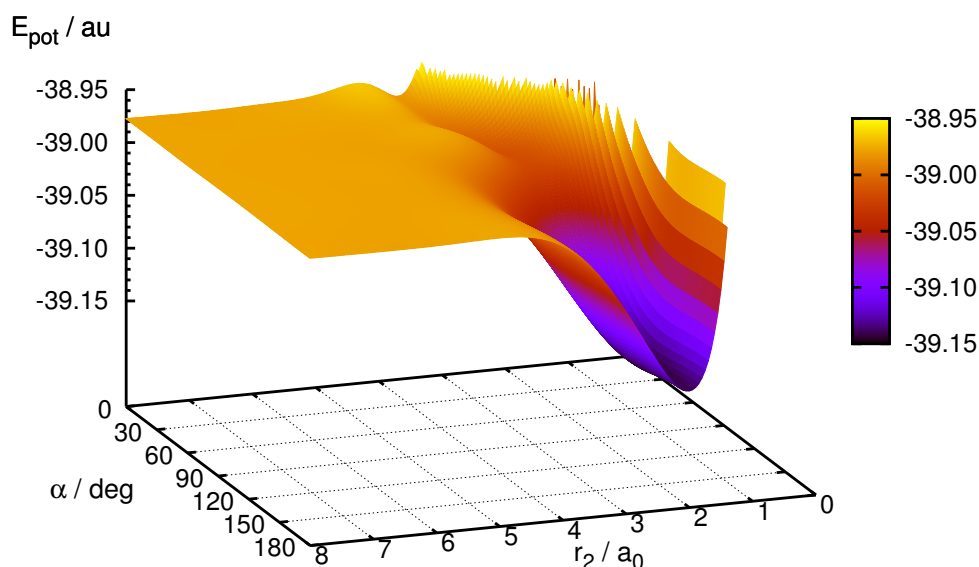


Figure 3.3: Two-dimensional cut through the potential energy surface of CH_2 . The distance $r(\text{C-H}^{(1)}) = 2.03 a_0$ is fixed. $r_2 = r(\text{C-H}^{(2)})$ and $\alpha = \angle\text{H-C-H}$

lated. The fragments for the cluster expansion are $\text{H} + \text{CH}$ and $\text{C} + \text{H}_2$, which results in 11046 *ab initio* points for the fit. The weighted fit error of $2.16 \cdot 10^{-4}$ au is typical for the size of the molecule and the degree of the polynomial. As both fragment channels could be included in the fit of CH_2 , this specific surface is suited for spectroscopic calculations as well as reaction dynamics. This is of course under the condition, that the accuracy of the fit is sufficient for the specific application. Figure 3.3 shows a two-dimensional cut through the potential surface. The distance between carbon and one hydrogen atom was held fixed at $2.03 a_0$. This is approximately the equilibrium distance for CH and CH_2 . The other C-H distance and the angle H-C-H were varied. Accordingly, the figure shows an overview over the potential well as well as the $\text{H} + \text{CH}$ reaction channel. The potential shows a smooth transition from the fragment to the complex region, as intended.

CH_3 . The only four-atom compound in this work is the methyl radical CH_3 . For this planar molecule 8168 *ab initio* points were used. The $\text{CH} + \text{H}_2$ fragment data was included, while the $\text{H}^+ \text{CH}_2$ fragment was not. The reason for this is an incompatibility between the data sets. The asymptotic minimum of the $\text{H}^+ + \text{CH}_2$ fragment is -39.648278 au. As one can see in figure 3.4, the CH_3 data have a local maximum above -39.60 au, which makes the data incompatible. As the bond dissociation energy of 5.09 eV is not far from the

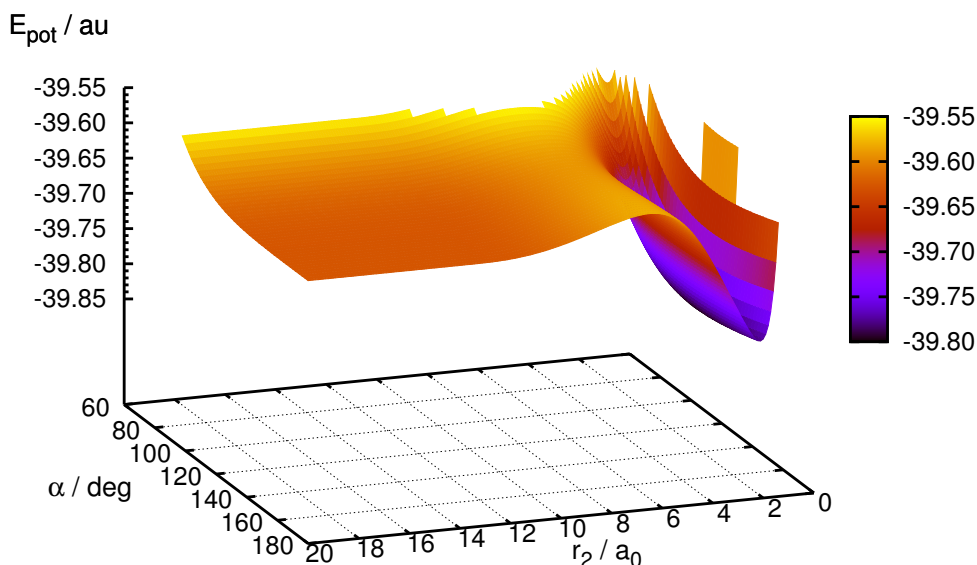


Figure 3.4: Two-dimensional cut through the potential energy surface of CH_3 showing the $\text{H} + \text{CH}_2$ channel. One C-H distance was varied with r_2 . The other two C-H distances are fixed at $2.03 a_0$. α is the angle between the latter H atoms.

experimental value of 4.87 eV, the fragment data can be considered correct. It is possible, that Coupled Cluster results were included, which show a too strong multi-reference character. For the H-abstraction potential, the Hartree-Fock energy does not converge to an asymptotic energy, but it is increasing further. At a certain point the SCF algorithm might also fail to converge. As the Coupled Cluster results strongly depend on the quality of the reference Hartree-Fock, artificial potential walls can appear in the dissociation region. This can be prevented by restricting the T_1 -diagnostic threshold for "good" Coupled Cluster results. On the other hand this might produce holes in the fitting procedure, if the space without any *ab initio* data gets too large. The $\text{CH} + \text{H}_2$ channel is represented correctly with the included fragment data. Figure 3.5 shows a two-dimensional potential energy surface cut for this channel. The area of the complex well is on the left side around $r_2 = 2$ to $3 a_0$. Due to the choice of coordinates the dissociation channel is shown as a small stripe on the lower end of the figure.

CH₄. The largest molecule considered in this work is methane. The potential for this molecule is ten dimensional in internuclear distance coordinates and was built from 60004 *ab initio* points including also fragment configuration spaces. These *ab initio* energies

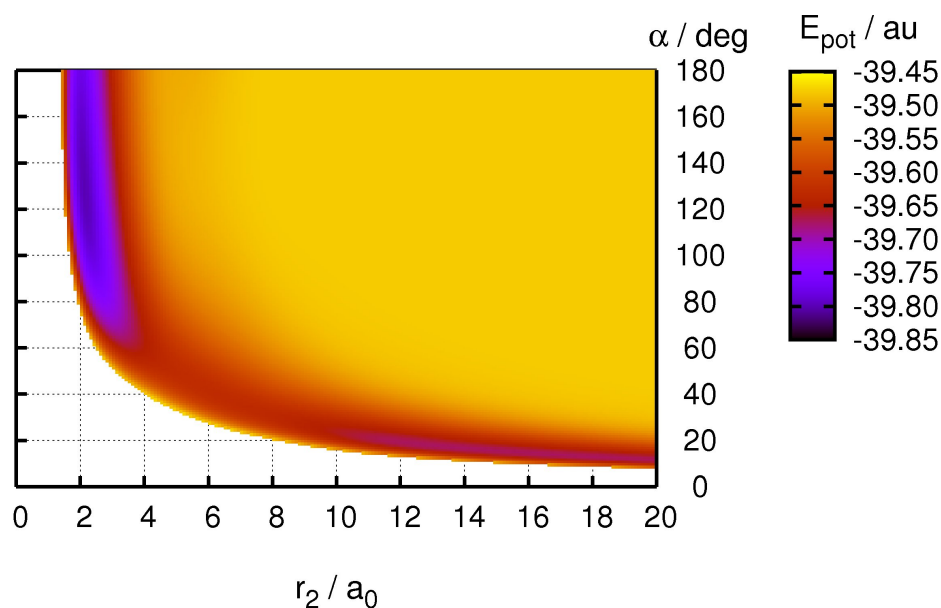


Figure 3.5: Two-dimensional cut through the potential energy surface of CH_3 showing the $\text{H}_2 + \text{CH}$ channel. One C-H distance was fixed at $2.11 a_0$. The other two C-H distances are identically changed as r_2 . α is the angle between the latter H atoms.

were calculated using MOLPRO2009[35] with the cc-pVTZ-F12 basis set. Although fragment *ab initio* points are included, the high dimensionality makes it difficult to guarantee smooth transitions from the complex to the fragment regions of the configuration space. Therefore, the fit presented in this work is classified as purely spectroscopic. The rms fit error for the first 0.1 au above the global minimum is $2.94 \cdot 10^{-4}$ au small, which is similar to the errors of the smaller molecules, but it increases relatively fast for higher energies. Diagnostics of potential energy surfaces of high dimensionality are difficult. The rms errors used in this work diagnose how well the fit represents the *ab initio* data for a certain energy interval. But this does not tell anything about the total quality compared to the "real" values. Also this does not allow a more specific analysis for the configuration space, to find out, where larger deviations occur. The common one- or two-dimensional cuts through the surface are of limited use for a ten-dimensional surface. Usually these are done for the normal mode displacement motions for spectroscopic potentials and along the lowest energy reaction path for reactive potentials. One-dimensional potential cuts along the normal mode displacement vectors are shown in figure 3.6. As this figure explicitly shows the potential for the vibrational eigenmodes of methane, the energy is given in reciprocal centimetres (offset = 40.512066 au; $1 \text{ au} = 27.2107 \text{ eV} = 219474.6 \text{ cm}^{-1}$). Details of the vibrational modes are discussed in 3.3.2. Here, it is only important that

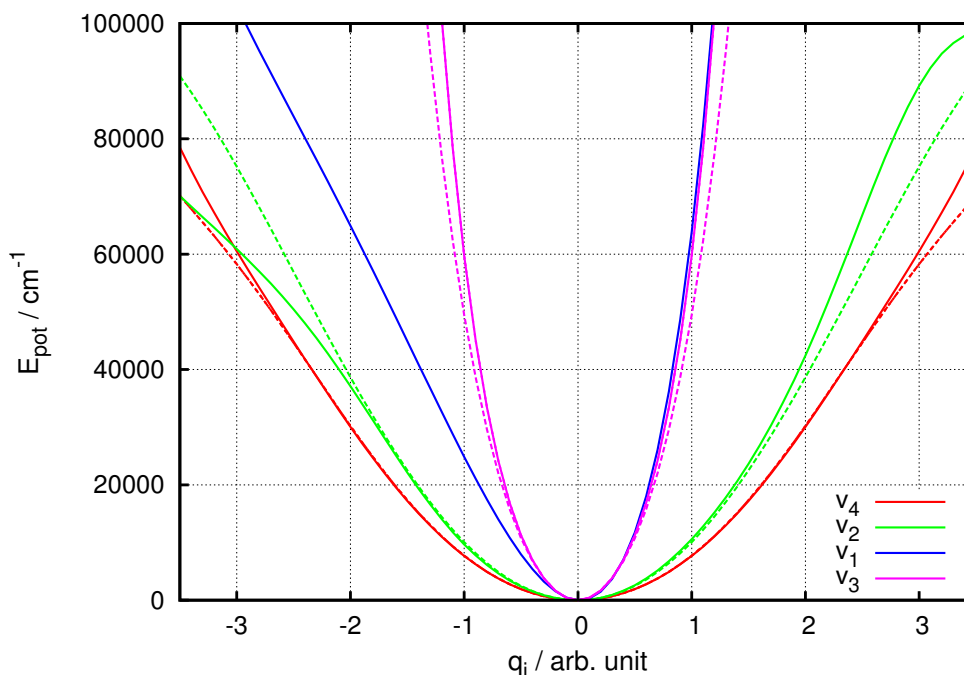


Figure 3.6: One-dimensional cuts through the potential energy surface of CH_4 along the normal mode displacement vectors. Displacements q_i in arbitrary units.

the potential cuts are unsuspecting in the energy range up to 20000cm^{-1} or 50000cm^{-1} , which is important for spectroscopy. One of the v_2 displacements, the straight line, shows atypical changes in the slope above 50000cm^{-1} for negative displacements and above 80000cm^{-1} for positive displacements. These can be artefacts of the fit or a result of a changing characteristic of the molecular configuration. If nuclei come near each other, or a dissociation-like configuration is reached the potential form varies from the normal asymmetric or symmetric curves like the ones shown in figure 3.6. Further diagnostics have to be performed, if these energy ranges are of interest or the vibrational energies do not show the expected quality.

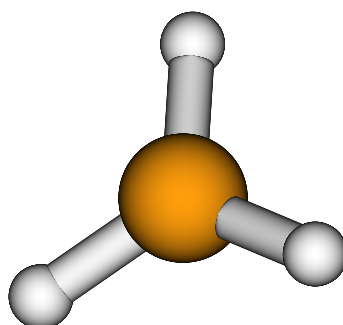
3.3 Application

The CH_x potential energy surfaces presented are suited for the usage in rovibrational spectroscopy. In addition the CH_2 potential can be used for reaction dynamics. The quality of the potentials can not only be described by the fitting errors. More important is the quality of the vibrational energy levels compared to experiments.

In this work the MULTIMODE[36–39] code was used to calculate vibrational and rotational energy levels of polyatomic molecules. MULTIMODE uses a method called Varia-

tional Configuration interaction (VCI) to obtain vibrational energies. In this method the wave functions are expanded in the normal mode vibrations and their overtones. The excitation level is user-defined and has to be adjusted until the expansion is converged. For vibrational energies up to six different normal modes can be combined at once. This is called mode coupling. The quantum number of the eigenvalues is given by the largest coefficient in the expansion. While this expansion allows to calculate accurate energies also for higher excitation levels, the quantum number assignment is not necessarily unique. For dipole transition moments only a coupling of four modes is implemented. The Hamiltonian used by MULTIMODE has a pole, when a non-linear molecule is bent to linearity. The ground state of CH_2 has a barrier to linearity of only 1935 cm^{-1} . Therefore, MULTIMODE can only be used to calculate energies for CH_3 and CH_4 .

3.3.1 CH_3



The methyl radical CH_3 is an intermediate product in hydrocarbon chemical networks, like the ones in the interstellar medium. It has also been detected in the atmospheres of Saturn and Neptune. CH_3 recombines very fast with other chemical compounds in gas phase. Therefore, it is very difficult to obtain accurate data from laboratory experiments. This makes this molecules an interesting candidate for spectroscopic and reactive computations. In this work, the potential energy surface CH_3 is primarily suited for spectroscopy.

CH_3 has six vibrational degrees of freedom of which four are doubly degenerate. This leaves four distinctive vibrational modes. The lowest energy motion, ν_2 , is an out-of-plane bending mode, also called umbrella motion. It is infrared active, because the out-of-plane bending produces a large dipole moment. The second mode in energy, ν_4 , is a doubly degenerate in-plane bending mode, which should be weakly infrared active. The symmetric stretch mode ν_1 is infrared inactive, as a symmetric motion does not induce dipole moments. The asymmetric stretch ν_3 is doubly degenerate and weakly infrared active.

A list of the lowest lying vibrational levels is given in table 3.3. Experimental vibrational energy levels are only available for the fundamental vibrational levels, besides ν_4 , and the $\nu_2 = 2,3$ overtones. There are a limited number of vibrational levels available from

Table 3.3: Selected vibrational energies of CH₃. Calculations from Medvedev *et al.* [40], Schwenke [41] and experiments[42–45] are compared. All energies in cm⁻¹.

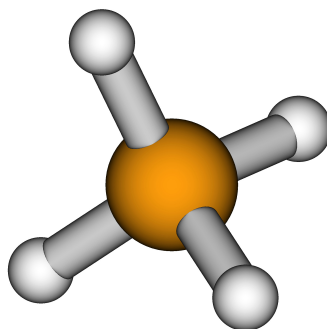
$\nu_1\nu_2\nu_3\nu_4$	new	Med.	Schw.	Exp.
zpe	6512.0	6445.9	6449.2	???
0100	612.5	591.7	596.3	606.5
0200	1298.4	1266.2	1278.9	1288.1
0001	1396.5	1388.4		
0101	2017.7	1991.8	1997.0	
0300	2032.9	1994.2	2025.6	2019.2
0201	2711.5	2674.0	2690.6	
0002	2765.4	2750.7	2748.2	
0002	2784.3	2767.8	2766.1	
0400	2804.6	2763.2	2829.0	
1000	3015.2	2988.5	2991.5	3004.4
0010	3171.2	3142.8	3144.4	3160.8
0102	3399.9	3367.1	3371.1	
0102	3414.7	3383.0	3388.5	
0301	3455.3	3407.5	3447.8	
0500	3605.2	3557.7	3686.0	
1100	3614.8	3572.8	3575.5	
0110	3760.8	3710.0	3716.0	
0202	4104.2	4057.5		
0202	4116.8	4073.1		
0003	4127.5	4107.8		
0003	4163.0	4138.0		
0401	4243.3	4179.7		
1200	4286.7	4234.3		

numerical studies of Schwenke [41] and Medvedev *et al.* [40]. All these data are included in table 3.3. The vibrational energies are 6 – 14 cm⁻¹ larger than the experimental values. The deviation is relatively constant over the energy. This is positive, as it implies, that the potential has a constant quality over the energy. More important, the transition energies are differences of energy levels. If their errors are similar, the line positions are more accurate than the energies. The other numerical studies tend to underestimate the vibrational energies by a larger amount than the overestimation in this work. The work of Schwenke seems to switch from an underestimation to an overestimation for higher excited states. This produces increased errors in the line positions. The deviations between the data of Schwenke and Medvedev *et al.* are strongly varying from a few cm⁻¹ to over 100 cm⁻¹ for $\nu_2 = 5$. The energies from this work are consistently larger compared to the results of Medvedev *et al.*. The good agreement with the few experimental data and the rather constant deviation from Medvedev *et al.* suggest a superior quality of the new data

obtained in this work.

All rovibrational states up to 7000cm^{-1} over the zero point energy (zpe) have been calculated for rotational levels up to $J = 5$. Transitions between these states were calculated, which has been used to obtain Einstein coefficients of spontaneous emission. These coefficients measure the transition probability for one molecule per second. This information can be used as input for radiation models. The line list is not complete and is mainly intended as an estimate of the line strengths of the different vibrational states. Figure 3.7 shows the Einstein coefficients A_{ji} over the emission energy. While there are transitions over the whole energy range, most of them are small. There are two major emission bands. The lower one ranges from 3000 to 3300cm^{-1} . These are mainly transitions where ν_3 is reduced by one, although the ν_3 mode is considered to be only weakly infrared active. The interesting point is, that the initial and final states for these transitions are excited in the strong infrared active ν_2 mode, which has a transition energy around 600cm^{-1} . It appears, that the combination of ν_2 with another mode, produces stronger transitions, than for this mode alone. This hypothesis is strengthened by the transitions of the second strong emission band between 4350 and 4700cm^{-1} . There, the ν_3 and ν_4 modes are simultaneously decreased by one quantum number each. Again, the final and initial states are excited in ν_2 . For the moment there are no line lists available for this molecule. Therefore, the potential energy surface provided by this work should be used to create one.

3.3.2 CH₄



Methane is a very common hydrocarbon and is found in most environments, where hydrocarbons are around. It is chemically very stable, with the exception of substitution reactions with halogens. Besides the typical astrophysical environments, which were already mentioned, it is often used in experimental plasma physics. In the last years it also became famous as an important greenhouse gas, which is mainly produced by cattle.

Methane has nine vibrational eigenmodes of which all but one show degeneracies, leaving four distinctive modes. The non-degenerate ν_1 mode is a symmetric stretch and therefore infrared inactive. The ν_2 mode is two-fold degenerate and represents a torsional bend.

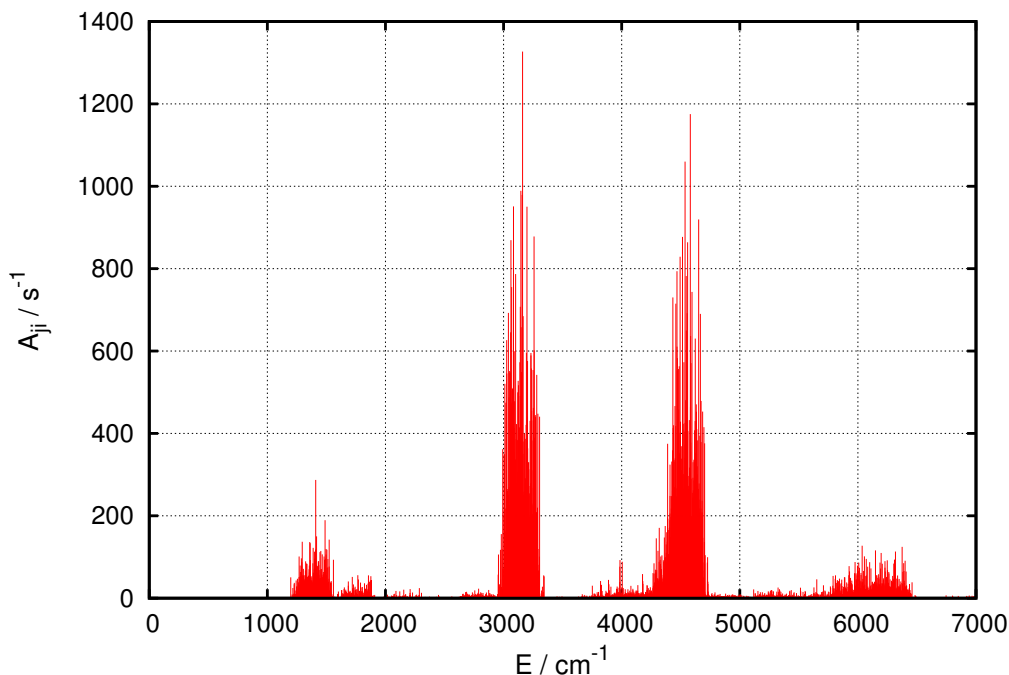


Figure 3.7: Einstein coefficients for spontaneous emission of CH_3 up to $J = 5$. The maximal rovibrational energy is limited to 7000cm^{-1} .

As two normal mode vectors belong to this mode, two curves are drawn for this mode in figure 3.6. The asymmetric stretch mode ν_3 and the umbrella bend mode ν_4 are both threefold degenerate. Only these two ones are infrared active.

In this work two generations of methane potentials were used. The original one has been used to calculate all rovibrational eigenvalues up to 6200cm^{-1} . From these a line list has been generated[47], which was tested in atmospheric modelling of Brown dwarfs by Hauschildt *et al.* [51]. This potential surface was based on RCCSD(T)/aug-cc-pVTZ *ab initio* data. The current potential, as presented in section 3.2, used a better *ab initio* method, a better basis set, more *ab initio* points and a higher order polynomial. Selected vibrational energies of these potentials are shown in table 3.4 together with energies from other works and experiments. The new potential shows significantly improved vibrational energies compared with the original fit. Deviations from experiments could be reduced from $20 - 30\text{cm}^{-1}$ for the worst cases to about $10 - 15\text{cm}^{-1}$. The new fit is of similar quality like the octic force field T8 from Schwenke and Partridge [52], which was used by Wang and Carrington [46]. The octic force field uses an expansion in symmetry-adapted internal coordinates. These coordinates are optimal coordinates for near equilibrium configurations. In addition the lower coefficients of the potential have direct physical meaning like harmonic frequencies, which can be adjusted to experimental results. For large amplitude motions these coordinates become more and more inappropriate, because they

Table 3.4: Vibrational energies of CH₄ below 5000cm⁻¹. Comparison with calculations from Wang and Carrington [46], Warmbier *et al.* [47] and experiments[48–50]. All energies are in cm⁻¹.

$\nu_1\nu_2\nu_3\nu_4$	irrep.	Exp.	new	War.	Wang
0000	A1		9708.55	9662.18	9691.53
0001	F2	1310.76	1310.61	1308.63	1311.74
0100	E	1533.33	1532.66	1521.44	1533.25
0002	A1	2587.04	2587.68	2583.67	2589.77
0002	F2	2614.26	2614.44	2610.56	2616.24
0002	E	2624.62	2624.96	2621.25	2627.30
0101	F2	2830.32	2830.76	2818.54	2831.53
0101	F1	2846.08	2845.42	2834.37	2846.91
1000	A1	2916.48	2918.13	2901.46	2913.71
0010	F2	3019.49	3019.73	3003.65	3013.6
0200	A1	3063.65	3056.45	3044.13	3063.49
0200	E	3065.14	3062.19	3045.86	3065.01
0003	F2	3870.49	3871.58	3866.82	3874.75
0003	A1	3909.19	3909.69	3905.11	3912.27
0003	F1	3920.52	3920.86	3915.88	3924.09
0003	F2	3930.92	3931.67	3925.96	3935.34
0102	E	4104.62	4103.11	4090.89	4104.48
0102	F1	4128.73	4131.62	4120.57	4131.31
0102	A1	4133.02	4134.65	4130.62	4135.80
0102	F2	4142.86	4143.68	4146.67	4144.88
0102	E	4151.00	4151.88	4161.90	4153.76
0102	A2	4161.91	4161.95	4172.96	4164.36
1001	F2	4223.46	4224.24	4207.74	4221.85
0011	F2	4319.21	4319.69	4303.07	4314.23
0011	E	4322.20	4322.22	4306.00	4317.59
0011	F1	4322.58	4323.02	4307.34	4317.83
0011	A1	4322.69	4323.15	4309.46	4318.42
0201	F2	4348.71	4344.87	4335.11	4350.10
0201	F1	4363.59	4362.25	4349.12	4364.74
0201	F2	4378.98	4374.51	4378.77	4379.77
1100	E	4435.12	4436.54	4413.18	4432.22
0110	F1	4537.55	4538.36	4512.45	4531.37
0110	F2	4543.76	4543.32	4519.6	4537.82
0300	E	4592.01	4580.43	4568.28	4591.94
0300	A2	4595.28	4585.46	4570.30	4595.17
0300	A1	4595.46	4591.84	4571.07	4595.44
⋮	⋮	⋮	⋮	⋮	⋮

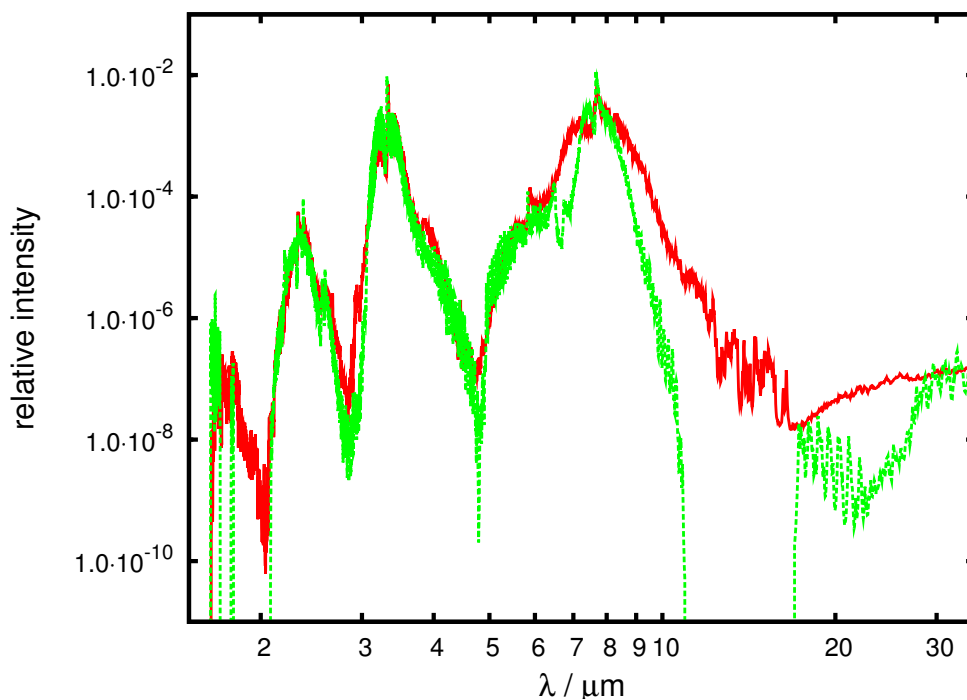


Figure 3.8: Relative intensities of methane at 1000 K[47]. Comparison between intensities obtained from this work (red) and HITRAN2004[53].

are coupled to the symmetry properties of the molecule. Deviations in the order of few reciprocal centimetres from experiment can originate from the potential as well as from the solver for the rovibrational eigenvalues. Both potentials, or solvers, have problems with overtones of the ν_4 state. The new potential mainly shows larger deviations for the E modes, which points at problems with the MULTIMODE code, which is used to obtain rovibrational eigenvalues.

The MULTIMODE code is used in this work for all polyatomic eigenvalue problems. As described above, it can accurately solve the eigenvalue problems even for higher excited states. As it is a general code using a normal mode expansion, not all problems can be solved with the same accuracy. States which are poorly represented by the normal modes, internal rotations and degenerated modes are problematic. The version 4.9.1 of MULTIMODE was used to generate a complete-as-possible line list of methane. For this, approximations to the dipole matrix elements and the line positions had to be done. MULTIMODE does not allow automatic detection of degenerated states and does not even produce correct degeneracy patterns for higher excited states. Some higher excited modes split. This can be seen in table 3.4 for example for the 0300 mode. 0100 is an E mode. That means there are two degrees of freedom with the same energy (0+1 and 1+0). The overtone 0200 can be formed either by two excitations from one of these degrees of freedom (0+2 and 2+0), or one each (1+1). This mode therefore splits in an E and an A_1 mode

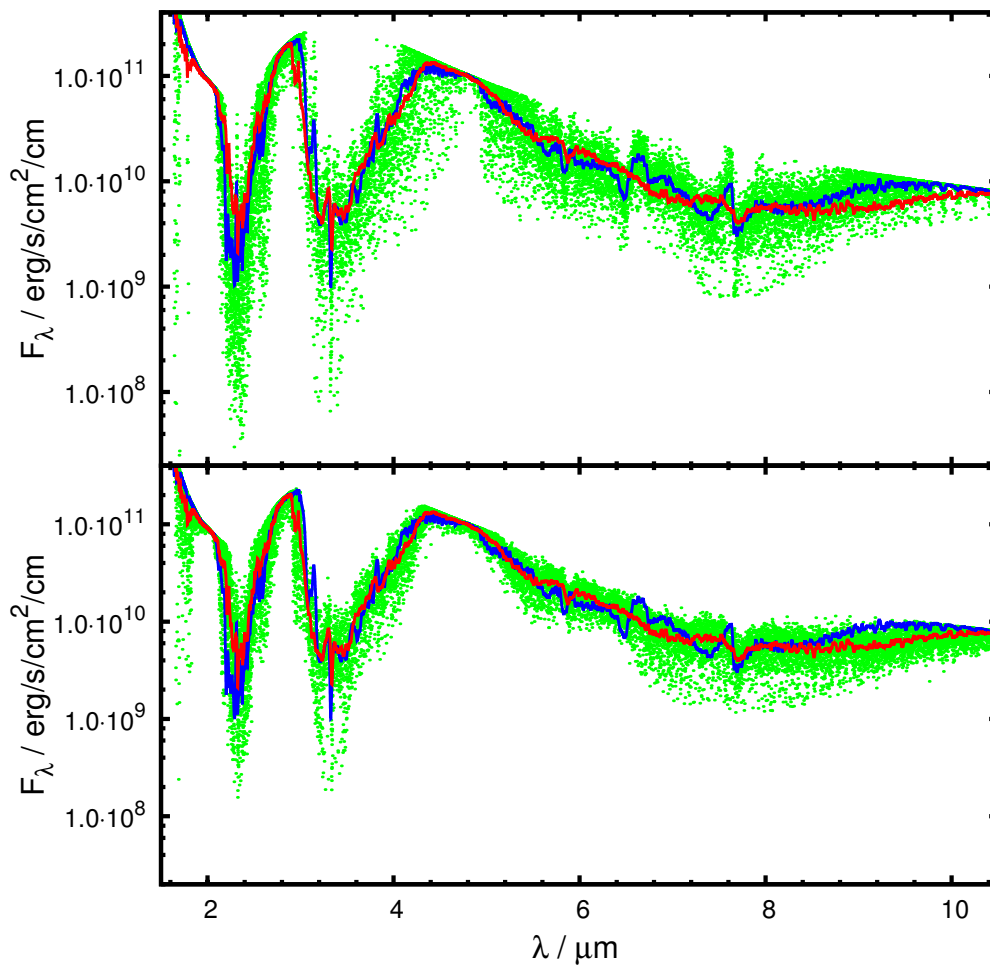


Figure 3.9: Radiative flux distribution as a function of wave length for 1000 K. Only methane absorption lines are shown. Upper part: HITRAN2004, lower part: this work. Blue and red lines: averages for HITRAN2004 and Warmbier *et al.* lines, respectively.

with different energies. 0300 splits into three different modes and so on. This could not be treated correctly, but the average energy of these was used. Therefore, it is not sensible to use the new potential to redo the line list calculations with MULTIMODE as the improved quality of the potential would be taken away by the averaging process.

While the limited numerical possibilities limit the quality of the methane line list, this does not make it less important. While single line position might not be accurate there are applications where other properties are more important. In the case of radiation transport calculations for brown dwarfs, as have been performed by Hauschildt *et al.* [51], the completeness of line lists are very important. The HITRAN[53, 54] database offers line lists for 39 different molecules. This and other databases depend on experimentally measured and/or calculated transition information. Usually the emphasis is on accurate line positions of few lines. For radiation transport, as mentioned, it is more important

to have complete lists. An incomplete list, like shown in figure 3.8 for HITRAN2004, causes unnatural gaps in the spectra. The line list from this work fills the gaps, which can be found around $2\mu\text{m}$ and between 10 and $20\mu\text{m}$ in the HITRAN2004 database. The impact of these gaps can be observed in radiation transport calculations. Figure 3.9 compares radiative fluxes calculated for brown dwarf atmospheres at 1000 K. To improve the visual impression, only methane lines were used. It can be seen that the HITRAN data has radiative holes, which are not presented in the new line list. As a consequence the temperature profile of the atmosphere changes. In this case local temperatures diverged up to 80 K between the models.

3.4 Recap

The calculation of *ab initio* data and the fitting of potential surfaces (PES) are the first two steps in the work flow (see figure 1.1) of this thesis. They are prerequisites for any spectroscopic or reactive calculation. In this chapter potential energy surfaces for small hydrocarbons were presented. These potentials were fitted from high level *ab initio* data. It could be shown, that they provide accurate equilibrium configurations and vibrational energies. The chosen *ab initio* method needs a Hartree-Fock reference wave function, which is a good initial guess. This is not the case for the (pre-)dissociation parts of the configuration space, where this method can not be used. It could be shown, that a cluster expansion of the potential in fragments can partly overcome this problem. This makes the CH_2 PES suitable for spectroscopic as well as reactive purposes. The CH_3 and CH_4 potentials are limited to spectroscopic studies only, because not all fragments could be sufficiently included by the cluster expansion.

While polyatomic molecules are mainly interesting for infrared spectroscopy, the inclusion of electronic transitions will be discussed for diatomic molecules in the next chapter, which is taking the step from fitting and rovibrational energies to rovibronic line lists and photodissociation.

4 Spectroscopic and photodissociation studies of magnesium hydride

In the last chapter applications of *ab initio* and potential fitting methods were presented. The potential energy surfaces of hydrocarbons were used for rovibrational spectroscopy. This chapter extends the application of computational chemical physics to rovibronic transitions of diatomic molecules. It completes the first branch in the work flow of this thesis (see figure 1.1).

Cold stellar atmospheres and gas giants can contain a large diversity of molecules. Many of these are diatomic molecules like metal hydrides and metal monoxides. While computational spectroscopy for larger molecules is limited to rovibrational transitions, it is possible to calculate electronic transitions for diatomic molecules. In this work a code was developed which can calculate complete lists of transitions with Einstein coefficients and oscillator strengths for a number of given electronic states as well as bound-continuum photodissociation cross sections. The MgH molecule was chosen as an example. This molecule is of vital interest for astrophysics. MgH has been found in the sun and the atmospheres of many cold stars. MgH lines are even prominent in spectra from other galaxies. Its spectra can be used to determine the relative abundance of Mg isotope in stellar atmospheres. Together with other metallic diatomic molecules MgH is used as an indicator for the relative abundance of metals in stellar atmospheres. In addition to the importance of MgH there are older theoretical works available, which can be used for comparison and validation of this work.

4.1 Methods

The computational strategy for this project is as follows. First a set of *ab initio* data has to be acquired, including energies, dipole moments and transition dipole moments between the electronic states. The accuracy required for spectroscopy is beyond the limits of fitting

procedures for potential energy surfaces. Therefore, a cubic spline interpolation is used in this case. It is notable, that this is only possible due to the low dimensionality of the configuration space, namely one-dimensional. For larger numbers of coordinates fitted potentials can not be avoided. The rovibronic eigenstates and transitions are obtained using a Lagrange mesh method.

4.1.1 Choice of *ab initio* method

The ground state of MgH $X^2\Sigma^+$. All higher bounded states are also doublet states. The lowest excited states A $^2\Pi$ and B' $^2\Sigma^+$ have the same dissociation limit. These three states have been subject to previous spectroscopic studies and are therefore suited for the validation of the code. This work also includes the E $^2\Sigma^+$ and C $^2\Pi$ states. While these states are relatively high in energy they may be accessed by energetic photons, by two-photon excitation or by two-photon photodissociation.

The difficulty in *ab initio* calculations for several electronic states is the quality of the resulting energies. The calculation is a three step process. For a certain atomic configuration a Hartree-Fock calculation of the ground state is performed. This calculation yields canonical orbitals, molecular orbitals with integer occupation numbers, as described in section 2.1.2. These are taken as a starting guess for a state-averaged multi-configurational self consistent field (MCSCF) calculation. In a MCSCF (see section 2.1.4.4) molecular orbitals (MO) and electron densities are obtained using more than one Slater determinant. If more than one electronic state is requested the molecular orbitals are averages over all these states. In the third step these MOs are taken as basis for the MRCI calculations (see 2.1.4.4). If the MO basis is an average over several states this can have an influence on the final MRCI energies. The MCSCF and MRCI states do not necessarily coincide. In seldom cases the inclusion of an additional MCSCF state can enter contributions to the basis, needed for the MRCI to converge to the correct state. Yet it is more probable, that the state averaging causes the basis to be non-optimal for a specific state. This would cause a less optimised MRCI energy. If one wants to calculate more than one state of the same irreducible representation this can hardly be avoided, as one can not skip roots in the MCSCF part. The most important reason for this work is though, that state averaged MOs are a prerequisite for the calculation of transition dipole moments between electronic states. It is not possible to compare two states described by different bases.

The next consideration is the size of the active space. This is the set of molecular orbitals which are optimised and occupied. If the set is chosen small the expansion of orbitals is insufficient to represent all states properly and one obtains wrong energies. If the set is chosen too large the computational costs increase dramatically and the computational

algorithm might fail to converge, as the higher orbitals are practically unoccupied and the numerical algorithm can sometimes not decide which orbital to include and which to exclude. Moreover steps in the potential might occur, as the *ab initio* has an irregular convergence. This can also happen if the chosen active space is only suited for a part of the configuration space, like the near equilibrium part. While going to the dissociation limit the electronic structure changes and molecular orbitals get replaced by other ones, causing steps. An additional restriction lies in the symmetry requirements. Taking the example of a diatomic molecule. The largest Abelian point groups usually implemented in computer programs are D_{2h} and C_{2v} . In C_{2v} the s orbitals are of the irreducible representation A_1 . The p orbitals split in p_z , p_x and p_y which have irreducible representations A_1 , B_1 and B_2 . If a p_z orbital is included, it is advisable to include also the p_x and p_y orbitals, else the calculation is unbalanced. In the case of diatomic molecules the expectation value of the angular momentum along the z -axis, L_z^2 , is non integer for unbalanced active spaces or unpropitious chosen combination of states, e.g. only one of two (nearly) degenerate states of different L_z^2 are included.

The Dunning-type correlation consistent basis sets[6, 55] offer the best quality for a number of basis functions. The largest set available are aug-cc-pV6Z and aug-cc-pWCV5Z for hydrogen and magnesium, respectively. As a rule of thumb it is recommended to use the same level of basis set for all atoms. The Dunning basis sets are composed in a way that going from one level to the next, atomic orbitals are added which recover approximately the same amount of correlation energy. If a larger set is used for one atom the binding is tweaked towards this atom, which changes results. The MCSCF for the five states does not converge for large parts of the configuration space, if a 5- ζ basis for magnesium is used. Therefore, the aug-cc-pVQZ and aug-cc-pWCVQZ for hydrogen and magnesium were used.

4.1.2 Lagrange Mesh Solver for the molecular Schrödinger equation

The time-independent molecular Schrödinger equation for MgH solved in this work is:

$$\left\{ -\frac{\hbar^2}{2\mu} \frac{d^2}{dr^2} + V(r) + \frac{\hbar J(J+1)}{2\mu r^2} - E_{v,J} \right\} \Psi_{v,J}(r) = 0, \quad (4.1)$$

with the interatomic separation r , the reduced molecular mass μ and the rotational and vibrational quantum numbers J and v . This equation neglects effects like spin-orbit coupling, spin-rotation coupling and Born-Oppenheimer breakdown effects. This differential equation can be solved using the Lagrange mesh method as described in section 2.3. The computer program written for this work uses a constant step Lagrange mesh for central

potentials derived by Baye[18]. The mesh is defined in equation (32) in the paper of Baye[18] and is presented here briefly.

The basis uses orthonormal sine functions of the form

$$\Phi_k = \sqrt{2} \sin(\pi(k - 1/2)x), \quad (4.2)$$

with $k = 1, \dots, N$, which are defined in the interval $[0, 1]$. The functions vanish at 0 and their first derivatives at 1. The interval can be scaled to fit the needs of physical systems. The choice of sine basis functions is advantageous, because the wave functions have a sinusoidal form. Another common choice are orthogonal polynomial basis functions. They are usually not equally spaced and therefore represent certain parts of the configuration space better than others. For example Hermite polynomials are suited for bound rovibrational wave functions. The mesh points for the sine basis are defined as

$$x_i = \frac{i}{N}, \quad (4.3)$$

with weights

$$\lambda_i = \frac{1}{(1 + \delta_{iN})N}. \quad (4.4)$$

The weight for x_N is reduced as this point is at the upper boundary of the interval. For the kinetic energy matrix $T = -d^2/dx^2$ the off-diagonal matrix elements are given by

$$T_{ij} = (-1)^{(i-j)} \frac{\pi}{2} \left[\frac{\cos(\frac{\pi}{2}(x_i - x_j))}{\sin^2(\frac{\pi}{2}(x_i - x_j))} - \frac{\cos(\frac{\pi}{2}(x_i + x_j))}{\sin^2(\frac{\pi}{2}(x_i + x_j))} \right] \frac{1}{\sqrt{1 + \delta_{iN}}} \frac{1}{\sqrt{1 + \delta_{jN}}}. \quad (4.5)$$

The diagonal matrix elements are given by

$$T_{ii} = \frac{\pi}{2} \left[\frac{1}{6}(4N^2 - 1) - \frac{\cos(\pi x_i)}{\sin^2(\pi x_i)} \right] \quad (4.6)$$

for $i < N$ and by

$$T_{NN} = \frac{\pi}{12}(4N^2 - 1). \quad (4.7)$$

The matrix form of the Hamiltonian leads to a standard eigenvalue problem, where the eigenstates are the vibrational energy levels for a given rotational quantum number. The eigenvectors are the approximate values of the wave function at the mesh points. The system is solved using the SYEVR Lapack routine¹ for a given number of eigenvalues. This routine calculates eigenvalues and eigenvectors, if desired, of a square real matrix. The computed eigenvectors are orthonormal. The routine allows to specify the number of eigenvalues which shall be calculated. The output wave functions already contain weights

¹see <http://www.netlib.org/lapack/double/dsyevr.f>

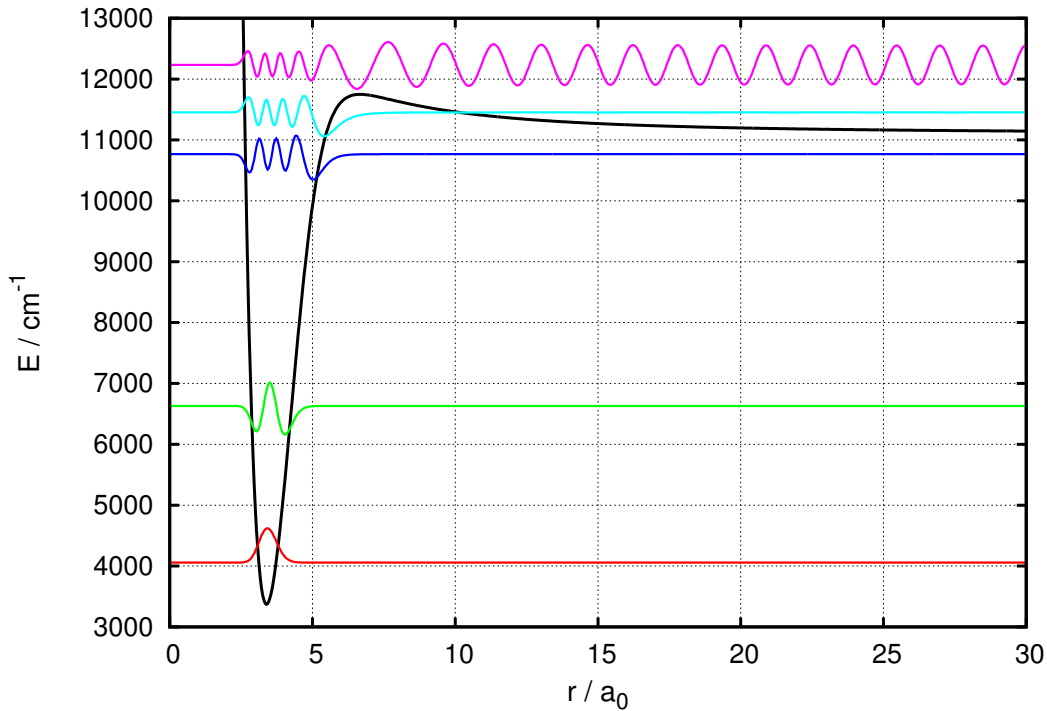


Figure 4.1: Effective potential energy curve (black) of the electronic ground state for $J = 24$. Bound wave functions for $v = 0$ (red), $v = 2$ (green) and $v = 6$ (blue) are given. The wave function for $v = 7$ (light blue) is quasi-bound. A continuum wave function (purple) is given too. The base lines are shifted corresponding to the vibrational energies. Amplitudes are magnified.

$\lambda_i^{1/2}$, which has to be taken into account for the calculation of expectation values.

There are three distinguishable solutions for the Schrödinger equation: bound, quasi-bound and continuum solutions.

Figure 4.1 shows examples for all three types of solutions for the $J = 24$ levels of the electronic ground state. The effective potential is shown, which is the sum of the adiabatic electronic potential and the rotational energy. The bound solutions are levels with an energy lower than the dissociation limit. The lower three wave function in figure 4.1 are bound. These levels are stationary solutions and represent the normal rovibrational levels. As the wave functions are naturally limited by the potential, the domain boundary conditions are irrelevant. Continuum solutions have an energy larger than the dissociation limit. The uppermost wave function in figure 4.1 is a continuum solution. Their time-independent wave functions behave asymptotically as

$$\Psi_{k,J}(r \rightarrow \infty) = \left(\frac{2\mu}{\pi\hbar^2 k} \right)^{1/2} \sin\left(kr - \frac{\pi}{2}J + \delta_{k,J}\right), \quad (4.8)$$

where $k = \sqrt{2\mu E}/\hbar$ is the wave number of the continuum wave function and E is the energy of the continuum wave function measured from the dissociation limit of the potential. The factor $\sqrt{2\mu/\pi\hbar^2 k}$ is the square root of the density of states $\rho(E)$. The wave functions from the Lapack routine are normalised such that $\sum_{i=1}^N |\Psi(x_i)|^2 = 1$. As this normalisation is wrong for continuum wave functions, they have to be renormalised. For this the information about the actual asymptotic amplitude is needed, which is extracted from the amplitude of the last extremum of the wave function in the interval. The above mesh was chosen, because it guarantees an extremum at the outer boundary of the interval. The wave functions take the form (4.8) only at a certain distance, which depends on the potential and the energy of the continuum solution. Especially for rotational excited states the centrifugal potential shifts this point to larger distances. As the number of periods in the calculation box $[0, r_{max}]$ increases by one for each eigenstate, high lying continuum solutions will have an extremum near r_{max} in any case. For the low lying eigenstates this is different. The lowest continuum solution has one extremum outside the potential well, but may have several within the well. If the boundary condition was $\Psi(r_{max}) = 0$, this extremum would be somewhere in the middle of the configuration space, where it might not be asymptotic. This is avoided by the condition $\Psi'(r_{max}) = 0$, which forces the extremum to be the last mesh point.

The third kind of possible solutions are quasi-bound states. The rotational energies can be interpreted as a centrifugal potential, which adds to the adiabatic potential and forms an effective potential, as in figure 4.1. For large rotational quantum numbers the effective potential shows a reduced depth and a potential wall in the pre-dissociation regions, which can be significantly higher than the dissociation limit. This wall allows stationary solutions above the dissociation limit, as shown by the second highest wave function in figure 4.1. The wall has a limited width, therefore there is a certain tunnelling probability. The numerical procedure used in this work does deliver all three kinds of solutions. The handling of the quasi-bound states is difficult. There is no direct information about the expected dissociation life time of such a state, therefore it is hard to decide whether transitions involving such states should be included in the line lists or not. Shayesteh *et al.*[56] experimentally found some, but by far not all, of the quasi-bound states they predicted. All states are assigned a tag "b" and "q" whether they are bound or quasi-bound. This offers full flexibility for the future usage of the line lists.

4.1.3 Radiative oscillator strength and photodissociation cross sections

The Lagrange-mesh solver delivers the wave functions and eigenvalues for the rovibrational levels νJ of the electronic states n . With the dipole moments and transition dipole moments from the *ab initio* calculations transition dipole matrix elements $|D_{\nu'J',\nu''J''}^{n',n''}|^2 = |\langle \Psi_{\nu'J'}^{n'} | D^{n',n''}(r) | \Psi_{\nu''J''}^{n''} \rangle|^2$ can be calculated. Information about the spectroscopic line strengths are given by the line absorption oscillator strength

$$f_{\nu'J',\nu''J''}^{n',n''} = \frac{2}{3} \Delta E_{\nu'J',\nu''J''}^{n',n''} \frac{1}{2J''+1} S_{J'}(J'') |D_{\nu'J',\nu''J''}^{n',n''}|^2 \quad (4.9)$$

and the Einstein coefficient for spontaneous emission, or line transition probability, is

$$A_{\nu'J',\nu''J''}^{n',n''} = \frac{2}{c^3} (\Delta E_{\nu'J',\nu''J''}^{n',n''})^2 \frac{2J''+1}{2J'+1} f_{\nu'J',\nu''J''}^{n',n''} / t_{au}, \quad (4.10)$$

as defined by Larsson[57]. The energetic lower state is conventionally assigned the double primes. The factor $t_{au} \approx 2.42 \cdot 10^{-17}$ s is the atomic time unit in seconds. $S_{J'}(J'')$ are the Hönl-London[58] factors as defined by Hansson and Watson[59]. All right hand side units are expected to be atomic units, with $c = 1/\alpha$. The oscillator strength has no unit and the Einstein coefficient is given in s^{-1} . The bound-continuum photodissociation is described by the photodissociation cross section

$$\sigma_{\nu''J''}^{n',n''} = \frac{\pi}{3c} \Delta E_{k'J',\nu''J''}^{n',n''} \frac{1}{2J''+1} \sum_{J'=J''-1}^{J''+1} S_{J'}(J'') |D_{k'J',\nu''J''}^{n',n''}|^2. \quad (4.11)$$

If cross sections in the unit cm^2 are desired, the factor $\frac{\pi}{3c}$, including unit transformations, has the numerical value of $2.689 \cdot 10^{-18}$.

4.2 Results

4.2.1 *Ab initio*

The *ab initio* electronic potentials, dipole moments and transition dipole moments were calculated at 262 points in the interval between $1.8a_0$ and $32.6a_0$ using the MOLPRO2010 program package[28]. The *ab initio* potentials are compared with experimental data. The experimental reference data were taken from Shayesteh *et al.*[56], who provided data for the X $^2\Sigma^+$ state. Fragmentary data for the A $^2\Pi$ and B' $^2\Sigma^+$ states could be derived from the supplementary line list. Their dissociation energies D_e and the (0;0)→(0;0) excitation energies T_e differ significantly from older experimental results from Balfour *et*

al.[60–62]. A comparison of potential characterisations is given in table 4.1 and vibrational energies are given in table 4.2. As can be seen from the tables, the *ab initio* data shows an overestimation of binding energies for the lowest three electronic states. The equilibrium distances are too far and the potential wells are too wide. This effect increases with the approach of the basis set limit. This suggests that either one or both of the bases are not entirely suited for this molecule or that the *ab initio* methods are not exact enough. According to Shayesteh *et al.* the dissociation energy of the electronic ground state is 11104.5cm^{-1} . Different combinations of correlation consistent basis sets yield dissociation energies between 11400cm^{-1} and 11600cm^{-1} . This large discrepancy is not a problem of unbalanced basis set sizes, but rather an intrinsic error in at least one basis set or a problem of the *ab initio* method.

In order to improve the electronic potentials the *ab initio* was scaled and morphed linearly to fit experimental data as good as possible. *Ab initio* results usually do not agree exactly with experimental data. If enough experimental information is available, this can be used to adapt the *ab initio* potential accordingly. In this case, the procedure is as follows: First the ground state dissociation energy is fitted by applying a factor D_e^{exp}/D_e^{ab} to the potential values, which is the ratio of experimental and *ab initio* dissociation energies. Now the coordinate r is scaled ($\tilde{r} = m \cdot r$) such, that the vibrational energies of the ground state fit as good as possible to the experimental data. An offset is given afterwards ($\tilde{r} = m \cdot r + n$) such, that the equilibrium distance matches experimental values. This scaling of the coordinate is applied to all potentials and dipole moments, as electronic transitions could not be calculated otherwise. The excited states vibrational levels can now be adapted by changing T_e and D_e . The scaling and offset factors are given in table 4.3. It has to be clarified, that this morphing of potentials, although common in computational chemistry, is rather over-estimated and a source of errors and false conclusions.

In this case, the ground state vibrational energies (see table 4.2) are all improved compared to the unscaled potential. Larger deviations, between 11 and 14cm^{-1} , remain for vibrational states between $v = 8 - 10$. The error is not increasing linearly or quadratically with the vibrational energy, but shows a more erratic character. This indicates that not all parts of the configuration space are of equal quality. Especially the high energy predissociation regions might show larger errors, as the strongly mixed electronic states are more difficult to describe in the molecular orbital basis. Tendency is, that the basis is less complete for these cases.

Table 4.1: Comparison of dissociation energies D_e , electronic energy difference T_e and equilibrium distance r_e between *ab initio* (ab), scaled *ab initio* (sc) and experimental results from Shayesteh *et al.*[56] and Balfour *et al.*[60–62]. All energies are in cm^{-1} and distances in a_0 .

	D_e^{ab}	T_e^{ab}	r_e^{ab}	D_e^{sc}	T_e^{sc}	r_e^{sc}	D_e^{exp}	T_e^{exp}	r_e^{exp}
X $^2\Sigma^+$	11453	—	3.290	11104.5	—	3.269	11104.5[56]	—	3.269[56]
A $^2\Pi$	13579	18943	3.196	13362.1	19273.8	3.178	n.a. 13640 \pm 250[62]	19273.2[56] 19278[61]	n.a. 3.173[61]
B' $^2\Sigma^+$	10272	21869	4.969	10220.9	22083.2	4.916	n.a. 10790 \pm 250[62]	22082.4[56] 22410[61]	n.a. 4.906[61]
E $^2\Sigma^+$	10879	35151	3.183	—	—	3.164	n.a.	35551[61]	3.156[61]
C $^2\Pi$	4467	41616	3.149	—	—	3.132	n.a.	41240[61]	3.178[61]

Table 4.2: Numerical vibrational energies (in cm^{-1}) before and after morphing and experimental values from Shayesteh *et al.*. For A $^2\Pi$ and B' $^2\Sigma^+$ only values up to $\nu = 3$ are available. Energies are given relative to the zero point energy of the electronic ground state.

	ν	<i>Ab initio</i>	morphed	exp.
X $^2\Sigma^+$	0	737.52	740.74	739.11
	1	1428.58	1433.10	1431.98
	2	2793.80	2800.18	2800.68
	3	4094.98	4100.49	4102.33
	4	5329.79	5330.69	5331.39
	5	6488.47	6480.06	6479.65
	6	7562.03	7538.02	7534.81
	7	8533.47	8484.60	8478.00
	8	9378.96	9290.54	9279.65
	9	10058.93	9907.01	9892.72
	10	10511.28	10260.65	10249.39
	11	10686.44	10354.73	10352.23
	12	10715.18	—	—
A $^2\Pi$	0	18942.97	19273.83	19273.23
	1	20461.17	20808.69	20807.72
	2	21914.57	22276.07	22273.71
	3	23301.50	23673.53	23665.89
B' $^2\Sigma^+$	0	21868.52	22083.24	22082.36
	1	22660.97	22889.35	22887.47
	2	23431.21	23672.34	23671.47
	3	24179.57	24432.61	24428.04

Table 4.3: Scaling and morphing factors for the coordinate r and the potential energies.

	scaling	offset
r	0.98	$0.0455 a_0$
X $^2\Sigma^+$	0.969580	—
A $^2\Pi$	0.984	0.003610 au
B' $^2\Sigma^+$	0.995	0.002793 au

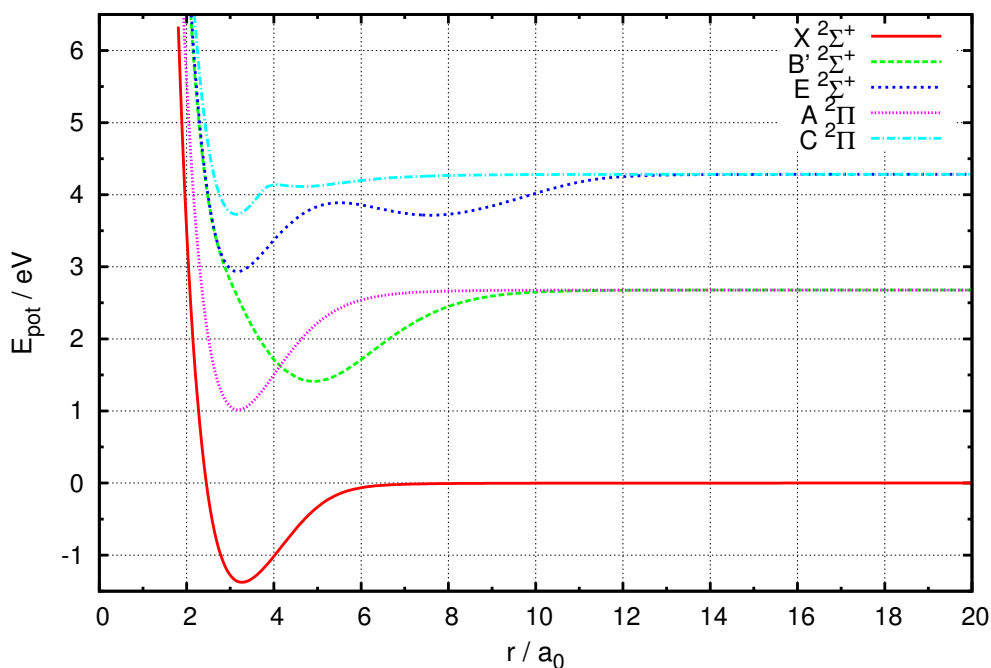


Figure 4.2: Potential energy curves for the five lowest doublet states of MgH.

The scaling of the coordinate has to be applied to all electronic states. The r_e are now nearer to the experimental values, besides the $r_e(C^2\Pi)$, which was already slightly underestimated before. The potentials of $A^2\Pi$ and $B'^2\Sigma^+$ were adapted to fit the experimental vibrational levels of Shayesteh *et al.* as shown in table 4.2. The agreement is within few cm^{-1} , which is satisfactory compared to the agreement of the ground states. It has to be noticed although, that this does not guarantee agreement with other experimental values, which are not available yet. It also does not mean, that the dissociation energy must be correct. The morphed dissociation energies are about 280cm^{-1} and 570cm^{-1} smaller than the ones measured by Balfour and Lindgren. Yet these data have been assigned a large uncertainty of 250cm^{-1} . Together with the fact, that even the T_e of $B'^2\Sigma^+$ shows a difference of about 230cm^{-1} between Shayesteh *et al.* and Balfour and Cartwright, this puts the results of Balfour and Lindgren in doubt. For the $E^2\Sigma^+$ and $C^2\Pi$ states only data from Balfour and Cartwright is available. This is not considered reliable, or at least not necessarily better than the *ab initio* data of this work. Therefore, no scaling of D_e or T_e has been applied for these electronic states.

The final potential energy curves are shown in figure 4.2 and the corresponding dipole moments are shown in figure 4.3. The ground state of MgH has a single-welled, Lennard-Jones-like potential curve, which enters the dissociation region around $8a_0$. The minimum lies at $3.269a_0$ and is $11104.5\text{cm}^{-1} = 1.37675\text{eV}$ deep. The dipole moment along

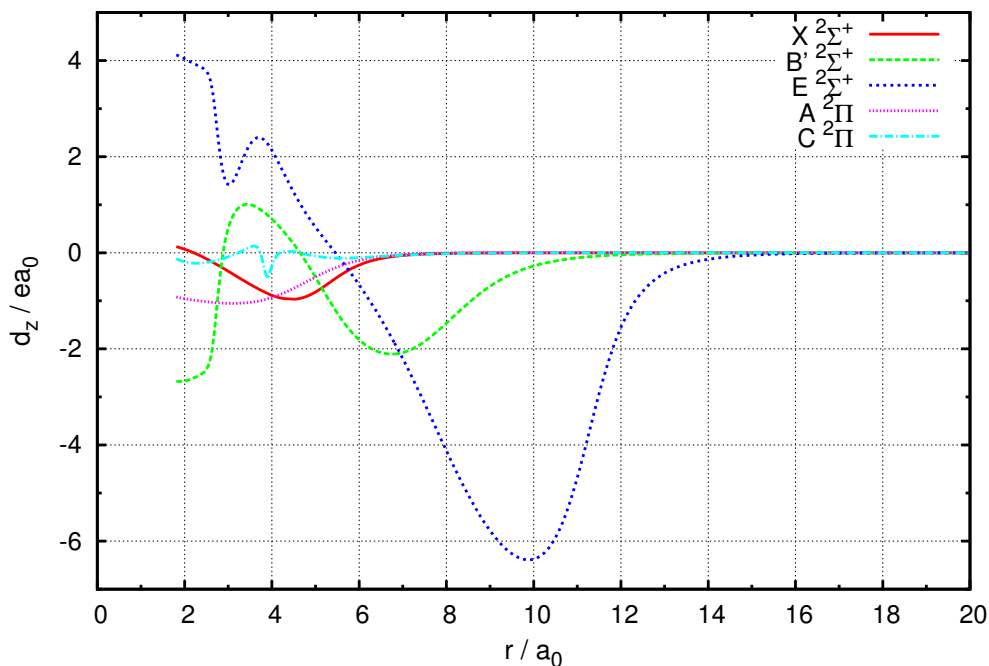


Figure 4.3: Dipole moments for the five lowest doublet states of MgH along the Mg-H axis. The dipole moments are given in the atomic unit elementary charge times Bohr.

the axis of symmetry is negative, with the extremum $d(4.5 a_0) = -0.963$ au. This weak dipole moment results from the charge transfer to the hydrogen atom. The $A^2\Pi$ state has a tighter well for low energies, but a wider pre-dissociation region. Its minimum is located at $3.178 a_0$ with a depth of $13362.1 \text{ cm}^{-1} = 1.65665 \text{ eV}$. The rovibrationless excitation from the ground state has an energy of $19273.8 \text{ cm}^{-1} = 2.38959 \text{ eV}$. The dipole moment is weak, as for the ground state, with the minimum of $d(3.68 a_0) = -1.05$ au. The $B'^2\Sigma^+$ state has the same dissociation limit as the $A^2\Pi$ state. Its minimum is at a larger distance of $4.916 a_0$ with a potential depth of $10220.9 \text{ cm}^{-1} = 1.26720 \text{ eV}$. The potential is broader than the first ones and reaches its dissociation regions as far as $10 a_0$. The ground state excitation energy is $22083.2 \text{ cm}^{-1} = 2.73790 \text{ eV}$. The dipole moment is negative for small distances and shows a strong gradient around $2.5 a_0$ and a maximum at $3.43 a_0$, where it increases from ≈ -2.5 au to 1.010 au. In this region the $B'^2\Sigma^+$ shows a strong interaction with the $E^2\Sigma^+$ state. After that maximum the dipole moment is decreasing until $6.71 a_0$, where it has a minimum with -2.0 au. The dipole moment is non-zero up to approximately $13 a_0$. The $E^2\Sigma^+$ is a double well state. Besides its global minimum at $3.164 a_0$ it has a local minimum at $7.59 a_0$. The dipole moment is overall strong. It starts from 4 au at $2 a_0$ and decreases to -6.4 au at $9.85 a_0$. There is a local minimum at $3.03 a_0$ due to the interaction with the $B'^2\Sigma^+$ state. The zero-crossing of the dipole has the same location as the local maximum of the potential between the wells at $\approx 5.5 a_0$. From this point on

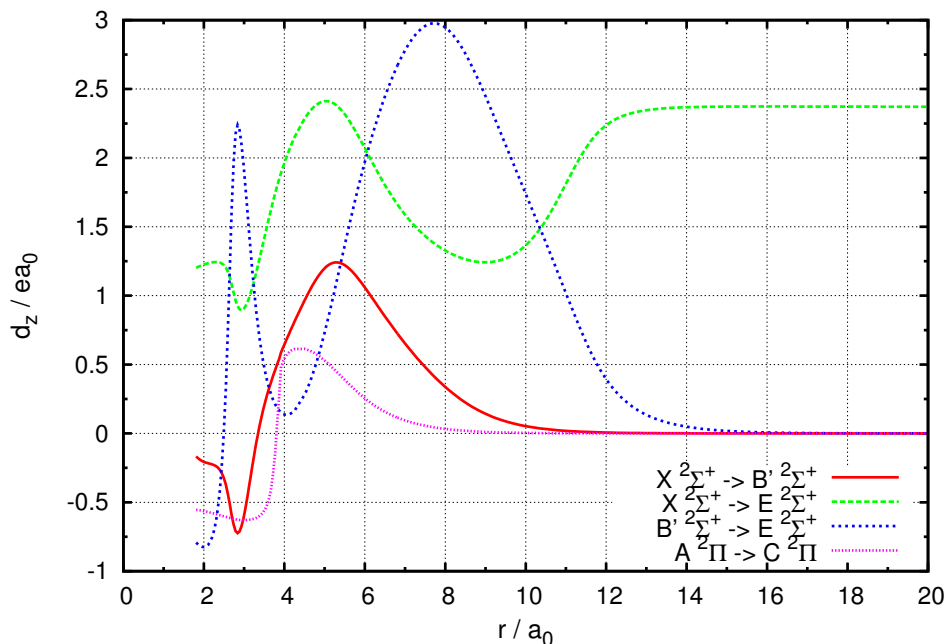


Figure 4.4: Transition dipole moments for the perpendicular transitions between the five lowest doublet states of MgH.

this state develops a strong ionic character, which diminishes only at $16a_0$. The highest state in this work, $C^2\Pi$, is also the weakest bound one. The minimum at $3.132a_0$ is only $4467\text{cm}^{-1} = 0.5538\text{eV}$ deep. A second, very shallow, minimum is located at $4.65a_0$. The barrier to the local maximum in between is only $202\text{cm}^{-1} = 0.0250\text{eV}$ high. The dipole moment is very weak, with several extrema. The strongest point at $3.97a_0$, near the local maximum, has a dipole moment of -0.42au .

The intensity of electronic transitions strongly depends on the transition dipole moment between these states. The sign of these moments depends on the relative phase of the electronic wave functions involved and does not carry physical information. Extrema often correspond to extrema in one of the potentials. The electronic rotational momentum Λ is either 0 (Σ states) or 1 (Π states) for the electronic states in this work. As transitions are allowed for $\Delta\Lambda = 0, \pm 1$, all five electronic states in this work are connected. Transitions with $\Delta\Lambda = 0$ are called perpendicular and $\Delta\Lambda = \pm 1$ transitions are orthogonal. The perpendicular transition dipole moments are shown in figure 4.4. The largest amplitudes of the transition dipole moments vary between 0.6au and 3au . The strongest two dipole moments appear for the $E^2\Sigma^+ \leftarrow X^2\Sigma^+$ and $E^2\Sigma^+ \leftarrow B'^2\Sigma^+$ transitions, while the $B'^2\Sigma^+ \leftarrow X^2\Sigma^+$ transition dipole moment is a factor of two smaller. The $E^2\Sigma^+$ state tends to have reasonable transition dipole moments with all states, because the double-well structure covers all the configuration where the other potentials have their wells. In

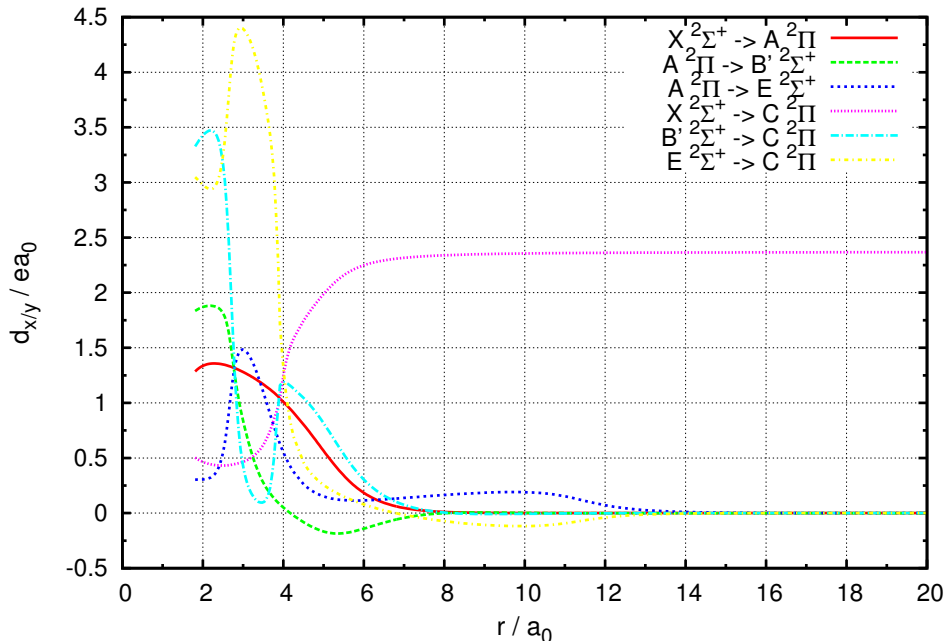


Figure 4.5: Transition dipole moments for the orthogonal transitions between the five lowest doublet states of MgH.

contrast to this the wells of $X^2\Sigma^+$ and $B'^2\Sigma^+$ are shifted relative to another. The states can only couple around the global minimum of $B'^2\Sigma^+$, as can be seen in figure 4.4 from the maximum around $5a_0$. The $E^2\Sigma^+ \leftarrow X^2\Sigma^+$ transition has a finite transition dipole moment of $2.4a_0$ for $r \rightarrow \infty$, which is the atomic transition dipole moment between the Mg ($3s^2\ ^1S$) and Mg ($3s3p\ ^1P$) states. The weakest orthogonal transition dipole moment belongs to the $C^2\Pi \leftarrow A^2\Pi$ transition. Its two amplitudes are about $0.6a_0$ strong, each located approximately at one minimum of $C^2\Pi$.

The orthogonal transition dipole moments are shown in figure 4.5. The amplitudes are in the same ballpark as the perpendicular ones. The $C^2\Pi \leftarrow B'^2\Sigma^+$ transition has a maximum transition dipole moment of almost $3.5a_0$, but at a distance of approximately $2.2a_0$ which is too small to play an important role, as the $B'^2\Sigma^+$ well is at a relatively large distance. The $E^2\Sigma^+ \leftarrow C^2\Pi$ transition has a very strong transition dipole moment of $4.4a_0$ at $3a_0$. The $C^2\Pi \leftarrow X^2\Sigma^+$ shows the same asymptotic transition dipole moment as $E^2\Sigma^+ \leftarrow X^2\Sigma^+$, because of the asymptotic atomic state of both final states.

4.2.2 Rovibrational states

For the five electronic states all together 2531 bound and 464 quasi-bound rovibrational levels were calculated. Quasi-bound states were only included, if their $\langle r \rangle$ is smaller than a threshold. This distance is different for each electronic state and also depends on

Table 4.4: Maximal vibrational ($J = 0$) and rotational ($v = 0$) quantum numbers and numbers of bound and quasi bound states. The maximal expectation value for r , for which a state is considered quasi-bound, is also given.

	v_{max}	J_{max}^{bound}	J_{max}^{quasi}	n_{bound}	n_{quasi}	$\langle r \rangle_{max}^{quasi} (a_0)$
X $^2\Sigma^+$	11	44	56	318	57	$\min(12, 14.32x^{-0.385} + 1.2)$
A $^2\Pi$	13	48	58	415	64	$\min(9, 14.74x^{-0.304})$
B' $^2\Sigma^+$	18	65	83	743	139	$\min(14, 17.99x^{-0.232})$
E $^2\Sigma^+$	24	67	95	929	191	18; 10 for $J \geq 20$
C $^2\Pi$	8	24	26	126	13	20

the rotational quantum number. If one plots $\langle r \rangle$ over the rotational quantum number for all eigenvalues of one electronic state, one finds patterns. For a given value of J , the vibrational levels have an increasing $\langle r \rangle$ and each vibrational eigenstate has an increasing $\langle r \rangle$ with increasing J . The increase of $\langle r \rangle$ for increasing v is caused by the anharmonicity of the potential. The inner wing is increasing faster than the outer wing. Therefore higher energy states are located more outwards. Some of the localised eigenstates above the dissociation limit have an $\langle r \rangle$ which is the continuation of one of these patterns. Those are chosen as quasi-bound states in this work. This is a conservative treatment as the included quasi-bound states behave like bound ones and this excludes some of the higher quasi-bound states, which have a larger $\langle r \rangle$. Higher quasi-bound states tend to have larger amounts of their wave function beyond the centrifugal wall. These states dissociate after a certain time, which disqualifies these states for bound-bound transitions. The number of bound and quasi-bound states, as well the $\langle r \rangle$ -thresholds, are given in table 4.4.

Figure 4.6 shows the energy of the bound and quasi-bound rovibrational eigenstates of X $^2\Sigma^+$ versus the rotational quantum numbers of these states. The dissociation energy is also indicated. The energy levels show the expected behaviour for single-well potentials. Harmonic oscillator energy levels are equally spaced. Real potentials are anharmonic, which causes the energy difference between successive levels to decrease with energy. The energies of the eigenstates increase quadratically with J . The rotational excitation also shrinks the energy difference between vibrational levels of the same rotational energy. There are no states with energies lower than the dissociation energy for $J > 44$. As can also be seen from figure 4.6, starting with $J = 13$ some of the listed states have energies larger than the dissociation limit. These quasi-bound states get more with larger rotational energy, until they disappear together with the centrifugal wall. For X $^2\Sigma^+$ the largest J with quasi-bound state, according to the definition from the beginning of this section, is $J = 56$. Table 4.4 gives the largest vibrational, bound and quasi-bound rotational levels for all electronic states.

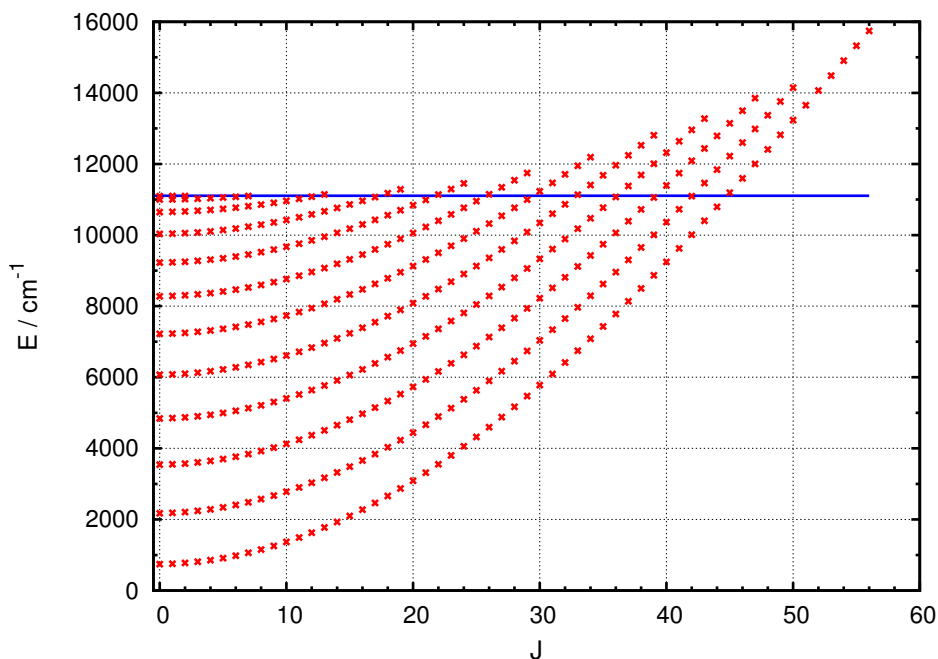


Figure 4.6: Energies of the (quasi-) bound rovibrational eigenstates of $X^2\Sigma^+$ relative to the potential minimum over the rotational quantum numbers. The dissociation energy is the horizontal line.

It is worth to mention, that the pattern is more complicated for multi-well potentials. As can be seen in figure 4.7 for the $E^2\Sigma^+$ state, the double-well causes two overlaying single-well patterns. For low energies only the deepest well is responsible for the eigenvalues and a clear single-well pattern exists, in this case up to approximately 6400cm^{-1} above the global potential minimum. Higher vibrational eigenstates show a strongly increased density of states, as the potential is effectually broadened. The rotational pattern looks, as mentioned above, like the overlay of two single-well potentials. This also means, that double-well potentials usually have much more rovibrational eigenstates, bound and quasi-bound ones, than single-welled potentials.

4.2.3 Spectroscopic data

Bound-bound rovibrational and rovibronic transitions were calculated for all five electronic states. Absorption line oscillator strengths versus photon energy are given for rovibronic transitions in figures 4.8 and 4.9. These transitions include quasi-bound states as initial as well as final states. The oscillator strengths are colour-coded for the rotational P-,Q-,R-branches. $\Sigma \leftarrow \Sigma$ transition have no Q-branch due to selection rules. The energy ranges as well as the form of distributions is different for each pair of electronic states. It is this very specific mixture of lines which make metal hydrides interesting for

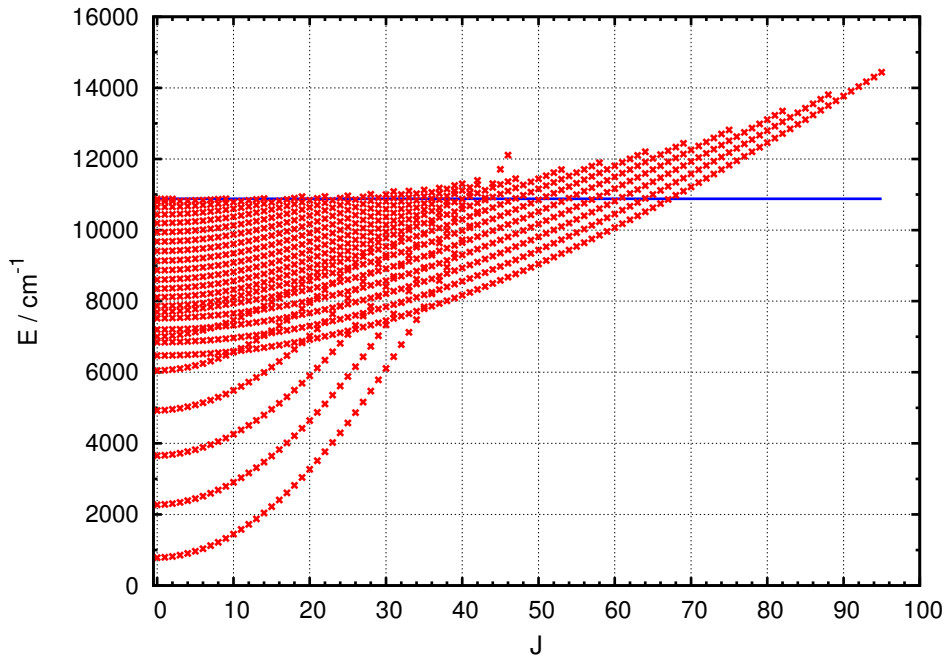


Figure 4.7: Energies of the (quasi-) bound rovibrational eigenstates of $E^2\Sigma^+$ relative to the potential minimum over the rotational quantum numbers. The dissociation energy is the horizontal line.

the computational astrophysics. These spectral lines can be easily identified opening a window into physical and chemical properties of an interstellar environment. Most of the transitions have an oscillator strength in the order of $10^{-2} - 10^{-1}$. The $B'^2\Sigma^+ \leftarrow A^2\Pi$ and $C^2\Pi \leftarrow A^2\Pi$ transitions show only weak oscillator strengths in the order of 10^{-4} and 10^{-3} . The largest single line oscillator strength can be found for $C^2\Pi \leftarrow X^2\Sigma^+$ and $C^2\Pi \leftarrow E^2\Sigma^+$. The $(v'' = 11, J'' = 0) \rightarrow (v' = 7, J' = 1)$ transition of $C^2\Pi \leftarrow X^2\Sigma^+$ has an oscillator strength of 0.85, followed by $(10, 0) \rightarrow (5, 1)$ with 0.53. Several other strong transitions from vibrational highly excited $X^2\Sigma^+$ levels can be found. As the transitions have an energy of about $34500 \text{ cm}^{-1} = 4.28 \text{ eV} = 290 \text{ nm}$, they need environments with reasonable amounts of ultraviolet radiation to play an important role. These lines can not be measured with earth-based telescopes, as this part of the ultraviolet spectrum is blocked by earth's ozone layer. The same is true for the $C^2\Pi \leftarrow E^2\Sigma^+$ transitions. Although the strong low-vibrational transitions have energies of only around 6500 cm^{-1} , it is unlikely that the initial states are highly populated.

The newly added $C^2\Pi$ and $E^2\Sigma^+$ states are more important as final than initial states. For example the $E^2\Sigma^+ \leftarrow A^2\Pi$ transitions have oscillator strengths of the same strength as the bulk of the most important $A^2\Pi \leftarrow X^2\Sigma^+$ transition. The photon energy range between 15000 cm^{-1} and 16000 cm^{-1} ($625 - 670 \text{ nm}$) is within the range where excitations are likely for many systems.

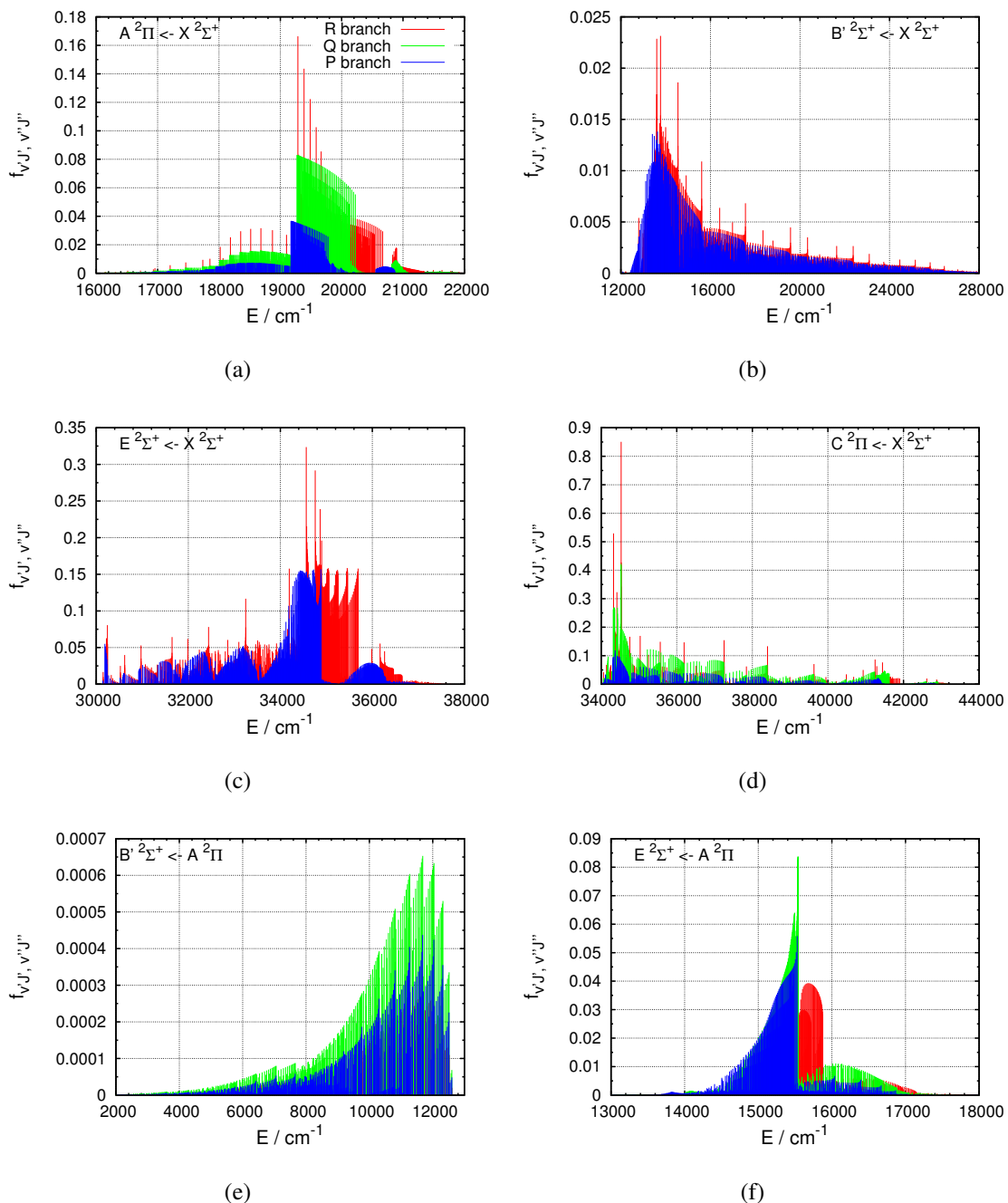


Figure 4.8: Absorption line oscillator strengths f_{ij} over the photon energy. The rotational branches are colour-coded.

Another look has to be given to the quasi-bound states. These add a considerable amount of transitions. For the most cases these are enclosed in the bulk of a transition band and are therefore not too critical. The $A^2\Pi \leftarrow X^2\Sigma^+$ transitions are special here. The bulk oscillator strengths for all three branches between 19000 cm^{-1} and 21000 cm^{-1} are relatively constant over the rotational levels. The quasi-bound states are seamlessly expanding these bands to higher energies. This might significantly change the absorption pattern of

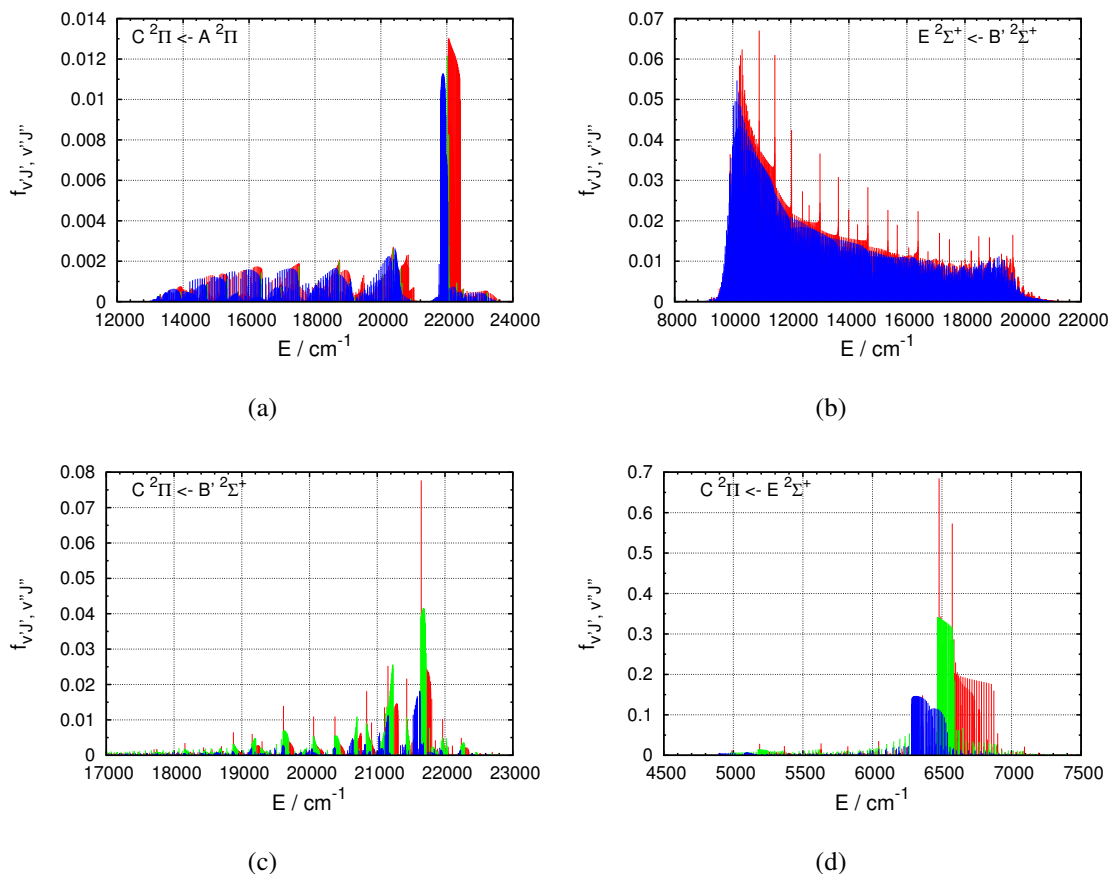


Figure 4.9: Absorption line oscillator strengths f_{ij} over the photon energy. The rotational branches are colour-coded.

MgH, provided these states are physical. Therefore all transitions in the line lists have indicators, whether the initial or final states were quasi-bound or not.

As mentioned in the introduction, Skory *et al.*[63] and Weck *et al.*[64] calculated line oscillator strengths for the $B'^2\Sigma^+ \leftarrow X^2\Sigma^+$ and $A^2\Pi \leftarrow X^2\Sigma^+$ transitions in 2003. As there is no experimental data available for line oscillator strengths, a validation of the calculations is naturally performed by the comparison with other calculations. Skory and Weck used potentials based on the *ab initio* calculations of Saxon *et al.*[65] from 1978 and further adapted it to the experimental data from Balfour *et al.*[60–62].

Figure 4.10 shows a comparison between the $B'^2\Sigma^+ \leftarrow X^2\Sigma^+$ transition from Skory *et al.* and this work. All quasi-bound contributions were removed from my data as Skory *et al.* did not include them. The data sets are almost identical. There is a small shift in the line positions, which is mainly caused by the different ground state excitation energies T_e in both works. The $A^2\Pi \leftarrow X^2\Sigma^+$ oscillator strengths, which are compared in figure 4.11, show some differences. The line positions are overall similar, but the line strength are a factor of 2 larger in this work. This is correct, because the Hönl-London factors from

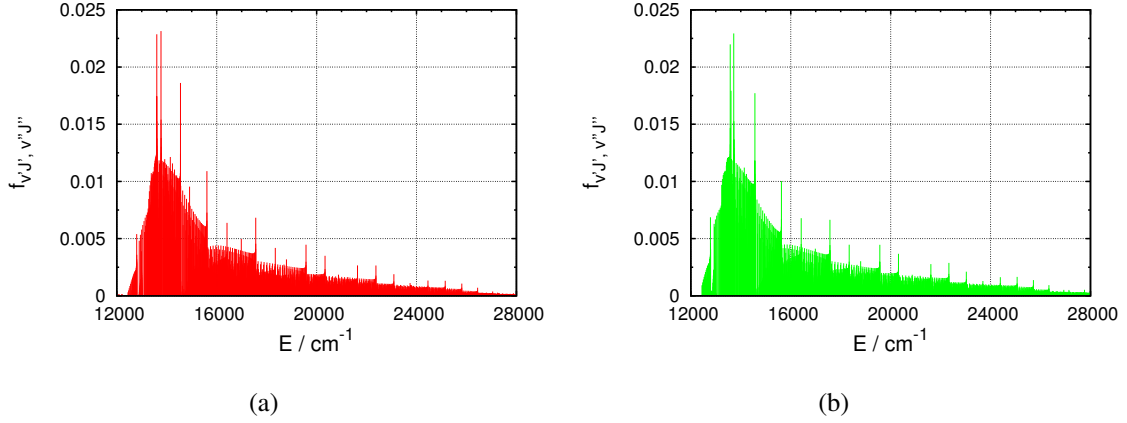


Figure 4.10: Absorption line oscillator strength for bound-bound $B'^2\Sigma^+ \leftarrow X^2\Sigma^+$ transitions are shown in (a). The same plot with data Skory *et al.*[63] is shown in (b) for comparison. No quasi-bound states are included.

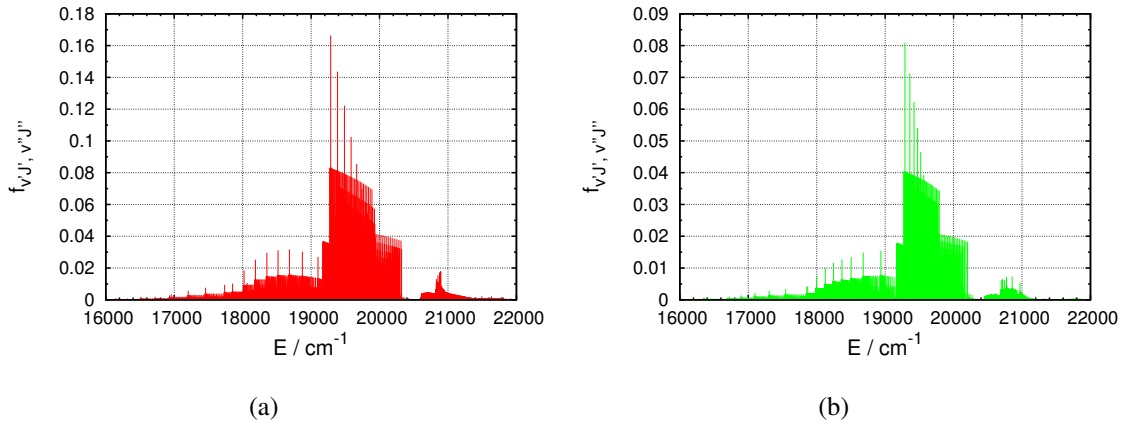


Figure 4.11: Absorption line oscillator strength for bound-bound $A^2\Pi \leftarrow X^2\Sigma^+$ transitions (a) and data from Weck *et al.*[64] (b) for comparison. No quasi-bound states are included.

Hansson and Watson[59] are a factor of 2 larger than the ones used by Weck *et al.*[64]. The overall agreement between this and previous works is excellent which validates this work. I used corrected Hönl-London factors and fitted to updated experimental data, which improves the quality of the data for the lowest three electronic states. In addition two additional electronic states are included, which expand the energy range for which spectroscopic data is available into the near-ultraviolet region.

The line lists from this work can be used as input for the radiation transport calculations in stellar modelling. Peter Hauschildt used this new data to calculate a test spectrum with

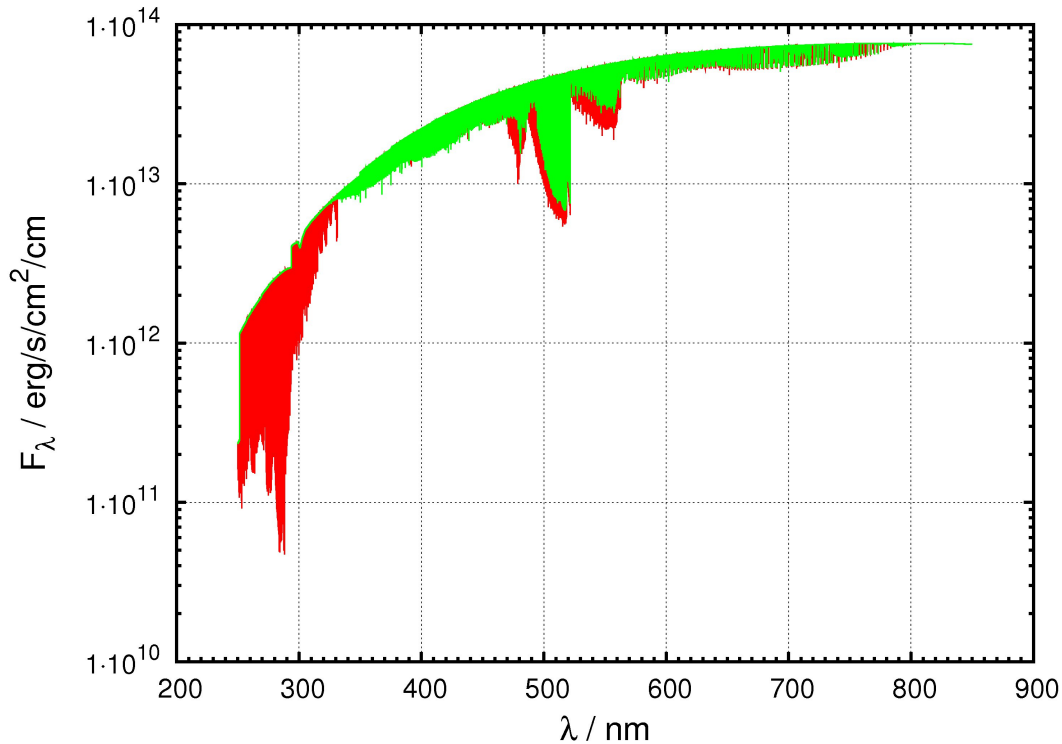


Figure 4.12: Synthetic spectrum with MgH absorption lines only at $T_{eff} = 3500$ K and $\log(g) = 5.0$. Line lists from this work (red) and Weck *et al.* (green) are compared.

the PHOENIX² code with MgH lines only. Figure 4.12 shows the radiative flux F_λ over the wave length for $T_{eff} = 3500$ K and $\log(g) = 5.0$. The figure contains spectra calculated from the current line list and from the data of Weck *et al.*. The absorption between 470 nm and 565 nm is dominated by the $A^2\Pi \leftarrow X^2\Sigma^+$ transitions. Three strong areas can be directly identified with the line oscillator strengths in figure 4.8(a). A comparison with the spectrum obtained from Weck's line lists shows two relevant differences for this part of the spectrum. First of all, the absorption intensity is increased for the new line list. This is caused by the corrected Hönl-London factor in this work. In addition, the absorption bands are extended to lower wave lengths. This is a sign, that the quasi-bound states, included in this work, contribute to the overall opacity. These two improvements to the line lists of MgH are significant. The opacity of an atmosphere hinders the radiation transport. On earth this is known as the greenhouse effect. In a star it changes the temperature gradients. A higher opacity in the synthetic spectrum will cause changes in the predicted temperature and pressure gradients in a stellar atmosphere. The line lists of Weck *et al.* start at approximately 330 nm. For higher photon energies absorption lines are

²PHOENIX is a general-purpose state-of-the-art stellar and planetary atmosphere code. It can calculate atmospheres and spectra of stars all across the HR-diagram including main sequence stars, giants, white dwarfs, stars with winds, T-Tauri stars, novae, supernovae, brown dwarfs and extrasolar giant planets. See <http://www.hs.uni-hamburg.de/EN/For/ThA/phoenix/index.html>

completely missing. This is a major difference to this work. The new line lists contribute to the whole spectrum of the PHOENIX calculation. The major absorption bands between 250nm and 290nm are dominated by the $E^2\Sigma^+ \leftarrow X^2\Sigma^+$ and $C^2\Pi \leftarrow X^2\Sigma^+$ transitions. The main contribution comes from $E^2\Sigma^+ \leftarrow X^2\Sigma^+$. Only the strong absorption lines at 290nm come from $C^2\Pi \leftarrow X^2\Sigma^+$.

4.2.4 Photodissociation

The photodissociation cross sections of MgH are generally weak. They are of the order of 10^{-18} cm^2 , except for resonances which are much stronger ($\sim 10^{-13} \text{ cm}^2$). A compilation of figures with cross sections can be found in the appendix. This section is focused on the general physical discussions and the comparison with results from Weck *et al.*.

Figure 4.13 shows photodissociation cross sections for the $A^2\Pi \leftarrow X^2\Sigma^+$ transition with $J'' = 0$. One can see, that for each v'' the curves end at a different wave length. These wave lengths correspond to the minimum transition energy needed to reach the continuum from a given initial state. The cross sections have no maximum energy within this theory, but in practise photon energies are limited. Another general feature of photodissociation cross sections are the modulations. They are produced by the changing phase and periodicity of the continuum wave functions. The exact form and frequency is unique. As one can see in figure 4.13, the cross sections are relatively constant for wave lengths smaller than $\approx 330 \text{ nm}$, but are increasing strongly for larger wave lengths. A comparison with the corresponding data from Weck *et al.*[66] in figure 4.13(b) shows qualitative agreement in slope, pattern and magnitude. There are, however, differences in the periodicity of the modulations. This is caused by different potentials and transition dipole moments,

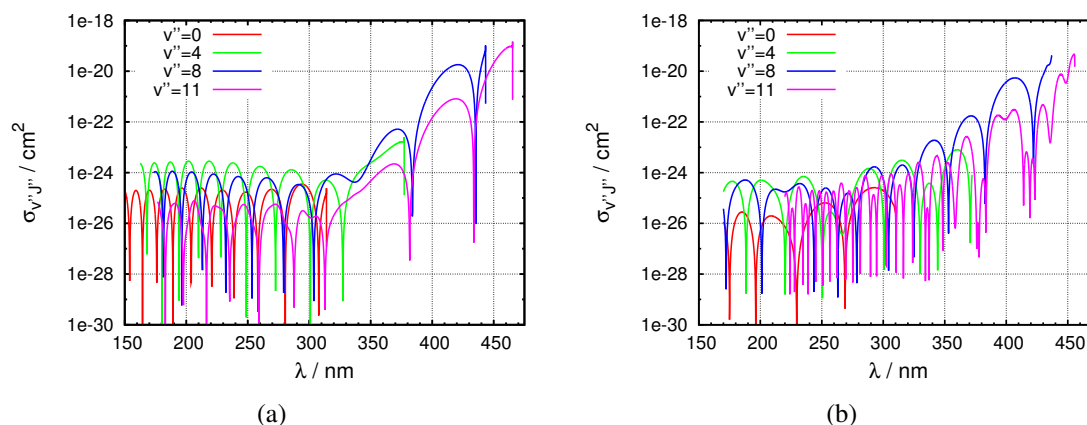


Figure 4.13: Photodissociation cross sections of $A^2\Pi \leftarrow X^2\Sigma^+$ for $v'' = 0, 4, 8$ and 11 with rotation free initial state ($J'' = 0$). Comparison between this work (a) and Weck *et al.*[66] (b) is shown.

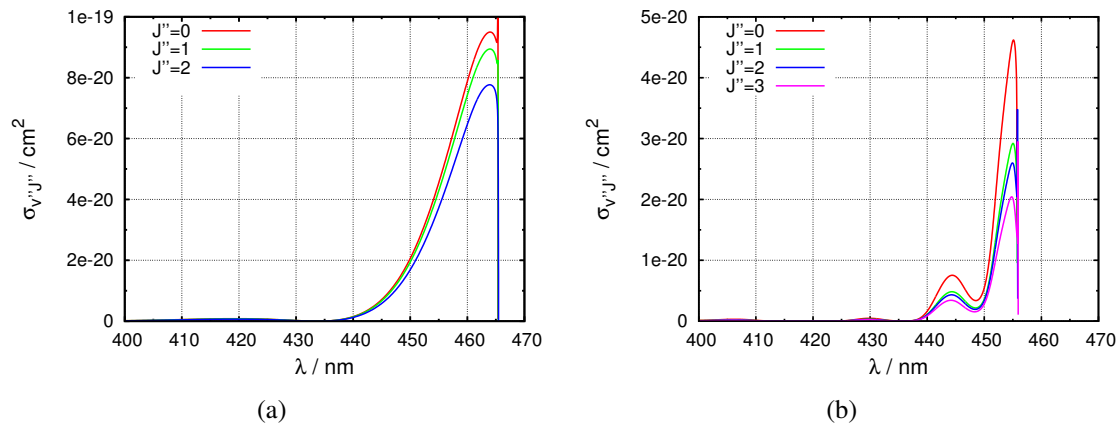


Figure 4.14: Photodissociation cross sections of $A^2\Pi \leftarrow X^2\Sigma^+$ for $J'' = 0, 1, 2$ and 3 with $v'' = 11$. Comparison between this work (a) and Weck *et al.*[66] (b) is shown.

which were used. There is no expectation of the deviation derivable from the known differences between the potentials. Another comparison for the $A^2\Pi \leftarrow X^2\Sigma^+$ transition is given in figure 4.14. Here, the initial vibrational level is kept at maximum, $v'' = 11$. The differences between the potentials can be seen clearly. The cut-off wave lengths differ by 10nm and the form of the curves is rather different. Both works show a clear peak near the cut-off wave lengths. The maxima for $J'' = 0$ differ by a factor of two, which is identifiable with the different Hönl-London factors. The data of Weck *et al.* shows two visible peaks in this scale, one around 444 nm and one around 455 nm. This work shows only one peak, which is broadened at the left flank, as if it includes both of Weck's peaks. Another difference is the much less pronounced rotational dependence in this work, which seems more realistic, as the differences between wave functions of low J 's are only small. In fact the strong decrease of the cross section for $J'' = 0$ to $J'' = 1$ in Weck's data is not consistent with the significantly smaller decreases between the other J 's.

Another comparison can be done for the $B'^2\Sigma^+ \leftarrow X^2\Sigma^+$ transition. The $J'' = 0$ transitions, as shown in figure 4.15, are more regular than for the $A^2\Pi \leftarrow X^2\Sigma^+$ transition. The largest peaks are not located at the cut-off energy, but around 385 nm. This is caused by the different positioning of the $B'^2\Sigma^+$ potential and the more complicated transition dipole moment. Both works agree in the periodicity of the nodes, but the amplitudes, depending on the energy, do not match. The $v'' = 0$ transitions in figure 4.16 show a feature, which has not been that obvious before. Directly before the cut-off wave length resonances occur which can be several orders of magnitude stronger than the surrounding.

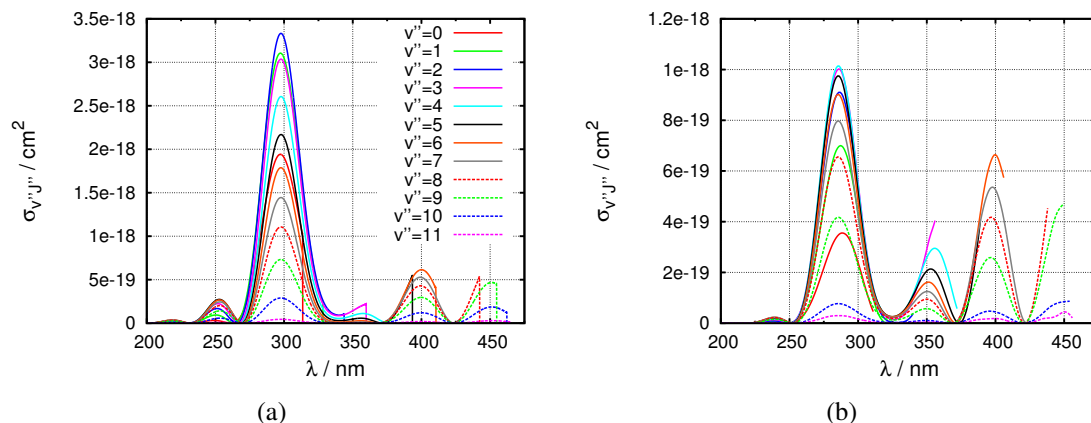


Figure 4.15: Photodissociation cross sections of $B'2\Sigma^+ \leftarrow X2\Sigma^+$ for $v'' = 0, \dots, 11$ with rotation free initial state ($J'' = 0$). Comparison between this work (a) and Weck *et al.*[67] (b) is shown.

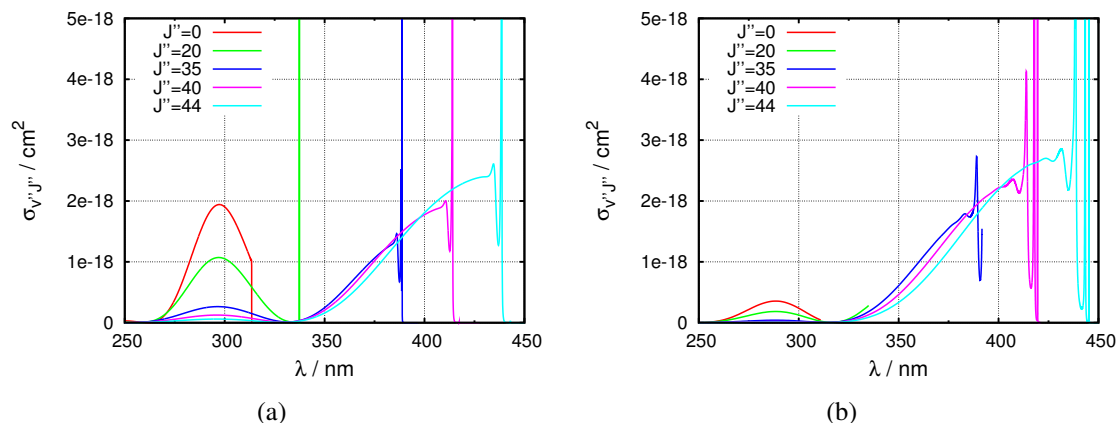


Figure 4.16: Photodissociation cross sections of $B'2\Sigma^+ \leftarrow X2\Sigma^+$ for $J'' = 0, 20, 35, 40$ and 44 with vibration free initial state ($v'' = 0$). Comparison between this work (a) and Weck *et al.*[67] (b) is shown.

4.3 Recap

In this chapter the spectroscopic properties of MgH were studied. Magnesium hydride is an important indicator species for stellar atmospheres. Complete spectra are important for the modelling of stellar atmospheres and the interpretation of measured spectra. Furthermore, destruction and formation processes of molecules must be included in atmospheric models.

The electronic potential and dipole moments of the five lowest doublet electronic states were calculated from *ab initio* methods. This work is an improvement compared with existing numerical studies, as the potentials represent newer experimental data and quasi-

bound states are included. Two further electronic states are taken into account, which expand the range of the line lists into the near ultraviolet spectral range. This adds a significant amount of opacity for stellar radiation transport modelling. A second application is the calculation of photodissociation cross sections. The photodissociation cross sections of MgH reveal a stronger dependence of the underlying potential than the bound-bound lines.

The rovibronic line lists calculated in this chapter complete the spectroscopy oriented studies of this thesis. The second branch is reaction dynamics. A first example was the calculation of photodissociation cross sections from the wave functions obtained for the rovibronic transitions. In the next chapter a binary reaction of the type $A + B \rightarrow C + D$ will be surveyed.

5 Reactive studies of the Methylidyne cation

The previous chapters focused spectroscopic applications of *ab initio*-based potential energy surfaces. But, as explained in chapter three, these potentials can also be applied for reaction dynamics. This second branch of the thesis is covered in this chapter with the example of the CH_2^+ reactive system.

The methylidyne cation, CH^+ , is a common molecular ion in interstellar environments and comets[68]. Although it was the first cation ever identified in interstellar space[69], its dynamics of formation and destruction are not yet completely understood. The measured abundances of CH^+ are often several orders of magnitude larger than predictions from standard gas-phase models (see Godard *et al.*[70] and references therein). This implies, that either the models or the reaction rate coefficients are incorrect. Therefore, one has to find mechanisms which either prevent destruction reactions or lead to an additional formation of the methylidyne cation, especially at low temperatures.

CH^+ can be easily destroyed by H, H_2 and electrons[71]. This work focuses on the collision with a neutral hydrogen atom



which is a reaction intuitively expected to be important, because of the high abundances of neutral hydrogen atoms in the interstellar space. This reaction is exothermic and has no known activation barrier.

Stoecklin and Halvick[72] published a potential energy surface for this reaction which was based on single electronic state *ab initio* calculations and a sixth-order polynomial fit for the three-body potential, including an *ad-hoc* term for the conical intersections. This potential was used by Halvick *et al.*[73] for quasi classical trajectory (QCT) and phase space theory (PST) analysis of the $\text{H} + \text{CH}^+$ reaction. The C^+ abstraction cross sections are predicted to be monotonically decreasing between 1K and 1000K. New measurements of Plasil and Gerlich[74–76] show a maximum of the rate coefficient at

60K and a strong gradient of the thermal rate for lower temperatures, which diverges from theoretical results[72, 73].

This discrepancy of experiment and theory and the unexplained abundance of CH^+ in interstellar environments motivate further research. The aim of this work is to improve the numerical predictions for the reaction rate coefficients. For this an *ab initio*-based potential energy surface was developed which was tested and used for QCT and reactive quantum scattering calculations.

In this chapter the chemical and physical properties of the CH_2^+ molecular system are presented. The potential energy surface is characterised and reaction cross sections and rate coefficients are given[77].

5.1 Properties of the CH_2^+ reactive system

The methylidyne cation, CH^+ , can be created by several gas-phase processes, which include reactions of carbon cations for neutral H or H_2 . A detailed discussion of creation and destruction processes can be found in Plasil *et al.*[74].

The binding energy of CH^+ is 4.255 eV, which is approximately 0.5 eV less than H_2 . The permanent dipole moment is 0.658 au along the symmetry axis C-H. Figure 5.1 compares the electron densities of CH and CH^+ at $r_e(\text{CH}^+) = 2.137 a_0$ obtained from a MC-SCF analysis of ground states. The electron densities are largest around the carbon nucleus. In the case of CH the electron density is decreasing continuously outside. The slope of the electron density between the nuclei is approximately symmetric. The Mulliken charges

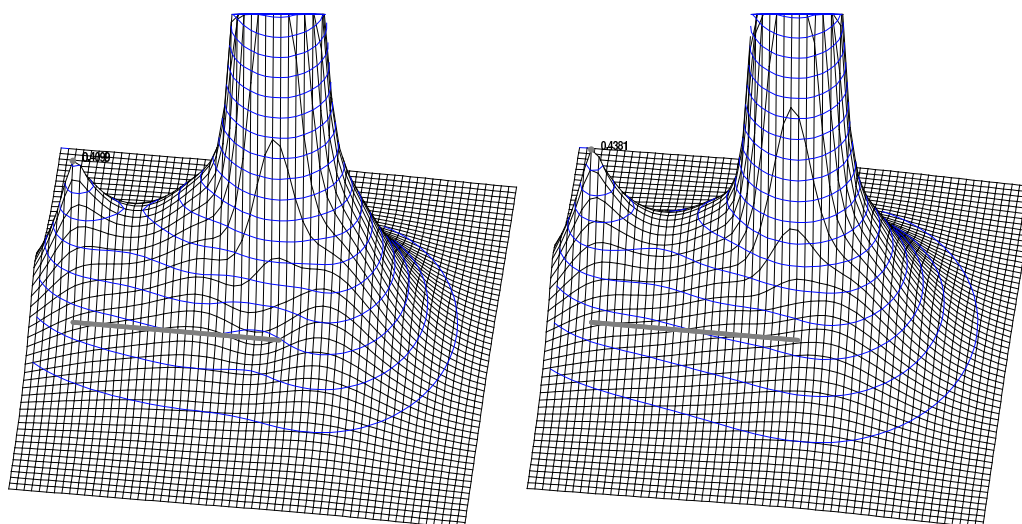


Figure 5.1: Electron density for $\text{CH}^+ X^1\Sigma^+$ (left) and $\text{CH} X^2\Pi$ (right) along the yz plane. The molecule is shown as a grey stick with the H atom on the left end. Contour lines have an increment of 0.05.

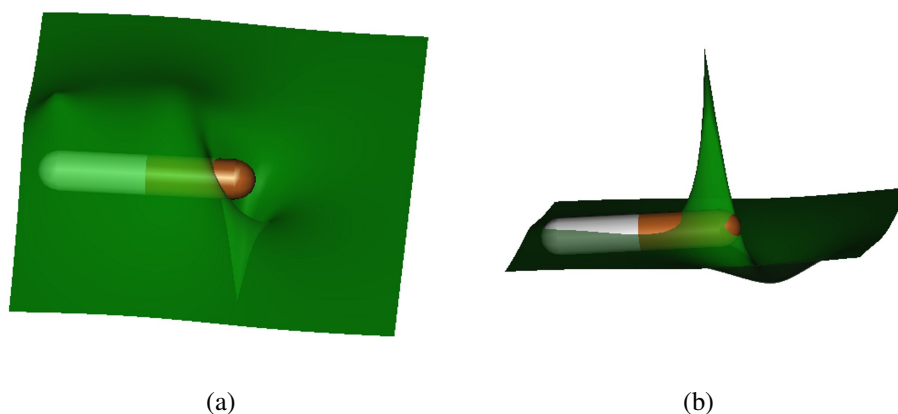


Figure 5.2: Molecular orbital function of the second (a) and third (b) σ orbitals of the ground state of CH^+ . The C atom is encoded in orange, the H atom in white. Only yz-plane cut is shown.

for C and H are -0.26 and 0.26 respectively. This reflects a slight polarisation of the covalent bond towards the carbon, as expected from the slightly larger electronegativity of carbon, 2.55 versus 2.20 of hydrogen. CH^+ has one electron less, which causes a decrease in the off-axis electron density near the carbon. The density between the nuclei is increased on the carbon side, reflecting a stronger charge transfer from the hydrogen. This is also reflected in the increased hydrogen Mulliken charge of 0.49. The six electrons are distributed primarily over three σ molecular orbitals. The lowest one is the doubly occupied $1s$ atomic orbital of carbon. As this orbital always keeps its atomic character, it is usually not included into the optimisation during configuration interaction calculations. A MC-SCF analysis gives an occupation number of 1.96 ($0.78 \text{ H } 1s + 0.52 \text{ C } 2s$) for the second σ orbital. The corresponding molecular orbital function is shown in figure 5.2(a). The second σ orbital shows three peaks along the axis of symmetry. One at each nucleus and one in between, but nearer to the carbon. As this orbital already shows a strong mixing of different atomic contributions, all but the innermost s -shell of carbon have to be optimised. The third σ orbital is more localised around the carbon. It reflects a part of the bond and the valence electron behaviour. The occupation number is 1.88 ($-0.93 \text{ C } 1s + 0.59 \text{ C } 2p_z + 0.17 \text{ H } 1s$).

The ground state of CH_2^+ is $X^2\Sigma^+$. This C_{2v} state has an equilibrium distance of $2.088 a_0$ with a H-C-H bending angle of 139.8° . For comparison, water has $1.81 a_0$ and 104.48° . For the $\text{H} + \text{CH}^+$ reaction, for which a correlation diagram is given in figure 5.3, one finds in the ground electronic state a peculiarity for the two linear configurations. In this $C_{\infty v}$ symmetry the $X^1\Sigma^+$ CH^+ has no open pair for an additional hydrogen atom to couple with, as discussed earlier. This causes a repulsive potential. In the $a^3\Pi$ configuration the C $2p$ electron stays in a π orbital. Therefore, an attractive potential for an incoming

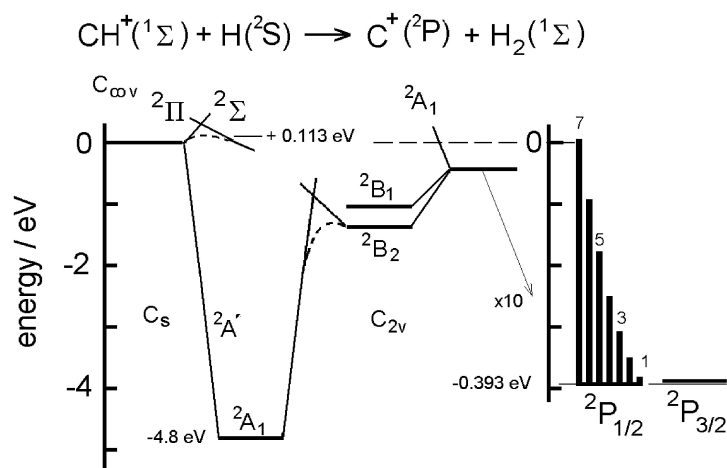


Figure 5.3: Selected features of the potential energy surfaces of the $\text{H} + \text{CH}^+$ reaction. For a complete correlation diagram, see Ervin and Armentrout[78]. In C_s symmetry the strongly bound CH_2^+ intermediate can be reached directly on a purely attractive surface. Collinear approach of the reactants ($^2\Sigma$ and $^2\Pi$ state) leads to an energy barrier, due to a conical intersection. According to Halvick *et al.* the crossing seam is 0.113 eV high. The right part presents some information for C_{2v} symmetry, indicating, that there are no energy barriers for reaching the product. The exothermicity of the reaction, 0.393 eV, is sufficient to populate rotational states of H_2 up to 6. The $J = 7$ state is endothermic. This figure is taken from Plasil *et al.*.

H atom is formed. This combination causes conical intersections between H and C to appear. Assuming a pure adiabatic behaviour, a reaction stays on the lowest energy potential. If the molecule is slightly bend out of the linear configuration, the Σ and Π states become A' and $A' + A''$ states in C_s symmetry. Two curves of the same irreducible configuration can not cross. Therefore, the intersections transform into avoided crossings in bend configurations.

The H_2 product lies 0.393 eV lower than CH^+ , populating H_2 rotational levels up to $J=6$. As CH^+ has a smaller spacing between rotational levels, the thermal population favours H_2 for low temperatures and CH^+ for higher temperatures.

5.2 Methods

5.2.1 Choice of *ab initio* method

Depending on the electronic structure, appropriate methods for *ab initio* calculations have to be chosen. As described in the previous section, the system at hand shows a strong mixing of states or electronic configurations. The conical intersections are one reason.

The other one is the span of the configuration space, which has to be covered. There are three major configurations of the system: The CH_2^+ complex, the $\text{H} + \text{CH}^+$ channels and the $\text{C}^+ + \text{H}_2$ channel. All these have a different electronic structure. A multi-reference method, here multi-reference configuration interaction (MRCI)[13–15], has to be employed, because in the intermediate regions of the configuration space the electronic structure is often difficult to converge. As MRCI results depend on the symmetry used for the computation, C_s symmetry was used for all configurations. In order to correctly represent the region in the configuration space governed by the conical intersections and avoided crossings both intersecting/ avoided crossing electronic states have to be calculated simultaneously in these regions. These are two A' states and one A'' state in C_s symmetry. Only the two A' states have to be calculated as including the A'' in the optimisation process does not improve the A' state energies. Far outside the crossing regions only the lowest electronic state is of interest. Yet, both A' states are computed over the whole configuration space to avoid discontinuities in the regions where energies are computed in two different ways, meaning that one or two states of the same irreducible representation included in the optimisation process. This can happen as the starting orbitals from the MCSCF calculation (see below) are different for these cases.

The choice of active space and basis sets is a compromise between accuracy and speed. In this case, the aim was a convergence threshold respective to basis sets and active space of less than the typical error of the fitting procedure. This can be estimated to be several 10^{-4} atomic units (Hartree), which corresponds to about 10 meV. The augmented correlation-consistent valence triple zeta (aug-cc-pVTZ) basis sets of Dunning[6, 55] were chosen. A larger basis like aug-cc-pVQZ would have been too expensive. The non-augmented cc-pVQZ basis has a size between aug-cc-pVTZ and aug-cc-pVQZ. The augmented versions of Dunning's basis sets have additional diffusive terms[55]. These terms can be important in the pre-dissociation phase and for non-localised or weakly bound electrons. The cc-pVQZ basis was ruled out, because it lacks these diffusive terms.

For each configuration, first complete active space self-consistent field[11, 12] (CASSCF) orbitals and electron densities are calculated. As the lowest two A' states are included in the calculation, these orbitals and densities are state averaged (SA-MCSCF) with equal weights for each state. The innermost s -shell of C is considered closed, leaving 5 electrons to be distributed over 10 active molecular orbitals ($8 A'$, $2 A''$). In the following, Davidson-corrected internally-contracted multi-reference configuration interaction[13–15] (MRCI) was used, where both states were optimized simultaneously with the C $1s$ electrons treated as core. Core electrons are not further optimised and no excitations from core orbitals are included. As the C $1s$ orbital keeps its atomic character also in molecular bonds, MRCI energies show only small changes. All *ab initio* calculations were performed using MOL-PRO2009.1[35].

5.2.2 Potential energy surface

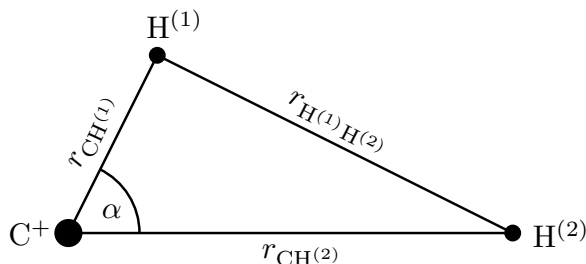


Figure 5.4: Coordinates used to describe the CH_2^+ molecular system.

The standard form of the PES (see section 2.2) is well-suited for single-valued global potentials without cusps. In order to account for conical intersections this approach has to be modified. One needs a representation for the conical intersection, which smoothly transforms into an avoided crossing form at near-linear configurations. It is reasonable to stay with the well-tested potential fit and to add another set of polynomials for each intersection. These should be non-zero only in the vicinity of the corresponding intersection. Using this approach one has the full flexibility to choose appropriate functions/functionals for the intersections, while keeping all advantages of the well-known PES, including the simultaneous least-squares fit of all coefficients. In the case of a x_2y_1 -type system the internuclear distances are $r_{x^{(1)}x^{(2)}}$, $r_{x^{(1)}y}$, $r_{x^{(2)}y}$, as shown in figure 5.4 for CH_2^+ , and the invariant basis is $r_{x^{(1)}x^{(2)}}$, $\overline{r_{x^{(i)}y}}$ and $r_{x^{(i)}y}^2$.

This work uses the standard variable transformation $y = e^{-r/\lambda}$ for the xy -distances, the xx -distance is transformed as

$$y = e^{-|r-r_0|/b}, \quad (5.2)$$

where r_0 is the position of the conical intersection, which might depend on the other coordinates as well. First or second degree polynomials should be used with these coordinates, otherwise a poorly chosen r_0 might produce erratic behaviour of the fit close to r_0 . In addition to the modified polynomial a modified damping function was introduced:

$$t_0 = e^{-k \cdot \min(\alpha, \pi - \alpha)} \max \left(e^{-l|r_{x^{(1)}y} - a|}, e^{-l|r_{x^{(2)}y} - a|} \right). \quad (5.3)$$

α is the angle x - y - x , which can be easily calculated from the internuclear distances. The chosen form of the potential near the intersection is very sensitive to the parametrisation, but it offers a representation of intersections with an accuracy similar to the accuracy of the potential fit.

The overall computational cost of the added polynomials is insignificant compared to the original PES, which can use up to 19th order polynomials for triatomic systems.

5.2.3 Dynamics

The quasi classical trajectory method (QCT) was applied for the calculation of cross sections and rate coefficients. In QCT the atoms of the molecular system are moved following Newton's equations of motion. The force is usually given by an analytical or fitted potential calculated with quantum mechanical methods. The initial conditions for rotational and vibrational energies are quantised. Quantities like impact parameters and phases are varied using Monte-Carlo sampling for a large number of trajectories. This allows to calculate statistical properties of the reactive system, like reaction cross sections. As the particles are moved by Newton's equations of motion in QCT, no quantisation of vibration or rotation is preserved over the trajectories. Especially in the case of low kinetic and internal energy, where the vibrational zero-point energy is a large fraction of the total energy, quantum-mechanically forbidden results dominate, which leads to incorrect cross sections.

In this work a QCT code was developed using fifth-order Gear[79] predictor-corrector integration and adaptive time-step management. A velocity verlet integrator is also implemented and can be selected by the user. The Gear integrator itself consumes more operations per cycle than the simpler velocity verlet algorithm, yet it is more stable for long simulation times and allows larger time steps. Automatic time-stepping was implemented using the energy conservation between time steps as a measure and a three-limit system. If the error is smaller than the lower limit $ll1 = 0.000075$ meV, the time step for the next cycle is increased by 5%. If the error is larger than the threshold $ul1 = 0.00075$ meV the time step is decreased by 10%. These two thresholds were chosen such that the total energy conservation over a run is not significantly improved by tightening these limits. If the energy conservation is worse than the $ul2 = 0.001$ meV threshold the whole time step is recalculated with a halved time step. Additionally, absolute minimal and maximal time steps of $dt_{min} = 0.0001$ fs and $dt_{max} = 0.1$ fs as well as a repetition counter were introduced, to avoid infinite loops and unreasonable low or high time steps. The total error for the energy conservation depends on the initial conditions but was limited to few meV or less. The parameters must be checked and eventually changed if other systems or potentials are used. The calculation of initial conditions was implemented using the semi-classical Einstein-Brillouin-Keller quantisation of the action integral.

In the standard weighting each quasi classical trajectory has a weight of unity and product quantum numbers for final state resolved cross sections are given by the nearest integer to the semi-classical ones. The standard weighting is therefore often referred to histogram binning (HB). The cross sections are defined as

$$\sigma_{\alpha}^{HB} = \pi b_{\alpha}^2 \frac{N_{\alpha}}{N}, \quad (5.4)$$

where N is the total number of trajectories with impact parameter $b \leq b_\alpha$, the largest impact parameter leading to channel α . The channels are inelastic collision, hydrogen exchange and carbon abstraction. As mentioned above the histogram binning is known to yield non-physical results for many systems due to zero point energy violation, population of energetically closed final states and wrong final state distributions[80]. Therefore, alternative post processing techniques were developed.

Bonnet[80–83] suggested a modified treatment for inelastic collision calculations, where the product state rotational distributions have to be corrected in the standard QCT. Starting from the classical S matrix theory (CSMT), see e.g. the work of Miller and Marcus[84–86], the product side state distribution is expressed in terms of Dirac distributions. Cross sections deduced at this point are exact in the context of CSMT, if the contribution from the interference term of the semi-classical probability is negligible (see Bonnet[80] equations 4 and 6). The set of trajectories with integer semi-classical quantum number is usually of zero measure with respect to the set of all trajectories. In order to compensate that the Dirac distribution is substituted by a Gaussian distribution, whose widths have to be small to mimic the Dirac distribution. This treatment is called Gaussian weighting (GW) or Gaussian binning. Although this method is derived for an inelastic collision case, it has been successfully applied for reaction dynamics as well. The Gaussian weight is defined as

$$w_i(\delta v_i) = \frac{1}{\sqrt{2\pi}s} e^{-\frac{(\delta v_i)^2}{2s^2}}, \quad (5.5)$$

where δv_i is the difference between the final vibrational quantum number and its nearest integer value of trajectory i and s^2 is the variance of the Gauss function.

If N and N_α are replaced in equation (5.4) with the corresponding sum over weights (5.5), the Gaussian weighting cross sections are defined as

$$\sigma_\alpha^{GW} = \pi b_\alpha^2 \frac{\sum_i^{N_\alpha} w_{\alpha i}}{\sum_i^N w_i}. \quad (5.6)$$

In practise this definition causes problems with the elastic trajectories. In QCT even trajectories which do not form complexes sometimes do not preserve their integer quantum numbers, as there is still an interaction potential between the reactants. Also numerical errors can add up over the millions of steps of a trajectory. If included into weighting these trajectories would loose most of their weight. If one measures the minimum distance between the reactants over the trajectory one finds a separation of collisional and non-collisional trajectories. This is shown in figure 5.5 for $J = 5$ and $E_{kin} = 100$ meV. In this figure non-elastic trajectories have a minimum distance between the reactants of less than $2a_0$. Elastic cases, however, have a minimum distance of at least $3a_0$. There are also cases, where the complex region is reached and the Gaussian binning of the trajectories

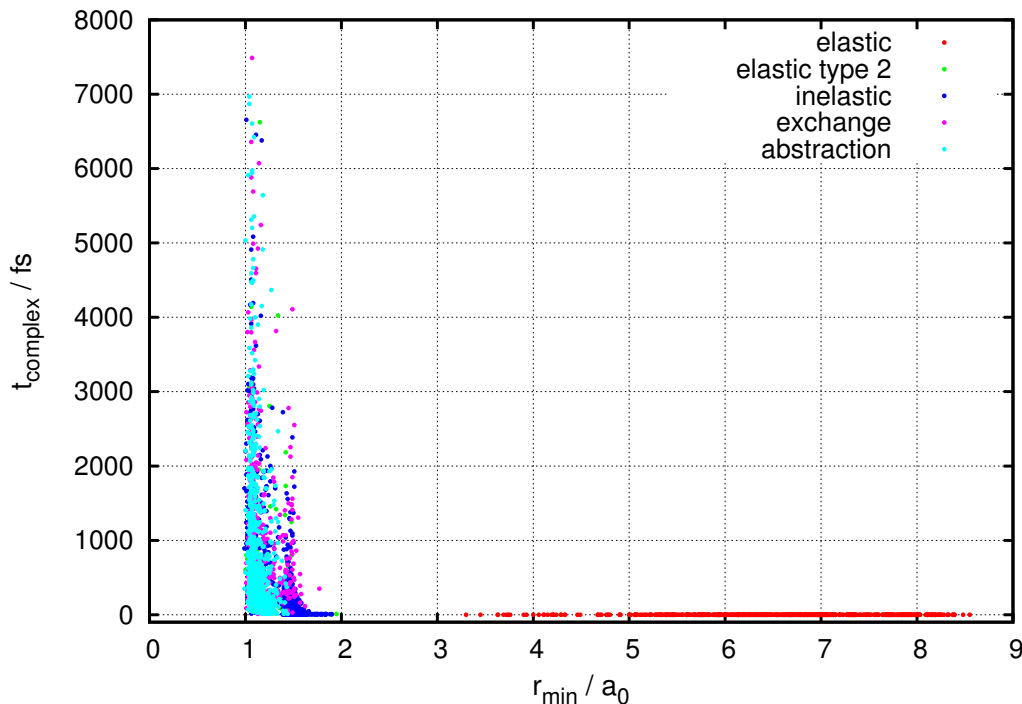


Figure 5.5: The time of trajectories in the complex region versus the minimum distance between the reactants for initial conditions $J = 5$ and $E_{kin} = 100 \text{ meV}$. Elastic collisions are distinguished, whether (type 2) or not they enter the complex region.

identifies them as elastic, these are marked as type 2. This separation distance is getting smaller for larger initial energies, but it does not diminish for the energy ranges used in this work. The distance between the fragments was defined as the second shortest internuclear distance. The shortest one would define the bound diatomic molecule. A rescaling of the internuclear distance to the equilibrium distances of the corresponding diatomics might be used for systems where the simple ansatz is failing. The encounter distance was set to $3a_0$.

Using the knowledge how to identify the complex forming trajectories N_c , these can be separated in the cross section equation. Defining weights $w_\alpha = \sum_i^{N_\alpha} w_i$ and $w_c = \sum_i^{N_c} w_i$ the final equation of the Gaussian is

$$\sigma_\alpha^{GW} = \pi b_\alpha^2 \frac{N_c w_\alpha}{N w_c}. \quad (5.7)$$

The Gaussian weighting does not necessarily provide satisfactory results, if the width of the Gaussian can not be chosen small enough or if the CSMT is failing. As an alternative an empirical modification of the Gaussian weighting (mGW) is introduced, which allows a better fitting of the results. The width of the Gaussian varies for the different channels

and the normalisation is removed. The equation (5.5) reads now

$$w_i(\delta v_i; a) = e^{-\frac{(\delta v_i)^2}{2s_\alpha^2}}. \quad (5.8)$$

Varying the Gauss width s_α over the channels allows active changing of the weights of these channels for the cross sections. This allows a fitting of cross sections to desired values, but it is also a shortcoming of this procedure, as results now strongly depend on parameters, which can not be justified easily.

For this system the largest drawback of HB-QCT is the population of energetically closed product states, which should be taken care of by the Gaussian weighting. Let me approximate the rotational energy of the diatomic product as a rigid rotor with $E_{rot}(j) = Bj(j+1)$ and the vibrational energy as a harmonic oscillator $E_{vib} = \omega(v + \frac{1}{2})$, with rotational constant B , harmonic frequency ω , rotational and vibrational quantum numbers j and v . The difference of the vibrational energy from the integer quantum number value δv should be less than the smallest rotational transition energy: $\omega \delta v < 2B$. As in this case the Gaussian weighting is meant to prevent the population of closed channels, an effective weighting follows $s_\alpha \propto B_\alpha/\omega_\alpha$. An appropriate proportionality factor has to be chosen manually, yet it can not be much larger than unity as the weighting would allow forbidden low energy transitions.

It is also possible to use Gaussian weighting for the final rotational quantum number as well. Tests have shown no significant change in the cross sections for rotational weighting widths s_J in the order of 10^{-1} and a strong gradient in the cross sections depending on s_J , if it is chosen in the order of 10^{-2} , with no sign of convergent behaviour. Therefore, this work is not using rotational weighting.

To obtain an error estimate of equation (5.7) error propagation of independent variables is used. $f(x_i)$ being a function of independent variables x_i and their standard deviations Δx_i , the deviation Δf is given by

$$\Delta f = \sqrt{\sum_i \left(\frac{\partial f}{\partial x_i} \Delta x_i \right)^2}. \quad (5.9)$$

The maximum impact parameter b_α is obtained from trajectory calculations. Assuming that all reaction channels α need a complex formation, the maximal impact parameters of all these channels should be identical. Therefore, the standard deviation of the impact parameter can be calculated directly. The first addend for the error propagation is therefore $\left(\frac{2\Delta b_\alpha}{b_\alpha} \right)^2 \sigma_\alpha^2$. N and N_c are dependent variables as $N = N_c + N_n$, where N_n is the number of non-complex-forming trajectories with $b \leq b_\alpha$. As these variables represent the convergence of a Monte-Carlo process, their error can be estimated by their square

root, e.g. $\Delta N_c = \sqrt{N_c}$. This yields $\frac{N-N_c}{N_c N} \sigma_\alpha^2$ as the second term in the error propagation. This term converges with $1/N$. I have chosen to use two terms for the error estimate of w_α and w_c . As the weights are calculated over finite sums with upper bounds N_α and N_c , respectively. The same scheme is applied for the error estimates of the w as for the error estimates of the N 's. The third term of the error propagation is therefore $\frac{w_c - w_\alpha}{w_\alpha w_c} \sigma_\alpha^2$. Using both terms, for N and w , yields a small overestimation of the error, as N_c and w_c are not independent. This overestimation is negligible for small $\sqrt{1/N_c}$. Another uncertainty lies in the definition of the w_i in equation (5.8). The parameter s_α has no analytically defined value. The sensitivity of the cross sections to the choice of s_α is included by a separate term in the error propagation calculation. Defining normalised weights $\Omega_\alpha = \frac{w_\alpha}{w_c}$ one can use the standard deviation of Ω_α with respect to changes of s_α . This does not necessarily measure the convergence, but rather the slope of the s_α dependency of the cross sections. All these terms result in a variance estimate for σ_α given by

$$s_{\sigma_\alpha} = \sigma_\alpha \sqrt{\left(\frac{2\Delta b_\alpha}{b_\alpha}\right)^2 + \frac{N - N_c}{N_c N} + \frac{w_c - w_\alpha}{w_\alpha w_c} + \left(\frac{\Delta \Omega_\alpha}{\Omega_\alpha}\right)^2}. \quad (5.10)$$

Assuming an equilibrated Boltzmann distributed system at temperature T , the thermal rate coefficients $\kappa_\alpha(T)$ are

$$\kappa_\alpha(T) = \left(\frac{8}{\pi\mu(kT)^3}\right)^{1/2} \int_0^\infty E_{coll} e^{-E_{coll}/kT} \sigma_\alpha(E_{coll}, T) dE_{coll}, \quad (5.11)$$

with temperature averaged cross sections

$$\sigma_\alpha(E_{coll}, T) = \frac{1}{Q_\alpha} \sum_n g_n \sigma_\alpha(E_{coll}, n) e^{-E_n/kT}, \quad (5.12)$$

where $n = \{v, j\}$ represents the internal degrees of freedom and $\sigma_\alpha(E_{coll}, n)$ are the initial-state resolved cross sections depending on the collisional energy E_{coll} . Further quantities are the reduced mass μ , the multiplicity g_n of state n and the canonical partition function Q_α .

As stated in this section, the reliability of the QCT methods is questionable. Therefore, a modified version of the ABC[87] quantum scattering code is used for comparison. This program solves the Schrödinger equation of the atom-diatom chemical reaction with a coupled-channel hyperspherical coordinate method (see section 5.2.4). As the classical S matrix theory, from which the Gaussian weighting is derived, is the semi-classical limit of the quantum scattering, this is an appropriate choice for bench marking. As computational costs grow very fast with the states entering into the scattering matrix, the application of ABC is limited to low energy cases.

5.2.4 ABC: quantum reactive scattering

The ABC[87] code for quantum mechanical reactive scattering for atom-diatom chemical reactions uses a coupled-channel hyperspherical coordinate method[88, 89] to solve the Schrödinger equation for the three nuclei on a single Born-Oppenheimer potential energy surface. Optimal coordinates for one product channel, e.g. mass-scaled Jacobi coordinates, are inappropriate to describe other product channels. In the coupled-channel approach the wave function is always expanded in all three chemical arrangements simultaneously. ABC uses Delves hyperspherical coordinates[90, 91]. The program uses exact quantum reactive scattering boundary conditions, avoiding the usage of imaginary absorbing potentials[92]. As ABC uses Born-Oppenheimer potentials, spin-orbit coupling can not be treated correctly in this code. In each run, the reactive scattering Schrödinger equation is solved for one combination of total angular momentum and parity delivering parity adapted scattering matrices as output. For a more detailed description see Skouteris *et al.*[87] and references therein.

5.3 Results

5.3.1 Potential energy surface

The CH_2^+ potential energy surface for the lowest A' electronic state was built from 16259 *ab initio* points. The standard polynomial was built with 5th order two-body polynomials and 13th order three-body polynomials. The cut-off lengths were chosen to be 12 and 8 a_0 , respectively. The additional polynomials were both chosen to be 2nd order. The 0eV-level is set to the asymptotic $\text{H} + \text{CH}^+$ energy in this chapter work.

The weighted root mean square (rms) error of the PES is 6.3 meV. The rms error for energies smaller than 0.1 au (0.1 au \approx 2.7 eV) above the global minimum is 15.5 meV and for energies between 0.1 and 0.2 au above the global minimum it is 17.2 meV. This means, that in the incoming channel variations due to errors in the fitting with amplitudes in the order of 10 to 20 meV have to be expected. These variations have their origin in

Table 5.1: Important reference values of the PES with experimental values in brackets: Dissociation energies D_e , equilibrium bond distances r_e and angles α_e . CH_2^+ dissociation energy to $\text{CH}^+ + \text{H}$.

	D_e / eV	r_e / a_0	α_e
CH^+	4.195 (4.255)	2.142 (2.137)	—
H_2	4.711 (4.751)	1.412 (1.401)	—
CH_2^+	4.778	2.069 (2.088)	141.2° (139.8°)

the polynomial form of the fitting function. If the kinetic energy is larger than this, the fragments are decelerated, accelerated and possibly deflected, but not reflected. Therefore, the reactive behaviour should not change significantly. If an incoming hydrogen hits a positive hump with a kinetic energy lower than the height of the hump, it is going to be reflected, causing a corruption of the reaction statistics. A symptom for this would be an otherwise unexplained increase of elastic scattering events for collision energies of less than 20 meV. Other important quantities of the PES are given in table 5.1. The equilibria of the complex and the different fragments differ between $0.005 a_0$ and $0.02 a_0$ with the experimental data, the dissociation energies up to 0.06 eV. The exoergicity of 0.518 eV is near the experimental value of 0.496 eV. This is well within the expected limits of the MRCI/aug-cc-pVTZ method and comparable with Stoecklin and Halvick, where bond lengths are underestimated and dissociation energies are overestimated. This work shows opposite behaviour with underestimated dissociation energies and partly overestimated bond lengths. For the complex region this work better fits experiments, but the fragments are slightly better represented by the former work, which is probably caused by the form of the fitting functions.

The validity of the extended fit using additional polynomials to describe the conical in-

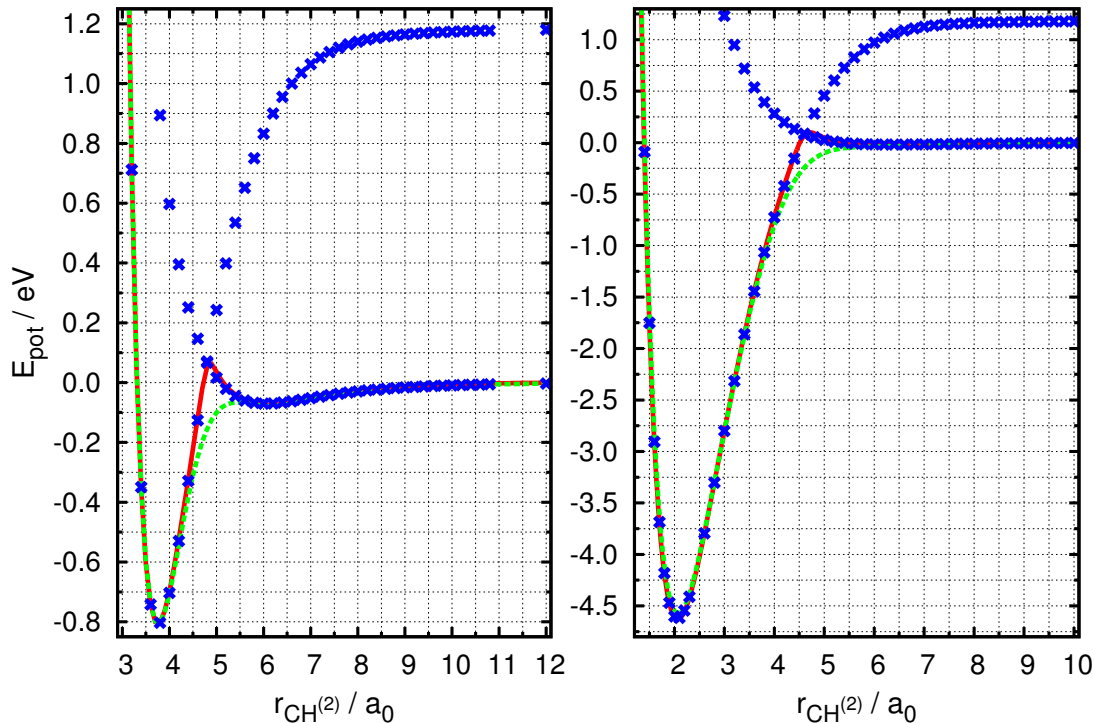
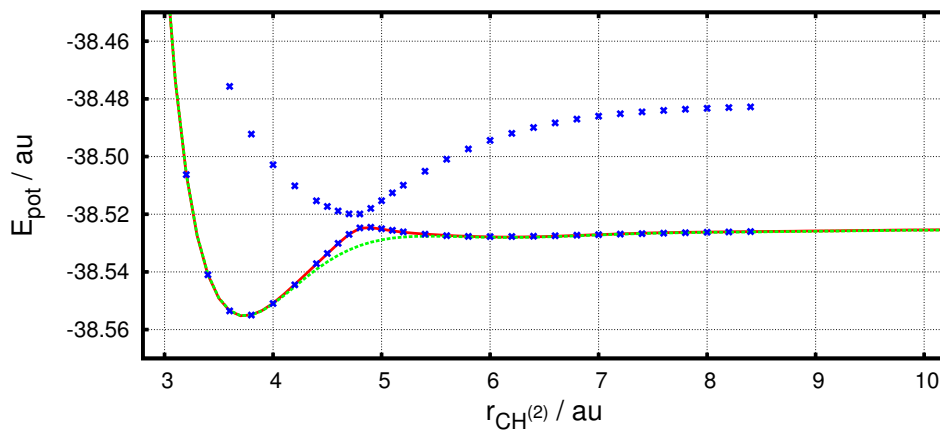


Figure 5.6: One-dimensional PES cut for fixed $r_{\text{CH}(1)} = 2.14 a_0$ at linear C-H-H (left) and H-C-H (right) configuration. Blue crosses: *Ab initio* energies for the lowest two A' states. Red line: PES with additional terms. Green dashed line: standard PES.

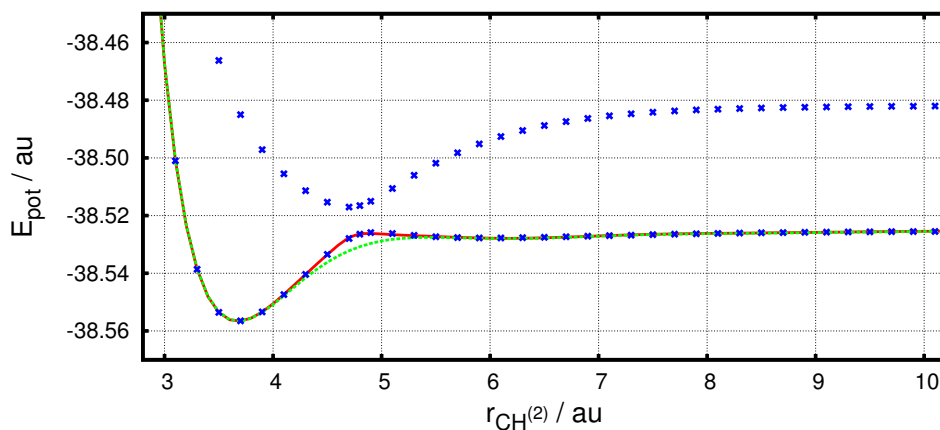
tersections can be shown visually. Figure 5.6 shows one-dimensional cuts through the PES for an incoming H atom with CH^+ at equilibrium distance in the collinear C-H-H and H-C-H cases. From the *ab initio* data it can be seen how the two lowest A' electronic states cross at the upper end of the potential well causing a small hump if one follows the lowest energy path over $r_{\text{CH}^{(2)}}$. The standard polynomial form of the PES can not reproduce this form and gives a fit "ignoring" this feature. The additional polynomials are able to compensate this shortcoming. The fit in figure 5.6 satisfactorily matches the intersections with corresponding heights of 68 meV and 99 meV above the asymptotic energy value, although the intersections are not spiky but smoothed.

Besides the conical intersections themselves, the regions with the avoided crossings are of particular interest from the fitting point of view. The development of the avoided crossings is shown for the example of the H-H-C intersection in figure 5.7 for 5° , 10° and 25° bending angle. At 5° , figure 5.7(a), the *ab initio* data still looks like the overlay of an attractive and a repulsive state. The avoided crossing only influences a small area directly around the former crossing point. The standard polynomial is therefore not able to reproduce the *ab initio* data in this region of the configuration space, while the additional polynomial does. Bending the molecule further to 10° , figure 5.7(b), the *ab initio* electronic states are now clearly separated. The lower state still shows an increased potential around the crossing region, which can not completely be reproduced without additional polynomials. At 25° , figure 5.7(c), one can find no sign of the avoided crossing and the standard polynomial potential accurately describes the *ab initio*. The electronic potential is altered by conical intersections and their residuals, the avoided crossings. The avoided crossings cause additional walls in the potential. If the height of a wall is higher than the asymptotic energy, this wall will have an influence on low energy dynamics. If the height is lower than the asymptotic energy it still might influence certain trajectories, but this can not be quantified. Following these considerations, the avoided crossings interfere with the reaction dynamics for bending angles up to approximately 5 - 10° . While this might influence the absolute values of the reaction probabilities, this region of the configuration space is too small to change the overall reactive behaviour of CH^+ , independent of temperature.

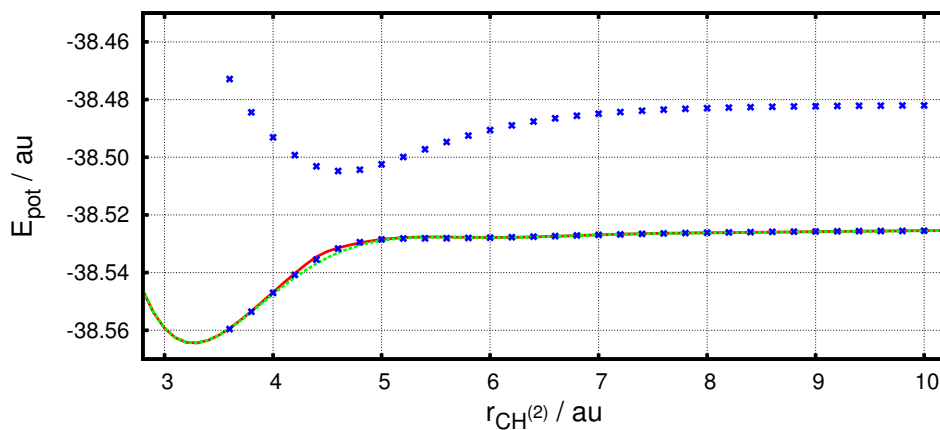
Another overview over the incoming channel is given in figure 5.8, where $r_{\text{CH}^{(1)}} = 2.14a_0$ is fixed again and the potential is given as a function of $r_{\text{CH}^{(2)}}$ and α . Figure 5.8(a) shows the complete channel, while figure 5.8(b) shows a more detailed map of the far-field potential of the incoming channel. If the H atom is approaching towards the bounded H atom, attractive forces are weaker compared to the approach towards the C atom. CH^+ has one free $2p$ orbit compared to its neutral counterpart. This yields a high overall electron affinity of the system, but the attractivity is mostly located at the C atom. The conical intersections for both collinear configurations can clearly be seen. Due to the avoided



(a)



(b)



(c)

Figure 5.7: One-dimensional PES cuts ($r_{\text{CH}(1)} = 2.14 a_0$) of avoided crossings for bending angles (a) 5° , (b) 10° and (c) 25° . Blue crosses: *Ab initio* energies for the lowest two A' states. Red line: PES with additional terms. Green dashed line: standard PES.

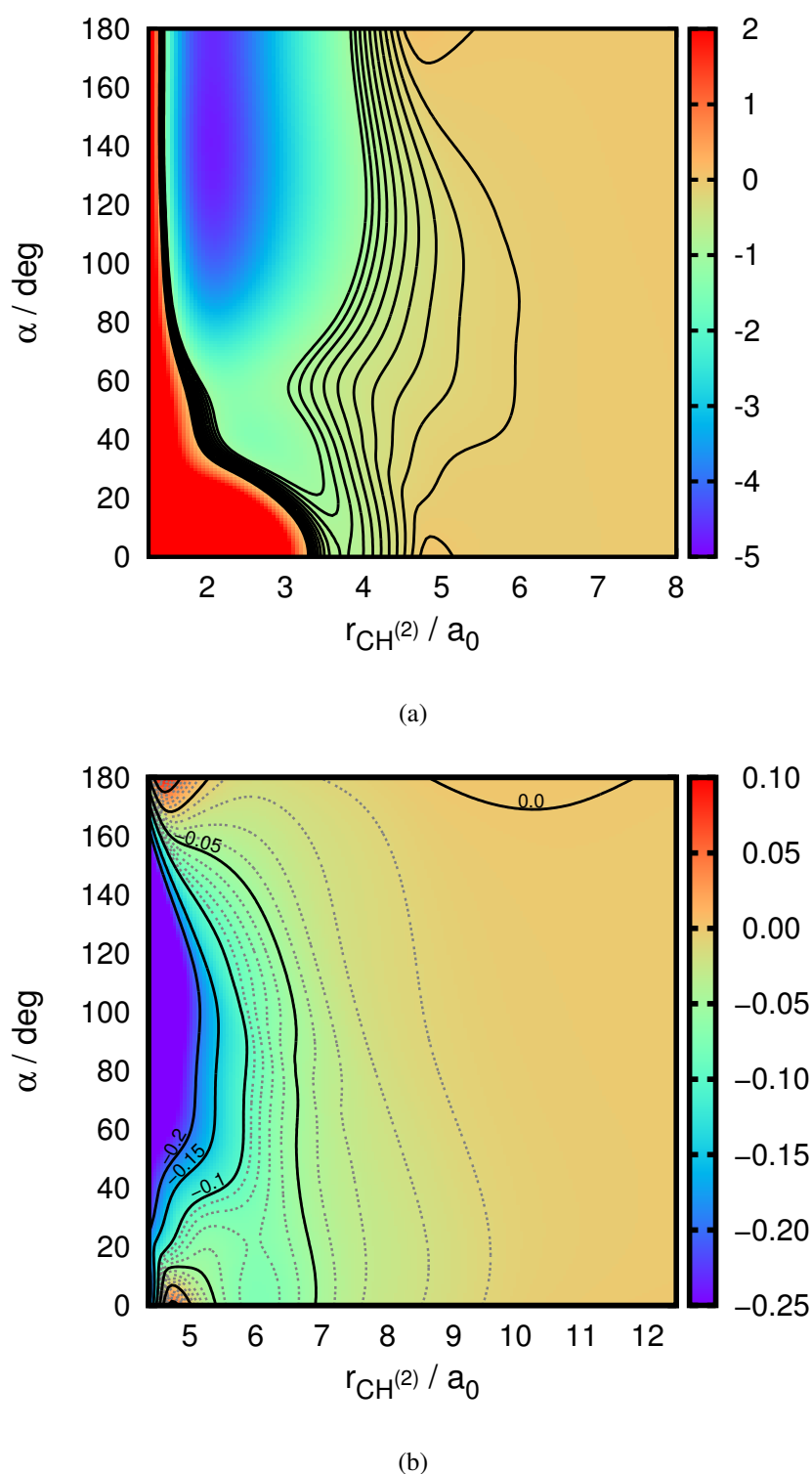


Figure 5.8: Two dimensional PES cut for fixed $r_{\text{CH}(1)} = 2.14 a_0$.

5.8(a): Contour lines between -1.0 eV and 0.1 eV are drawn with an increment of 0.1 eV.
5.8(b): Contour lines (black) are drawn between -0.2 eV and higher with an increment of 0.05 eV and (grey dashed) between -0.1 eV and 0.1 eV with an increment of 0.01 eV.

crossings at near linear configurations and the attractive character of the potential for bent configurations a clear gradient towards bent complex configurations around 80° to 160° appears. There is no barrier for an incoming projectile preventing the formation of a CH_2^+ complex, except while entering and staying in a collinear configuration, which is an unlikely event. The far-field interaction between CH^+ and H is crucial for the low temperature reactive behaviour. Therefore it has to be proven, that no artificial undulations are erected by the fitting procedure. For an incoming H atom the potential is purely attractive for all except near linear configurations. Around the 0° limit the potential is attractive for $r \geq 6a_0$, as can be seen in figure 5.6. The hump caused by the conical intersection reaches a height larger than the asymptotic energy limit for up to 7° of bending. At the 180° limit, the hump of the conical intersection is $> 0\text{eV}$ up to a bending angle of 168° . For this limit a region approximately between $9a_0$ and $11a_0$ has a potential value higher than the asymptotic limit with a maximum of 1.5 meV . This is an artefact of the fit. Due to the small amplitude and the narrow angular spread of this feature, the influence on the chemical dynamics should be negligible. Other artificial undulations were not found using contour plots of the incoming channel with a resolution of up to 5 meV . This implies, that classical trajectories with a projectile kinetic energy of at least 5 meV should not be compromised by the PES. A more detailed discussion of the influence of the PES on the dynamics is presented next.

5.3.2 Sensitivity studies for the potential energy surface

One major concern with *ab initio* based dynamics is the quality of the potential fit. Diagnostics of the fit can be done in several ways: e.g. visually, fit errors or comparison with experimental data. Another way is to perform exploratory studies on different fits. For this, ABC quantum scattering calculations were performed for $J=0$ to 2 with collisional energies up to 100 meV . The reference is the fit used in this work (std). For comparison the same fit without the extra polynomials for the conical intersection (wo) was used, the original fit scaled by 1.01 (scale) to fit experimental dissociation energies and an alternative fit (alt.). The alternative fit is 7th order two-body polynomial and 12th order three-body polynomial. The damping ranges λ were changed from $12a_0$ and $8a_0$ to $10a_0$ for both n-body terms. Figure 5.9 shows the respective cross sections.

The *ab initio* data for CH_2^+ underestimates the dissociation energies (see table 5.1) for all channels. The amount is varying but approximately 1% of the experimental values. Using the accordingly scaled potential for sensitivity study tests the influence of the correct dissociation energies on the dynamics. As the absolute values and the gradients are changed by the scaling this also gives insight in the general sensitivity on the exact potential form. The scaled potential does not show any significant change of the cross sections in figure

5.9. While the dissociation energy D_e is an indicator for the overall quality of the *ab initio* data, this value is not important for the (low energy) dynamics. It seems, that a scaling of 1% produces only minor changes in the gradients which govern the dynamics. This also suggests, that the usage of larger basis sets, like aug-cc-pVQZ, will not significantly improve the quality of the potential, assuming that no additional features are introduced. The comparison of my fit with the version which ignores the conical intersection tests the influence of the conical intersections and avoided crossings on the reaction dynamics. Figure 5.9 shows increased cross sections for energies below 10 meV. While this can be seen easily for $J=1$ and 2, this effect is more hidden for $J=0$. In the figure this is reflected as a maximum around 3 meV. The influence of the conical intersection on the dynamics appears to be rather small, which corresponds to the small fraction of the configuration space of the incoming channel which is perturbed by the intersections and avoided crossings.

The largest difference appears in the comparison with the alternative 12th order fit. This fit uses different parameters and has similar root mean square like the fit used in this work. The different order and damping ranges primarily change the potential at the pre-dissociation and dissociation regions. To be more precise, polynomial fits have unavoi-

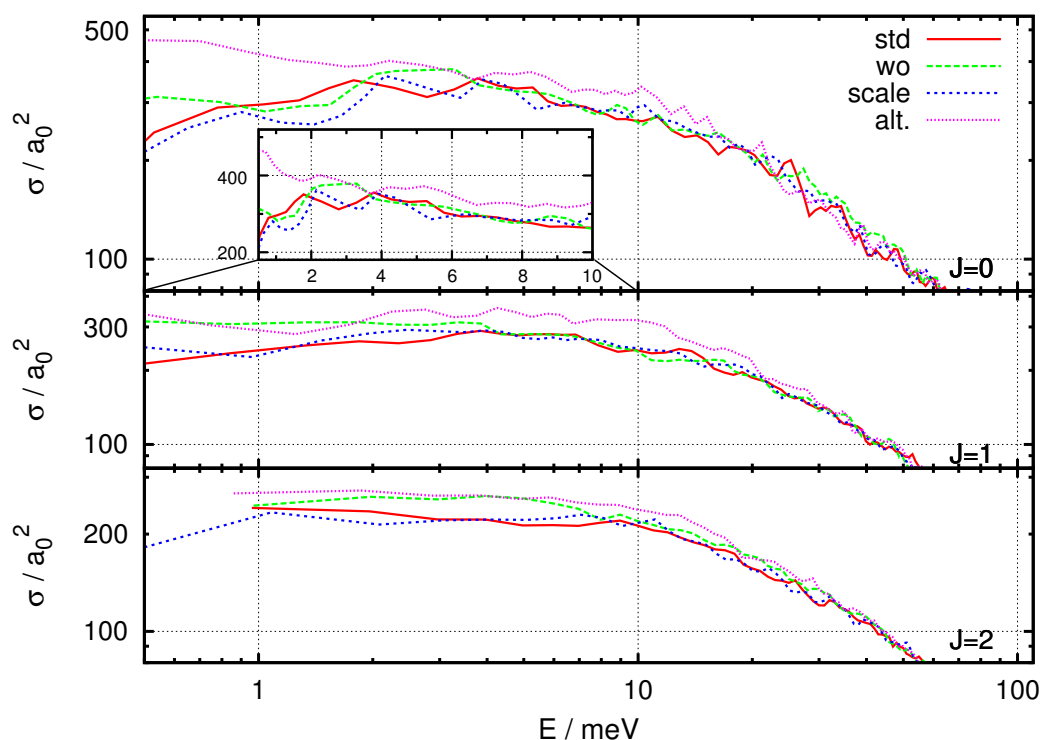


Figure 5.9: Comparison of ABC quantum scattering abstraction cross sections for initial rotational quantum numbers 0 to 2. std = standard fit in this work, wo = standard fit without conical intersection terms, scale = standard potential scaled by 1.01 to fit D_e s, alt. = alternative fit using different parameters (see text).

able modulations in these regions. Their form is changed by the modified parameters. In this case the low energy cross sections are significantly increased. Such deviations can be expected from the root mean square errors of the fits between 10 meV and 20 meV, while these errors do not state how strong the uncertainties of the cross sections are. The deviations are found to be about 10%. Also the low energy limit has a flatter slope. Extrapolated to the rate constants this would mean an uncertainty of approximately 10% at the lower limit which decreases with temperature and should be negligible above 50 K.

5.3.3 Cross sections

5.3.3.1 Comparative study of QCT weightings

As mentioned in section 5.2.3, the quality of QCT calculations varies very much with systems under surveillance. Before reaction cross sections are shown and analysed, the different QCT weightings are compared.

The C^+ abstraction and inelastic collision cross sections for $J=0$ are compared in figure 5.10. ABC quantum scattering cross sections are taken as reference, since no experimental data is available. The abstraction cross section are expected to be large at low energies and drop with increasing energy. The inelastic collision cross sections must be zero below 3.45 meV. For higher energies they should increase. This is expected according to thermal partition function considerations, see 5.3.3.2. The ABC curve is matching these criteria.

The first candidate for the comparison is the standard histogram binning (HB-QCT). Its cross sections show much less variation with energy than the ABC results. Especially the fact, that HB-QCT completely ignores that there can not be any inelastic collisions at low energy, disqualifies this method. It rather stays at the same value for all energies.

The next candidate is the Gaussian weighting. It is expected to eliminate "wrong" trajectories from the set and therefore improves the cross sections. Yet, this is only rigorously true for the limit of very small weighting widths, where only trajectories with almost integer quantum numbers are left. This set is small for small s_α and probably empty in the limit of the Dirac distribution. A tremendous amount of trajectories have to be calculated to gain a reasonable set size. A small set on the other hand introduces statistical errors. Medium weighting widths, which decrease the influence of false trajectories but keep a reasonable large set have to be used. While the Gaussian weighting is physically motivated, it does not necessarily deliver accurate results. This can be the case, if the classical S matrix theory does not adequately describe the system at hand. It is also possible that one can not calculate enough trajectories for a sufficiently small weighting width. The GW-QCT curve in figure 5.10 is calculated with $s_\alpha = 0.002$ for all trajectories. This is roughly a factor of 8 smaller than the one used by Halvick *et al.*. As can be seen, the low

energy inelastic cross sections are decreasing by almost a factor of 100 to approximately $1 - 2a_0$. This is a difficult case for any statistical technique, as the set of (allowed) trajectories for low energies is zero for some channels. If the conditions are not rigorous, e.g. Gaussian instead of Dirac distribution, these cross sections are naturally very noisy. The general form of the cross sections has improved considerably, yet the abstraction cross sections are underestimated by the GW-QCT. The high energy abstraction cross sections get deteriorated by the weighting since an artificial minimum appears.

The modified Gaussian weighting (mGW-QCT) is a purely empirical treatment and was chosen to prevent the population of forbidden final states. While this method efficiently erases forbidden reaction paths from the set, there is a risk of artificially preferred channels caused by the unequal weighting. Using values of $s_\alpha = 0.004$ and 0.015 for CH^+ and H_2 forming channels, respectively, I get the mGW-QCT curve in figure 5.10. The s_α are increased linear with the energy. In this case, the abstraction cross sections better fit the ABC results. Yet, neither QW-QCT nor mGW-QCT could deliver a constant quality for all calculated cross sections.

5.3.3.2 Quasi classical trajectory

Initial state selected cross sections from 4.0 million QCT trajectories have been computed for $J = 0, \dots, 10$ and collision energies of 1, 2, 4, 8, 16, 30, 60, 100 and 200 meV. for the lowest energy initial conditions I used $s_\alpha = 0.002$ for the standard Gaussian weighting (GW). For the modified version mGW $s_\alpha \sim B_\alpha/k_\alpha$ was used, resulting in $s_\alpha = 0.004$ and

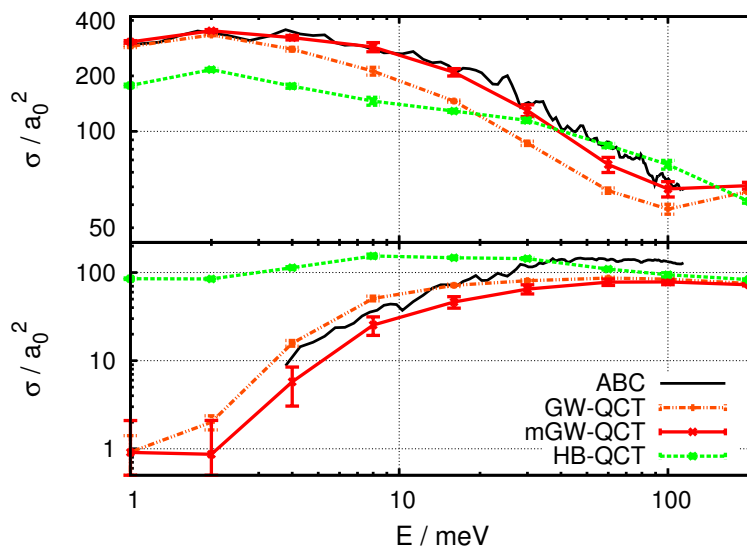


Figure 5.10: Comparison of $J=0$ QCT cross sections (Upper plot: abstraction, lower plot: inelastic collision.) for different binning techniques with ABC quantum scattering results as reference. For a description of the techniques see the text.

0.015 for CH^+ and H_2 forming channels, respectively. For initial conditions with higher energies such small weighting widths are not necessary as the rotational level splitting increases and therefore more energy has to be transferred from the zero point energy to the rotational degree of freedom to open a closed rotational energy path. In addition, a small weighing width diminishes the statistics. Therefore, the width was increased for initial conditions with high energy, such that the quantum mechanical results are resembled as good as possible. As mGW-QCT shows the best results of the three weighting methods, these are presented in this section.

The behaviour of the cross sections in dependence of the rotational state of the reactants and the collisional energy is a superposition of the dependence of the maximal impact parameter and the relative probabilities. The maximum impact parameter for all collisional channels are identical for almost all cases. Their deviation is usually less than 1%, which is well within the convergence limit uncertainty. The maximal impact parameters, as shown in figure 5.11, are relatively independent of the rotational energy of CH^+ if $J \geq 2$. A small variation of the maximum impact parameter for different J can be seen, yet this effect is small with changes between $0.2 a_0$, for 200 meV, and $0.5 a_0$, for 1 meV. For $J \geq 2$ the impact parameter is decaying for increasing collisional energy from roughly $12.6 a_0$ ($J = 10$) to $7.2 a_0$ ($J = 10$) for 200 meV. This is expected, as higher relative velocities decrease the interaction between the far field potential of the target and the projectile, re-

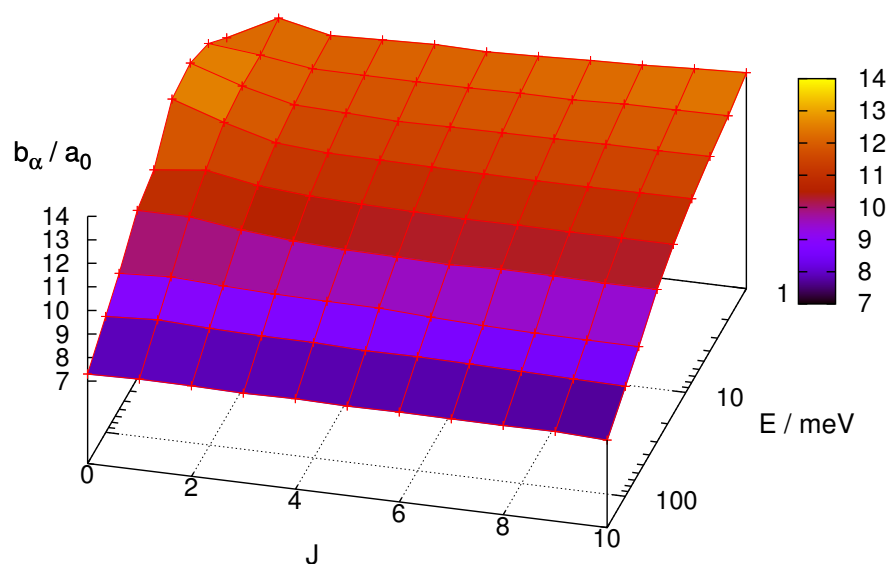


Figure 5.11: Maximum impact parameter in a_0 over initial rotational quantum number and initial kinetic energy.

ducing the deflection of the projectile. The same kinetic energy dependence can be found for $J = 0$ and $J = 1$, yet the impact parameters are larger here. Especially the $J = 0$ impact parameters for energies ≤ 8 meV are increased by approximately $1 a_0$. The 1 meV impact parameter is $0.3 a_0$ smaller than the $J = 1$ value. Comparisons with quantum scattering results (see 5.3.3.3) indicate that this decreased impact parameter is no artefact of the QCT method, but a characteristic of the PES. This is produced by the collinear and near-linear regions of the potential. As this is limited to very low kinetic energies this is most likely not a product of the conical intersections but of the limited accuracy of the fit, as discussed in section 5.3.1.

Another important factor is the partition function. The first rotational level of CH^+ has a rotational energy of about 3.45 meV. If the total energy is less than this, no inelastic collision can happen and the H-exchange reaction has only one accessible energetic path. If the energy increases more paths open, however the inelastic case has always less paths available than the exchange case. The situation for the C^+ -abstraction is rather different, as the product composition is different. H_2 has a smaller zero-point energy compared to CH^+ , allowing several paths even for low collisional energies. On the other hand the rotational level splitting is larger, thus the increase of open paths with higher energies is slower than for the other reaction channels. If not governed by other factors, cross sections should decrease with larger collisional energy. The abstraction cross section should be large for small total energies and decrease with larger energies. Inelastic and exchange cross sections should be zero or small for low energies and increase with larger total energy. Both cases should behave similarly.

In the following selected mGW-QCT cross sections are discussed for inelastic collisions, H exchange and C^+ abstraction, respectively, for different initial rotational states as a function of collisional energy. Error bars are the $2s_{\sigma_\alpha}$ confidence intervals obtained from equation (5.10). This error estimate is dominated by the weight w related term. The b_α and N related terms are smaller than $0.025 \sigma_\alpha$ and $0.004 \sigma_\alpha$, respectively. The Ω_α related term, which accounts for the s_α parametrisation is large, up to $0.33 \sigma_\alpha$, for small total energies. There the energy differences between rotational states are small and a smaller s_α would be needed. This would lead to a slower convergence of w , which would require more trajectories to be calculated than feasible. To give an overview the cross sections for the whole initial condition parameter space are shown in surface plots.

Figure 5.12 shows initial-state selected inelastic collision cross sections. For $J = 0$ and $E_{\text{coll}} < 3.45$ meV these should be zero. Using the Gaussian weighting it was possible to get the cross sections as small as approximately 1 meV. The errors bars are significant for small cross sections. This is directly related with the small fraction of trajectories with a large weight for these cases. The cross sections are increasing for increasing J as well as increasing kinetic energy. This is consistent with the expectations from the partition

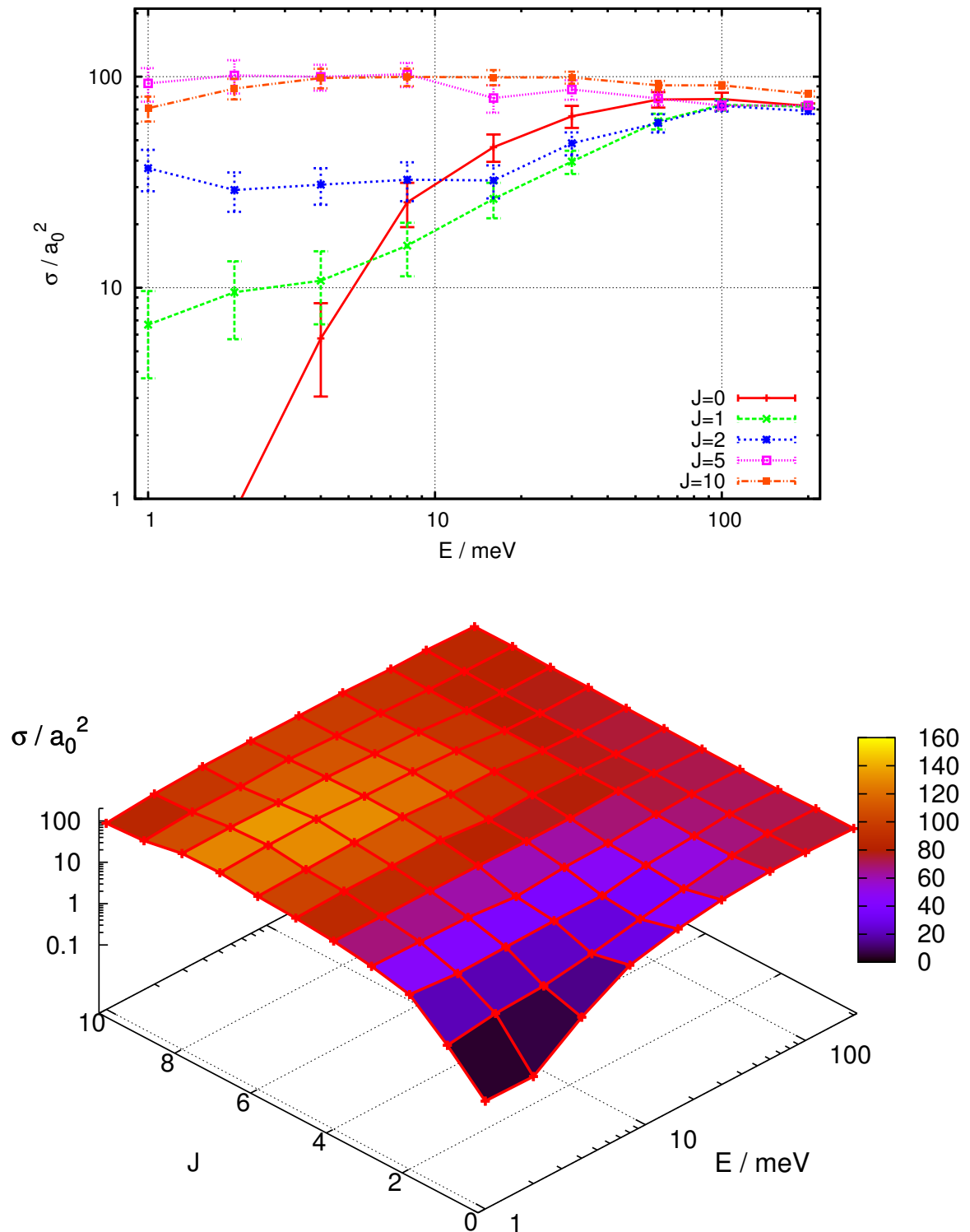


Figure 5.12: mGW-QCT inelastic collision cross sections. Upper: Plot for several values of the rotational quantum number J versus the collision energy. Lower: Cross sections versus J and collision energy.

function considerations. For the largest kinetic energies in this work, 200 meV, the cross sections are rather constant over the rotational quantum numbers and vary between $70a_0^2$ and $84a_0^2$. For lower kinetic energies, less than 16 meV, the cross sections show a maximum in J around $J = 7$ with a height of $150a_0^2$. It is not clear, why this maximum is arising. For $J = 10$ the cross sections show only small variations depending on the kinetic energies, around $70a_0^2$ to $100a_0^2$. For kinetic energies larger than 200 meV the cross section will decrease independent of rotational energy at some point, as the lowered impact parameter will show its effect.

The H-exchange cross sections in figure 5.14 show, as expected, a similar low energy behaviour like the inelastic collisions, but with some considerable differences for larger kinetic and rotational energies. The exchange cross sections show a maximum along changing kinetic or rotational energies for most of the parameters covered in this work. The absolute maximum is at $134a_0^2$ for $J = 3$ and $E_{coll} = 16$ meV. One reason for the low high energy cross section can be found in the time in complex of the trajectories. Figure 5.13 shows the times in the complex regions for a number of different trajectories. The initial conditions in this case are $J = 5$ and $E_{coll} = 100$ meV. As can be seen, one fourth of the inelastic collision trajectories have complex lifetimes of less than 10 fs. These cases are more probable for larger kinetic energies and to a smaller extent also for larger ro-

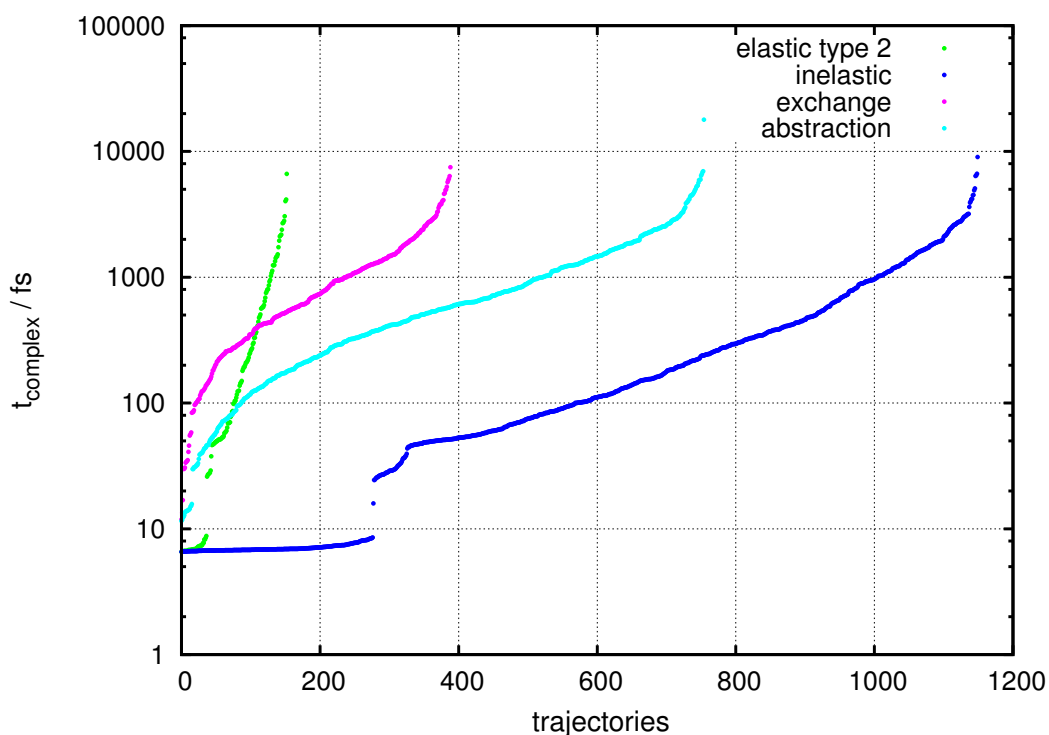


Figure 5.13: Time in the complex region for a number of trajectories with the initial conditions $J = 5$ and $E_{coll} = 100$ meV.

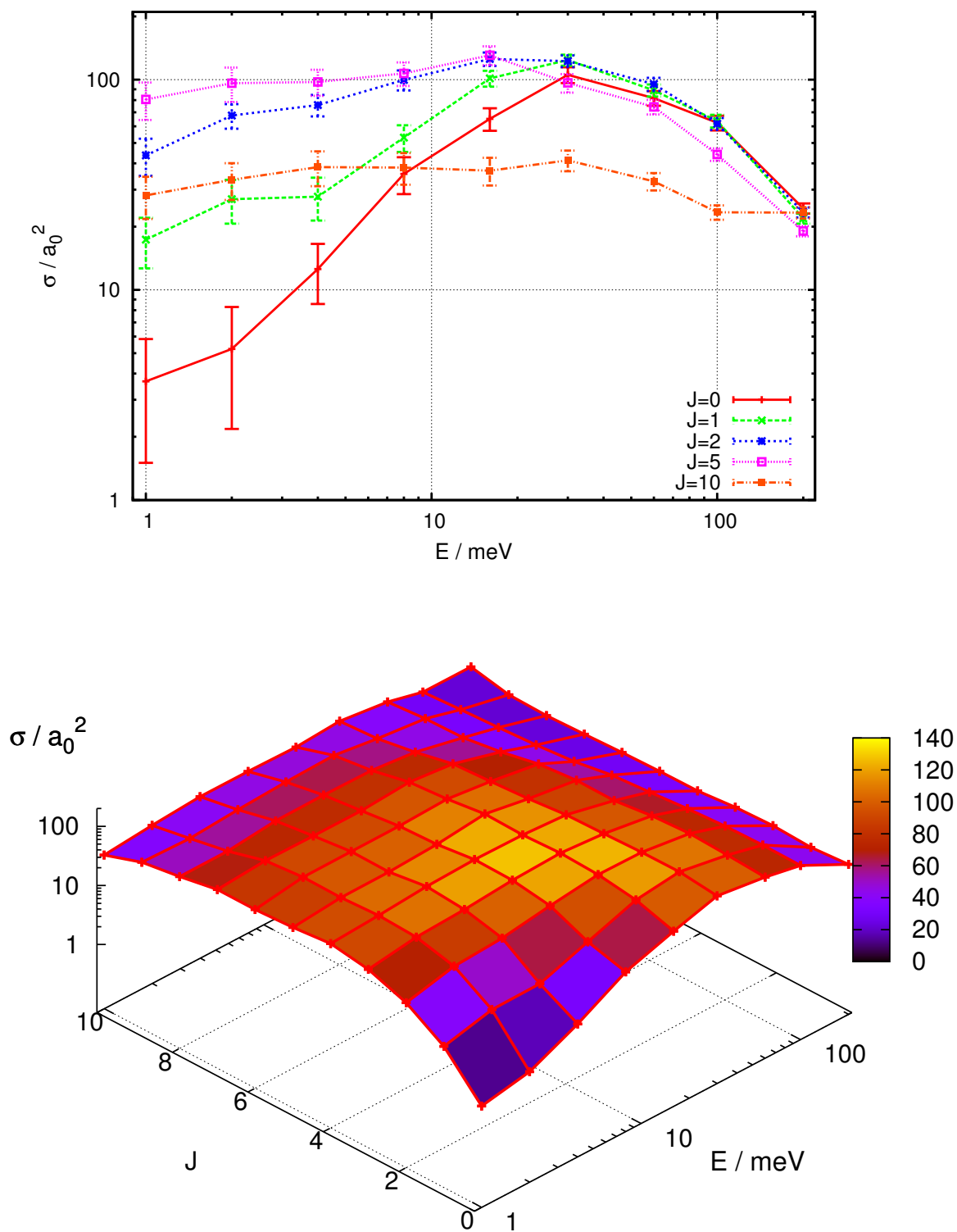


Figure 5.14: mGW-QCT H exchange cross sections. Upper: Plot for several values of the rotational quantum number J versus the collision energy. Lower: Cross sections versus J and collision energy.

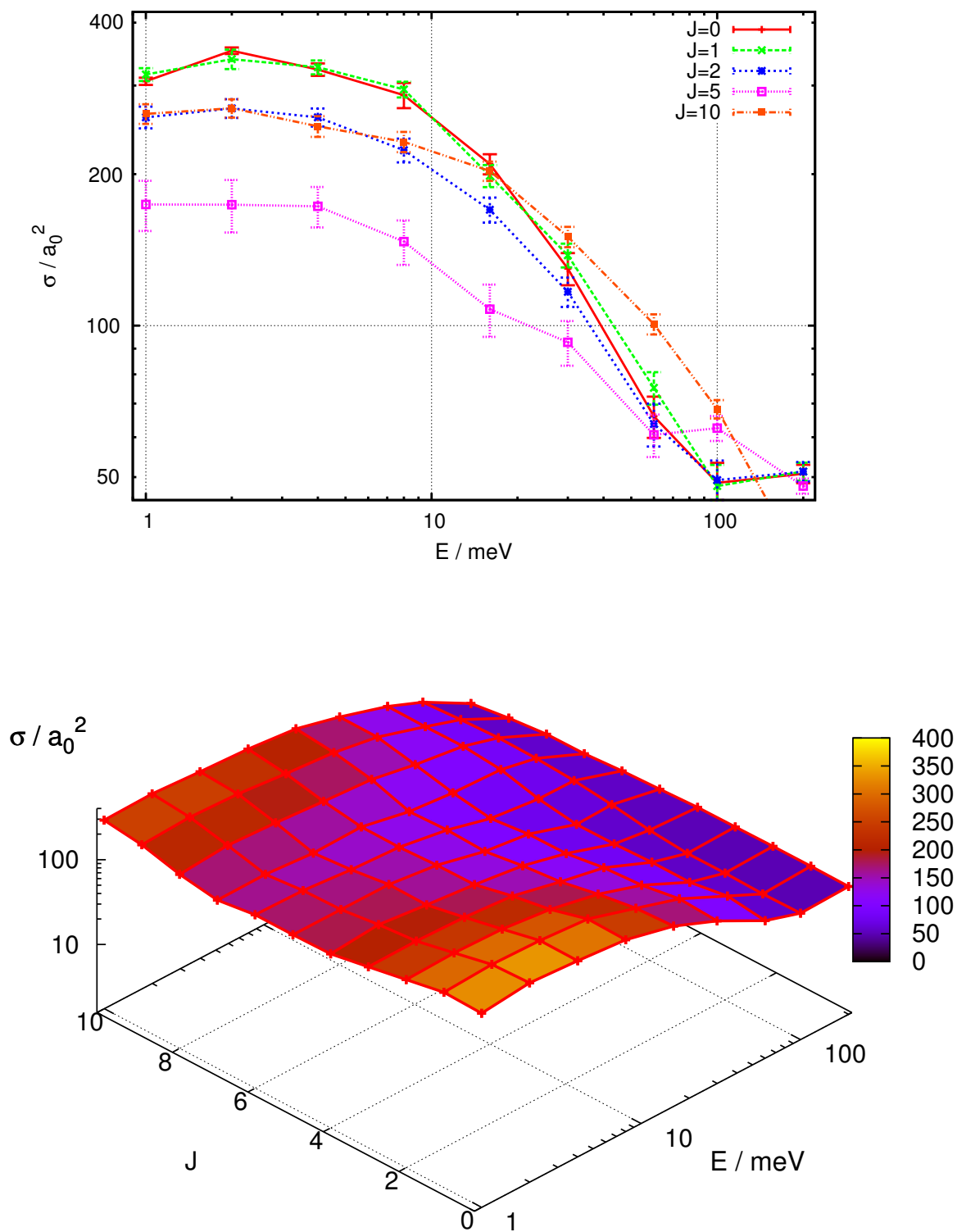


Figure 5.15: mGW-QCT C^+ abstraction cross sections. Upper: Plot for several values of the rotational quantum number J versus the collision energy. Lower: Cross sections versus J and collision energy.

tational energies. If this part is subtracted the relative partition of complex life times is identical for all channels. Still, the exchange channel has much less trajectories. This is unexpected, because after a certain time in the complex region all information about initial conditions is gone and the system can not distinguish between the two hydrogen atoms. Which one is separated in the end should be completely random.

The C^+ abstraction cross sections, as shown in figure 5.15, are large at low energies with a maximum of $350a_0^2$. The abstraction cross section decrease with higher kinetic energies due to the combination of smaller impact parameters and the slower increase of the partition function. The J dependency is rather unexpected. Up to $J = 7$ the cross sections are decreasing, which is expected, but afterwards, they are increasing again. At least this fits to the decreasing cross sections of the other channels. A possible explanation might be connected with the centrifugal distortion of the molecule. For high rotational energies the effective binding of the molecule is decreased due to centrifugal forces. This can increase the probability that the molecule is torn apart upon a collision with another atom.

Another possible explanation for the switching (increase/ decrease) behaviour with changing J is rotational shielding. The centre-of-mass for CH^+ is near the carbon ion. If brought into rotation the hydrogen is shielding the carbon, changing the probabilities, whether an incoming projectile is hitting one or the other. For higher kinetic energies of the projectile this is compensated. It is plausible to assume, that after a certain point, the shielding reaches an optimum and can not be improved further. Previous publications[73, 93, 94] claim, that the rotational shielding prefers the product channels with light atom separation.

5.3.3.3 Quantum scattering

As the reliability of QCT cross sections strongly depends on the weighting, the number of trajectories and whether additional quantum mechanical effects are important, a cross check with another method is useful. A series of quantum scattering calculations using the ABC code was performed. The initial diatomic rotational quantum number was restricted to $J \leq 5$ due to computational limitations.

The inelastic collision cross sections, which are compared in figure 5.16, show a good qualitative agreement for the cross sections with small kinetic energy, besides the $J = 1$ ones, which are decreased too strong by the Gaussian binning. For both methods the high kinetic energy cross sections show a decreasing rotational dependence and seem to reach plateau values. The ABC plateau is approximately a factor of two higher than the QCT one, yet the overall physical behaviour is consistent.

The comparison of exchange cross sections in figure 5.17 shows much less agreement between the methods. Both methods predict a decreasing rotational dependency over energy, which is found in all results of this thesis, but the cross sections seem somehow

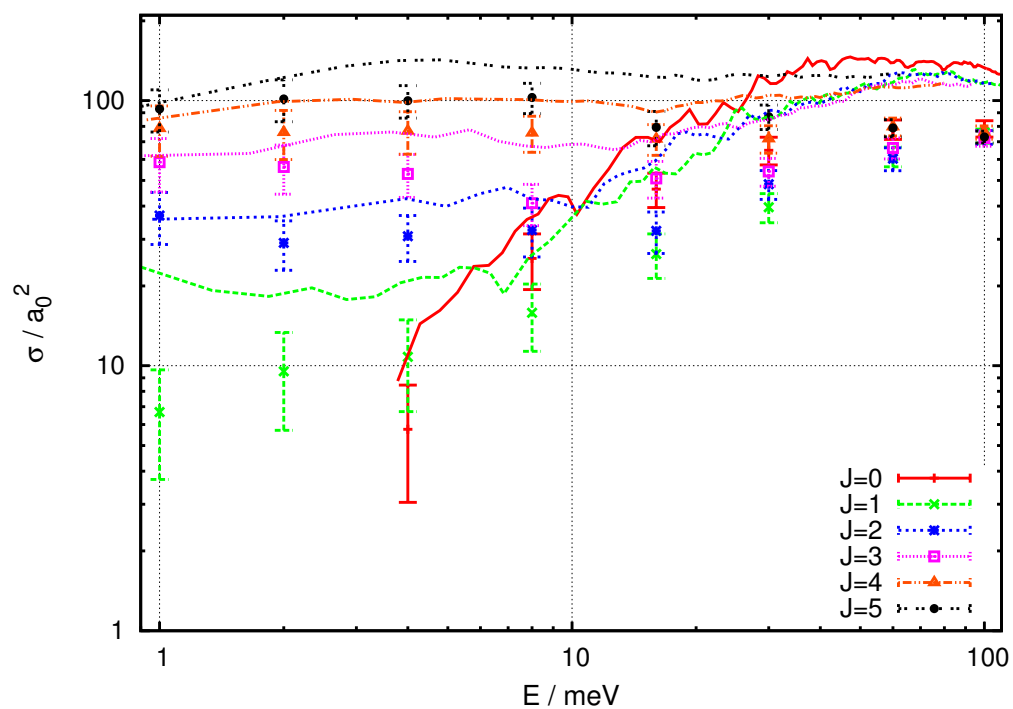


Figure 5.16: Low energy inelastic collision cross sections from mGW-QCT (dots with error bars) and ABC (lines) calculations.

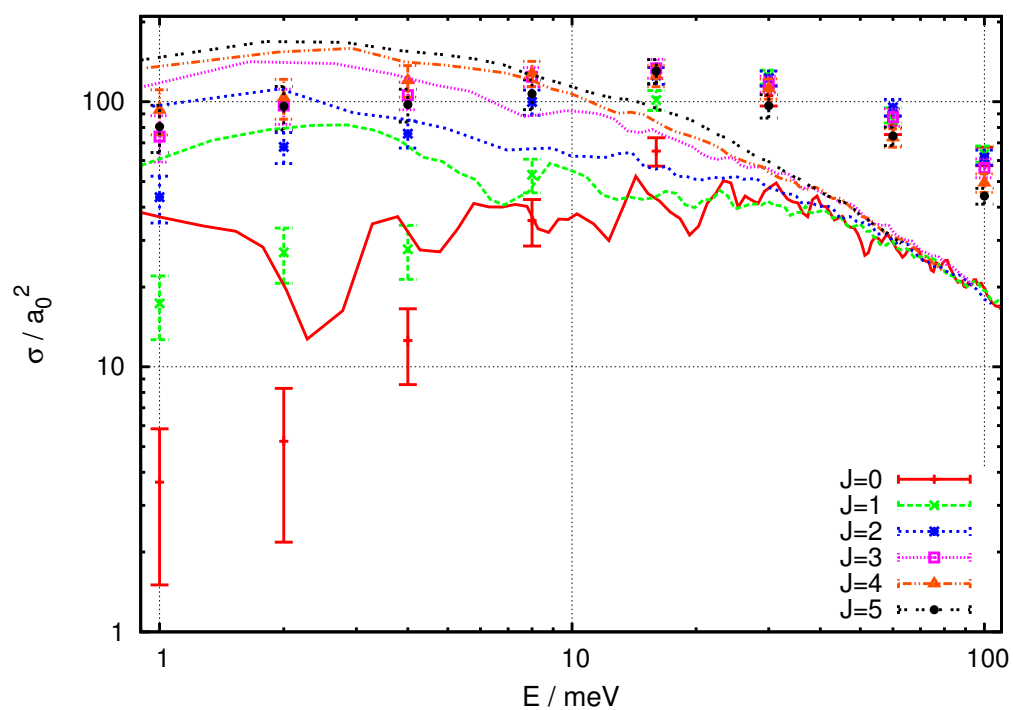


Figure 5.17: Low energy H exchange cross sections from mGW-QCT (dots with error bars) and ABC (lines) calculations.

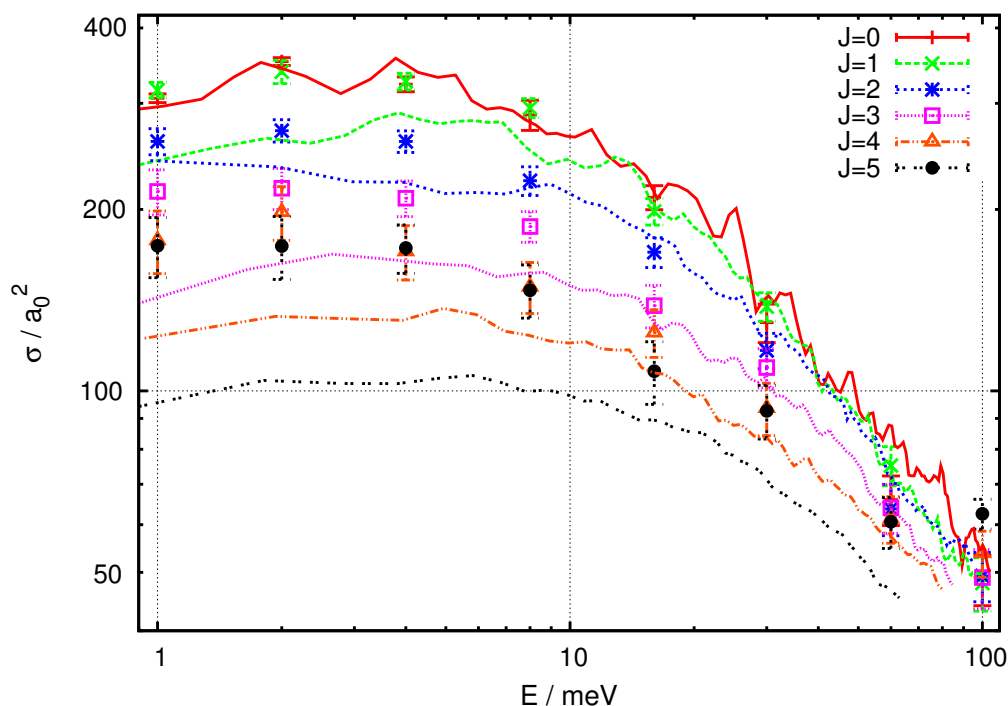


Figure 5.18: Low energy C^+ abstraction cross sections from mGW-QCT (dots with error bars) and ABC (lines) calculations.

tilted. The mGW-QCT low energy cross sections are overestimated due to the weighting, especially for low rotational energies, but they stay at a much higher level for larger kinetic energies. The ABC cross sections do not show the maximum for medium kinetic energies, but decrease over the energy. The ABC results are more realistic in terms of physics. As mentioned already the two major factors are impact parameters and partition functions. While the ABC cross sections decrease as predicted by the impact parameter with increasing collisional energy, they are increasing with rotational energies, which reflects the increasing probability of this channel over J if a complex is formed.

Figure 5.18 shows a comparison of mGW-QCT and ABC low energy abstraction cross sections. For $J = 0$ to 2 the QCT results are mostly following the ABC results. Both methods yield similar results here. For $J = 3$ to 5 QCT cross sections are generally larger than the ABC results, which implies a stronger J dependence of the abstraction cross sections.

5.3.4 Rate coefficients

The energy range chosen in this work allows to calculate rate coefficients up to 300 K. As cross sections are only calculated for energies of 1 meV and larger, their dependence for smaller energies is unknown. Therefore, several low temperature limits (linear, constant,

divergent) were used, where the constant and divergent limits give almost identical results. With the exception of inelastic collisions, which do not appear for the low temperature limit, maximal corrected rates are given as an upper bound of the real value. QCT reaction rate coefficients are given for standard histogram binning (HB-QCT), Gaussian weighting (GW-QCT) and the modified Gaussian weighting (mGW-QCT). ABC cross sections were calculated up to 60 meV only. Therefore, ABC rate coefficients are restricted to 150 K. The results are compared with previous published numerical work of Halvick *et al.* which is based on the Stoecklin and Halvick PES. They used GW-QCT as well as phase space theory (PST) methods. Their maximal cross sections are larger, implying a larger maximal impact parameter of at least $25 a_0$, which is approximately twice the size as in this work.

Figure 5.19 shows inelastic collision rates from QCT and ABC calculations compared to QCT results of Halvick *et al.*. The Halvick *et al.* coefficients are larger than the ones in this work, besides the HB-QCT results, which are intrinsically overestimates for this system. ABC, GW-QCT and mGW-QCT results are similar. The results of Halvick *et al.* are generally larger with decreasing difference for higher temperature due their larger low energy cross sections. Therefore, it originates from an area of the parameter space, where both potentials can not be considered as reliable.

The picture for the exchange reaction is looking rather different, as can be seen from

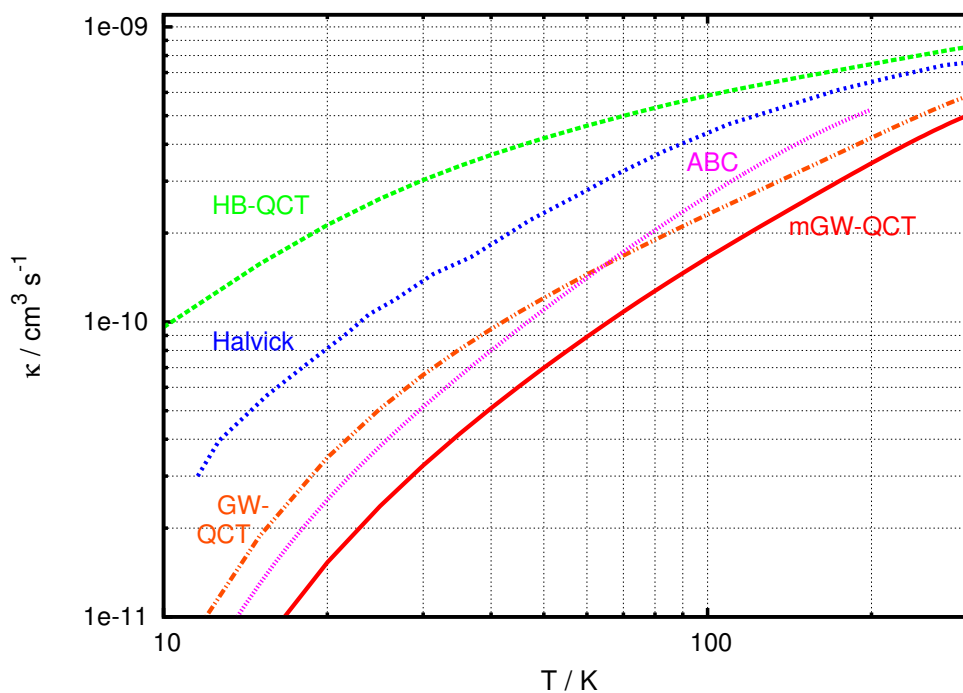


Figure 5.19: QCT and ABC rate coefficients for the inelastic collision channel. For comparison the QCT results of Halvick *et al.* are given.

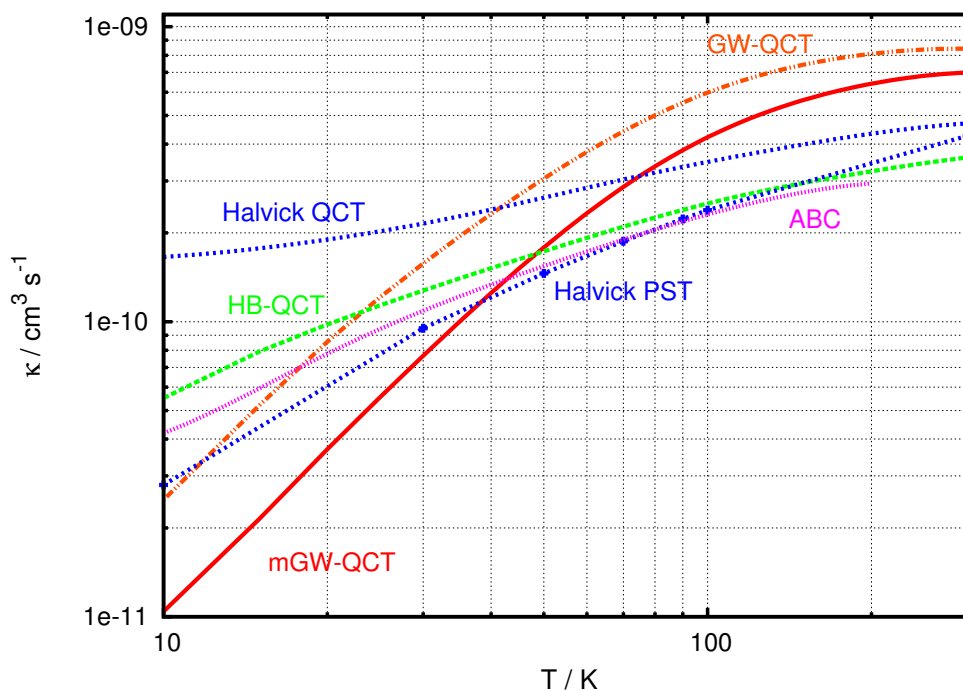


Figure 5.20: QCT and ABC rate coefficients for the exchange reaction channel. QCT and PST rate coefficients from Halvick *et al.* are shown as well.

figure 5.20. Good agreement is found between PST, HB-QCT and ABC results, while all weighted QCT results are off. The GW- and mGW-QCT results from this work have a too steep slope and a high temperature limit, which is almost twice as high as PST and ABC results. The low energy mGW-QCT cross sections are too small compared to the ABC ones. On the other hand I find too large high energy cross sections. It seems that Gaussian weighting distorts this particular channel, while the other two are improved over HB-QCT.

Previous numerical results show a monotonic behaviour for QCT and PST abstraction rate constants. This is in agreement with theoretical expectations and experimental results, e.g. from Luca *et al.*[95] and Federer *et al.*[96, 97]. Newer experiments from Plasil *et al.*[74–76] show a different low temperature behaviour. As can be seen in figure 5.21, where they measured small low temperature rate coefficients, e.g. $5 \cdot 10^{-11} \text{ cm}^3 \text{ s}^{-1}$ at 12.2 K, which are increasing rapidly up to 60 K. For higher temperatures their measurements coincide with results from Luca *et al.*, which are not shown in the figure. The QCT and ABC results from this work are generally lower than the results of Halvick *et al.*. Both numerical works agree on the same level with experiment, although they are separated by a factor of two. My results show a different behaviour for temperatures lower than 50 K as they have a positive slope. Although this work shows a drop of the reaction rate for low temperatures, this strong decrease could not be reproduced, except for HB-QCT. Yet

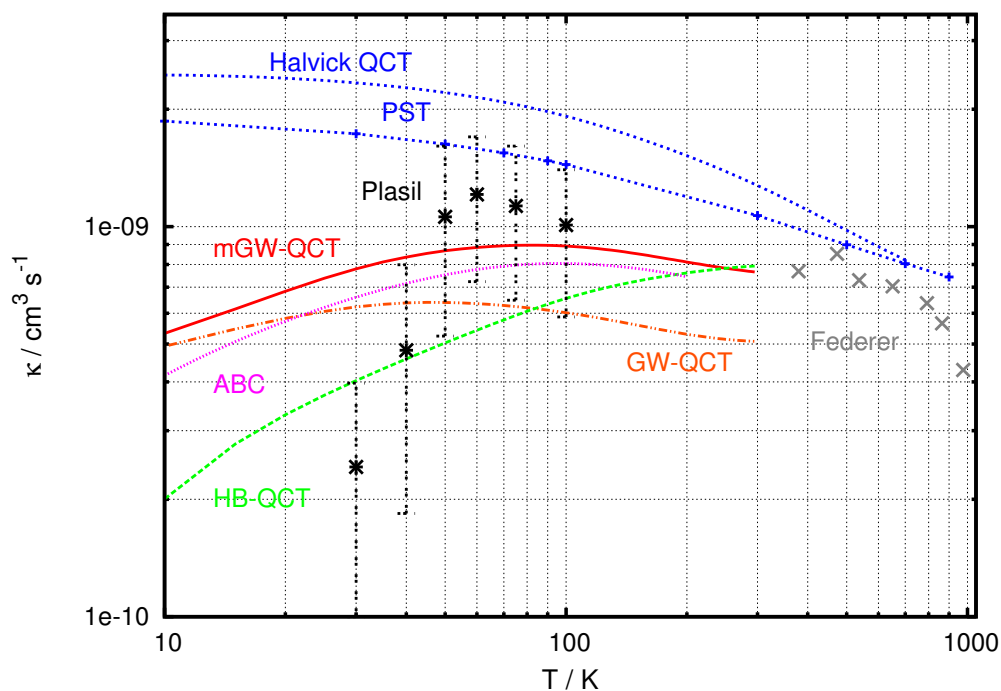


Figure 5.21: QCT and ABC rate coefficients for the abstraction reaction channel. QCT and PST rate coefficients from Halvick *et al.* are shown as well. Experimental rate constants from Luca *et al.* and Federer *et al.* are also included.

HB-QCT underestimated the low temperature rate coefficients as it underestimates the corresponding cross sections. The lower reaction rate coefficients for low temperatures in this work are caused by the relatively small impact parameters at low kinetic energies, which are defined by the far field potential.

5.4 Recap

In this chapter the reaction dynamics of $\text{H} + \text{CH}^+ \rightarrow \text{C}^+ + \text{H}_2$ was studied. This reaction is important for the CH^+ chemical equilibrium in interstellar environments containing both hydrogen and carbon. The predicted CH^+ abundances in these regions do not match measured data. Additionally, Gerlich and co-workers presented newer experimental reaction rates, which diverge from previous numerical expectations. This motivated the investigation in this work.

A new potential energy surface for the $\text{H} + \text{CH}^+$ reaction was presented. The potential has a root mean square error of about one order of magnitude smaller than the one of Stoecklin and Halvick. Based on this *ab initio* potential reaction cross sections and rate coefficients were calculated with quasi classical trajectory (QCT) and quantum reactive

scattering methods. The standard Gaussian weighting QCT C^+ abstraction cross sections are too small compared to quantum reactive scattering results. Therefore, a new empirical modification, mGW-QCT, is introduced, which improves the C^+ results significantly. In this work a smaller Gaussian weighting width is used than Halvick *et al.* and therefore the weighting errors for low energy cross sections is reduced. The potential and QCT results in this work are improved compared to previous numerical work.

Discrepancies between different numerical studies indicate a high sensitivity of low temperature reaction rates to the electronic potential used. Fitted *ab initio* potentials have fitting errors in the order of 10 meV. Depending on the functional form used, the far field potential can be distorted from the underlying *ab initio* data by several meV. This can deteriorate low kinetic energy dynamics using such a potential.

The C^+ abstraction rate coefficients from mGW-QCT and ABC agree well with the standard picture for temperatures larger than 60 K. For lower temperature previous numerical studies predict the same monotonic behaviour. This work and the experiment from Plasil *et al.* show a reduced rate coefficients for lower temperatures. The experimental results show a drastic inhibited reaction, which can not be found in this work.

This chapter demonstrated the application of computational chemical physics methods to reaction dynamics.

Conclusions

Computational chemical physics can give important input to astrophysical modelling and other fields of physics, where molecular properties are of importance. The aim of this work was to investigate the capabilities and limitations of *ab initio* based potential energy surfaces for spectroscopic and reactive studies and to apply these methods to problems of rovibrational and rovibronic spectroscopy and reaction dynamics.

The choice of *ab initio* methods and the potential fitting methods is critical for the computational chemical physics, since all further quantities directly depend on their quality. In this work modified versions of the Braams polynomial potential energy surface were used. A series of *ab initio* based computational chemical physics calculations have been performed covering spectroscopic and reactive applications of astrophysical interest. It was possible to improve the spectroscopic data of CH₄, MgH and reactive data of CH₂⁺. New partial spectroscopic data for MgH were obtained expanding the spectrum into the near ultraviolet region.

A high level coupled cluster *ab initio* method was used to build potentials for a series of small hydrocarbons. Hydrocarbons, especially of the CH_x and C₂H_x series, can be found almost everywhere on earth and in the universe. They exist in laboratory plasmas, stellar and planetary atmospheres and interstellar gases. In all these cases, light emitted or absorbed by the molecules is an important or even the only diagnostics of the system. The potential constructed in this work partly included a cluster expansion, which adds reactant configuration spaces to the fits. This could not be done for CH₃ and higher hydrocarbons, because of the limitations of the Coupled cluster *ab initio* method, which is well suited for the potential wells, but not for the dissociation regions. The examples of methyl and methane show how the potentials can be used for rovibrational spectroscopy. Results of radiation transport simulations illustrate the importance of as complete-as-possible line lists for radiation transport calculations.

The rovibronic spectroscopy of diatomic molecules is another important aspect for the stellar atmospheric modelling. Metal hydrides and oxides add opacity to the atmosphere in the visible light and ultraviolet frequency regions, as well as do the hydrocarbons in the infrared one. In addition the spectra of metal hydrides/oxides can be used to gather infor-

mation about metal and their isotope abundances. They are used as markers for the conditions in the atmospheres of stars. In this work a new code was developed, that efficiently calculates bound-bound transitions between electronic states and bound-continuum cross sections for diatomic molecules. It also offers an adequate treatment of quasi-bound rovibrational states. One important representative of the diatoms is magnesium hydride, MgH. Before this work, line lists and photodissociation cross section were available involving the three lowest doublet states of MgH. In this work new potential energy curves were calculated and adapted to updated experimental data. This causes changes in the relative energies between the electronic states and therefore shifts in the line lists. These are important, because accurate line positions are needed for the identification of spectral lines. In addition two further electronic states were included in the calculations. This expands the spectral range of MgH into the near ultraviolet region. Radiation transport models showed significant absorption by MgH from the newly added electronic states. A second usage of the diatomic potential energy curves are photodissociation cross sections. As interstellar environments are chemically active, such data is necessary for a complete picture of the ongoing processes. The photodissociation cross sections of MgH reveal a stronger dependence of the underlying potential than the bound-bound lines. In the case of MgH the cross sections are rather weak, besides occasional resonance lines which can be several order of magnitudes stronger.

As mentioned, not only spectroscopic, but also reactive behaviour of molecules is important in astrophysics. A current problem connected with this is the abundance of CH^+ in interstellar clouds. Its measured abundances do not fit the predictions from theoretical models. In addition Gerlich and co-workers recently measured low temperature $\text{H} + \text{CH}^+ \rightarrow \text{C}^+ + \text{H}_2$ reaction rates, which diverge from the theoretical picture and which could not be explained. In this work I built a reactive potential energy surface for the CH_2^+ system, which was then used to perform extensive calculations with quasi-classical trajectory and quantum scattering methods. It was found out, that the potentials used in previous works are not accurate enough to allow low temperature calculations. Results from these potentials must be taken with care. Furthermore, the results from the new potential energy surface suggest significantly reduced reaction rates compared to previous numerical studies. This is in agreement with the new results of Gerlich and co-workers. Nevertheless, the large error bars in the low temperature range for experimental as well as numerical results strongly suggest refined methods to be developed for both, before a final conclusion can be made.

This work demonstrated the possibility of modern computational chemical physics to supply consistent data for spectroscopy and reaction dynamics. These are necessary and important inputs for fields like astrophysics, plasma physics and chemistry.

Appendix A - MgH

1 Rovibrational transitions

In this appendix figures are given, which show the rovibrational line oscillator strengths of the four lowest doublet states of MgH. The first R branch peak in all graphs are purely rotational transitions. Q branch transitions are forbidden by selection rule for diatomic molecules.

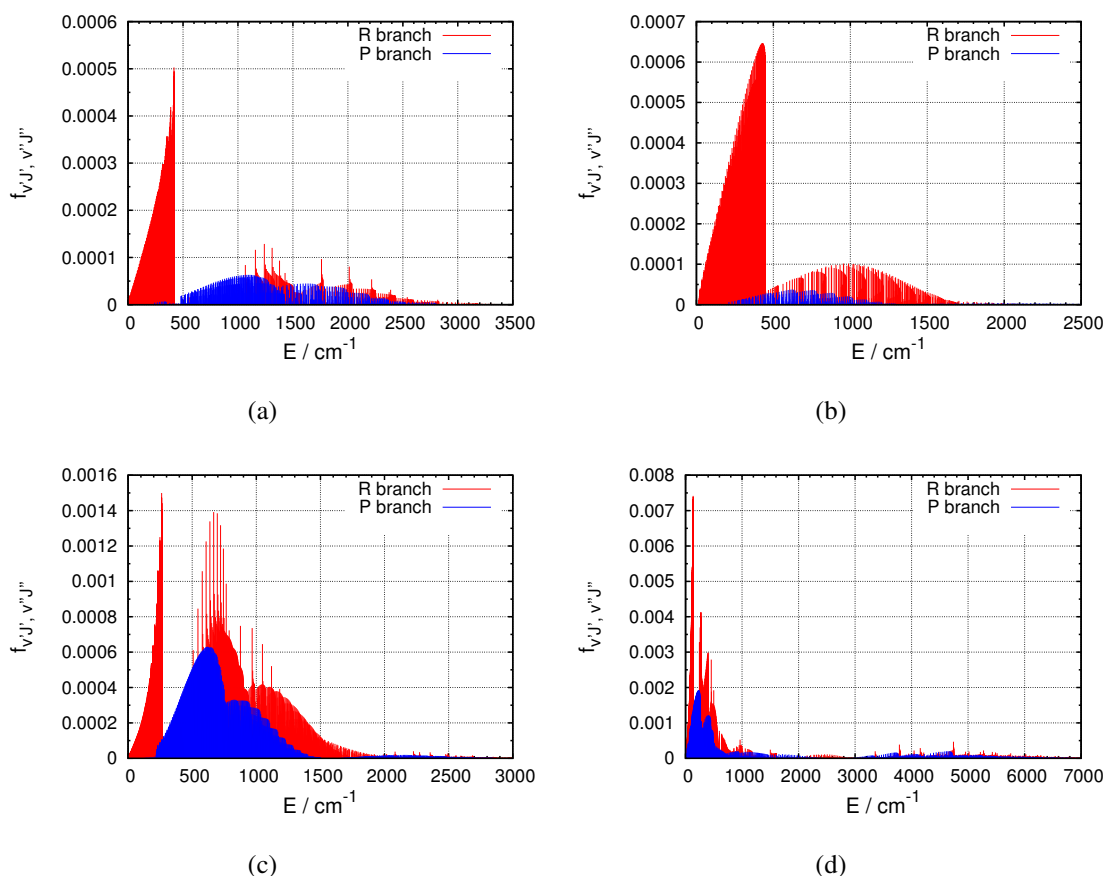


Figure 22: Rovibrational line oscillator strengths are shown for (a) $X^2\Sigma^+$, (b) $A^2\Pi$, (c) $B'^2\Sigma^+$ and (d) $E^2\Sigma^+$.

2 Photo dissociation cross sections

In this appendix figures for all calculated photodissociation cross sections are given. Each figure contains all cross sections for a pair of electronic states. For each combination of initial vibrational and rotational quantum numbers a line is drawn.

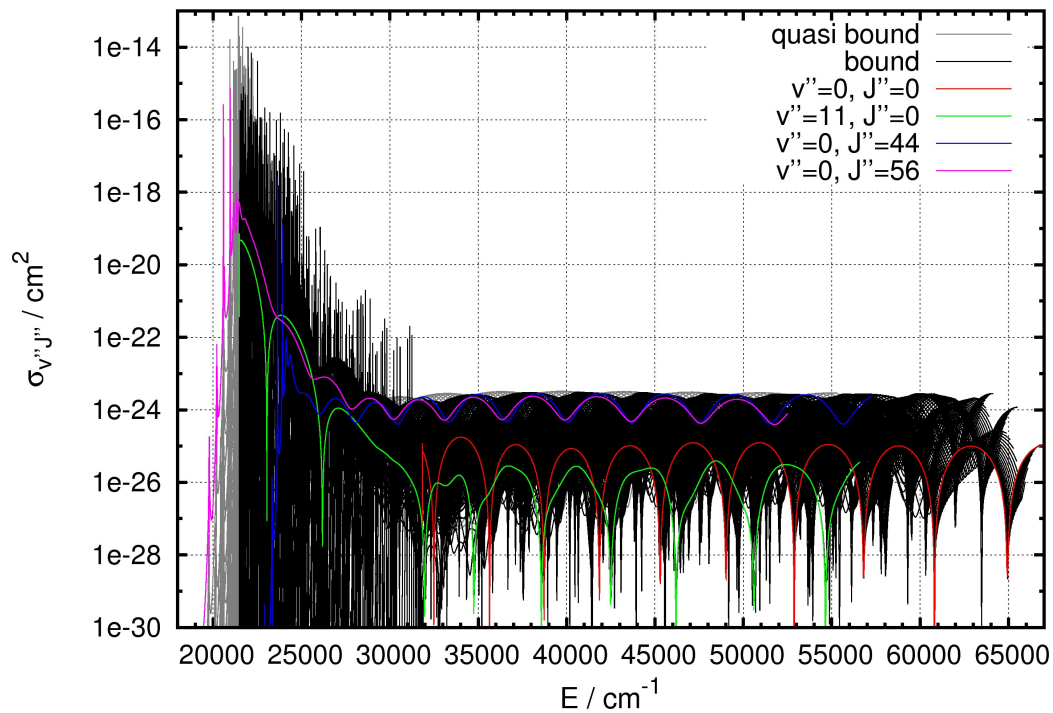
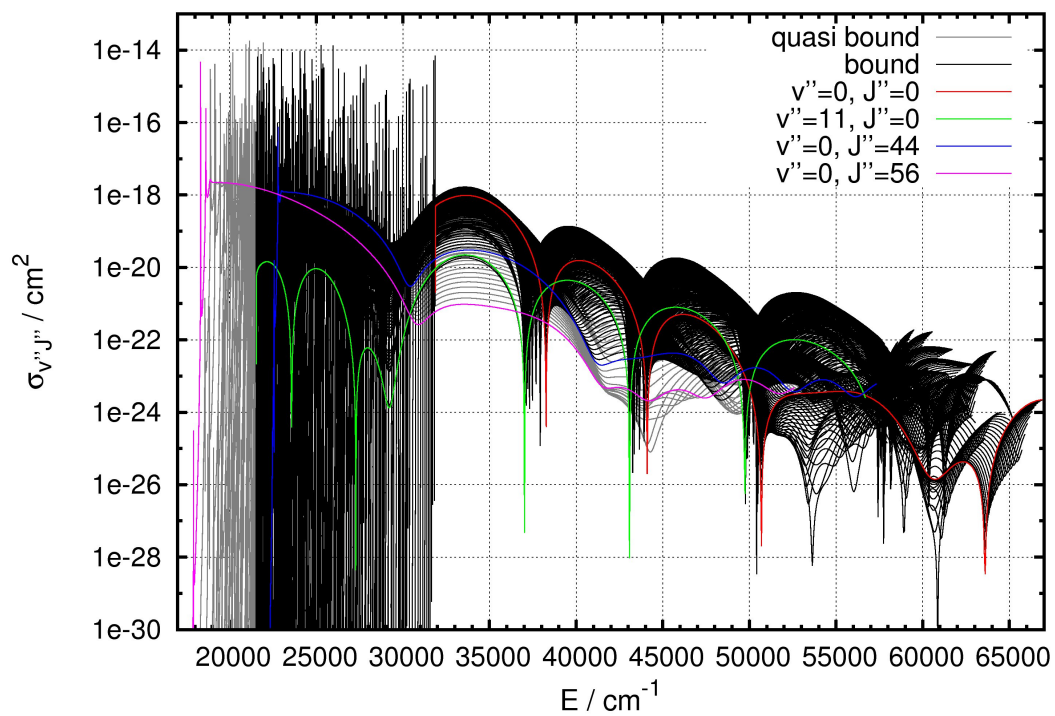
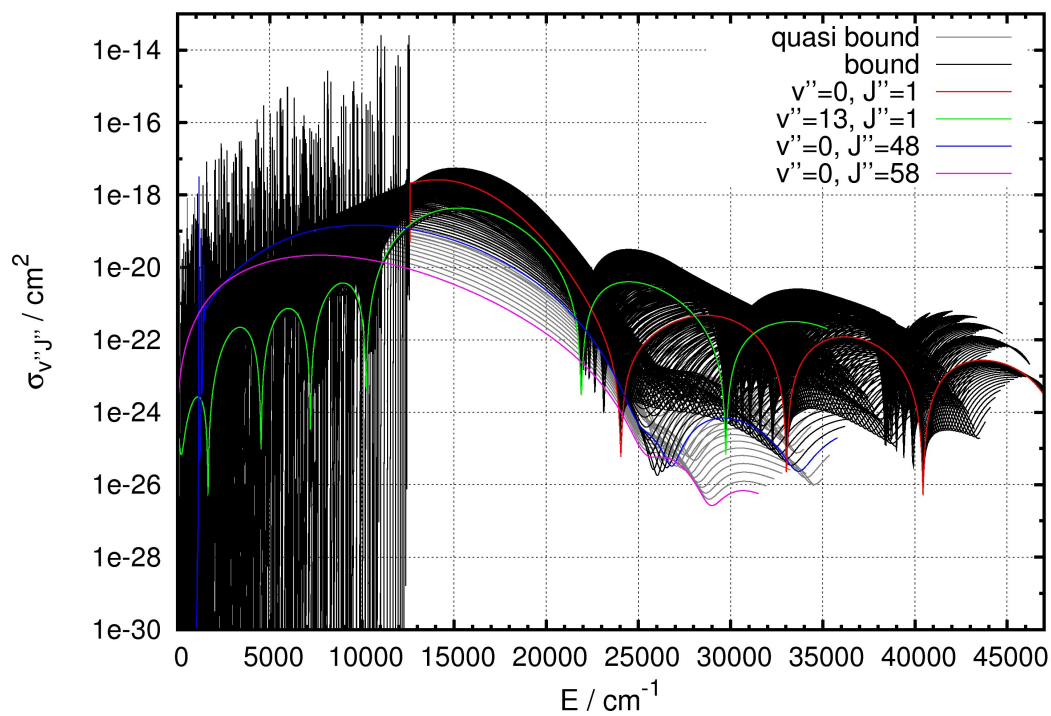


Figure 23: Photodissociation cross sections for $A^2\Pi \leftarrow X^2\Sigma^+$.

Figure 24: Photodissociation cross sections for $B'^2\Sigma^+ \leftarrow X^2\Sigma^+$.Figure 25: Photodissociation cross sections for $B'^2\Sigma^+ \leftarrow X^2\Pi$.

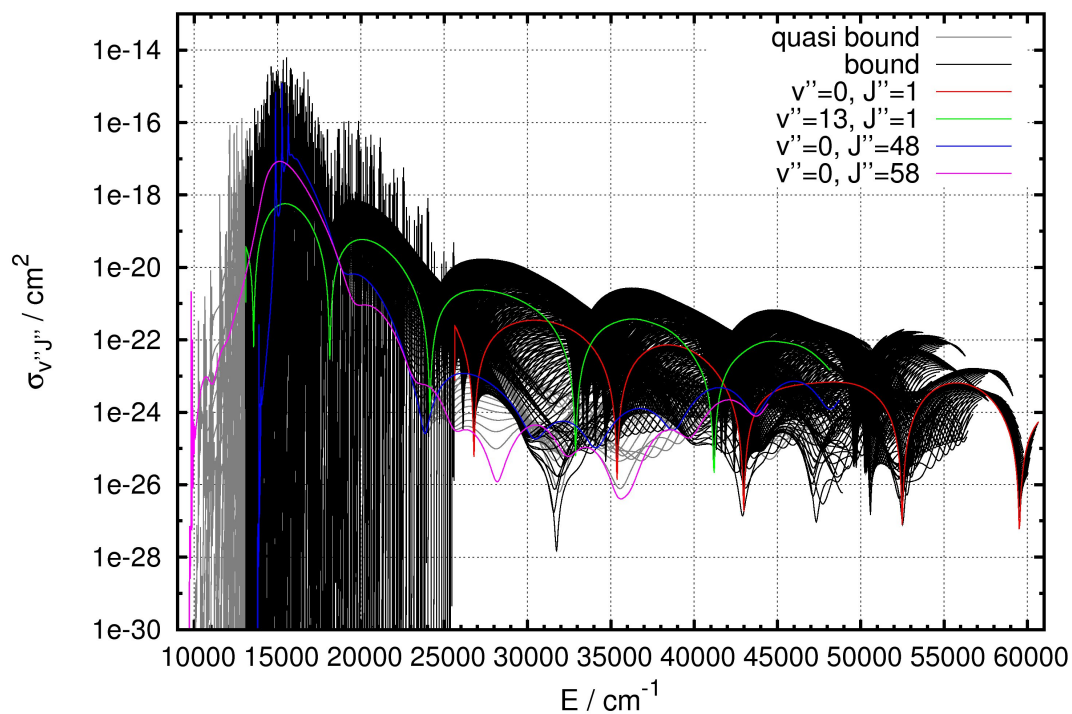


Figure 26: Photodissociation cross sections for $E^2\Sigma^+ \leftarrow A^2\Pi$.

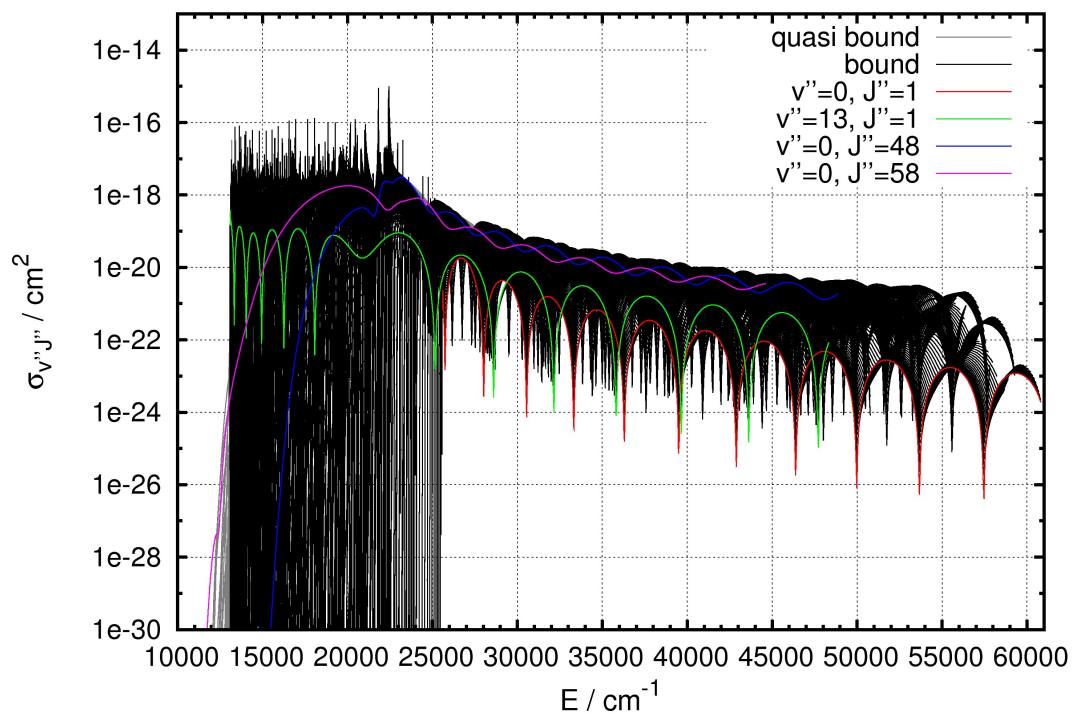
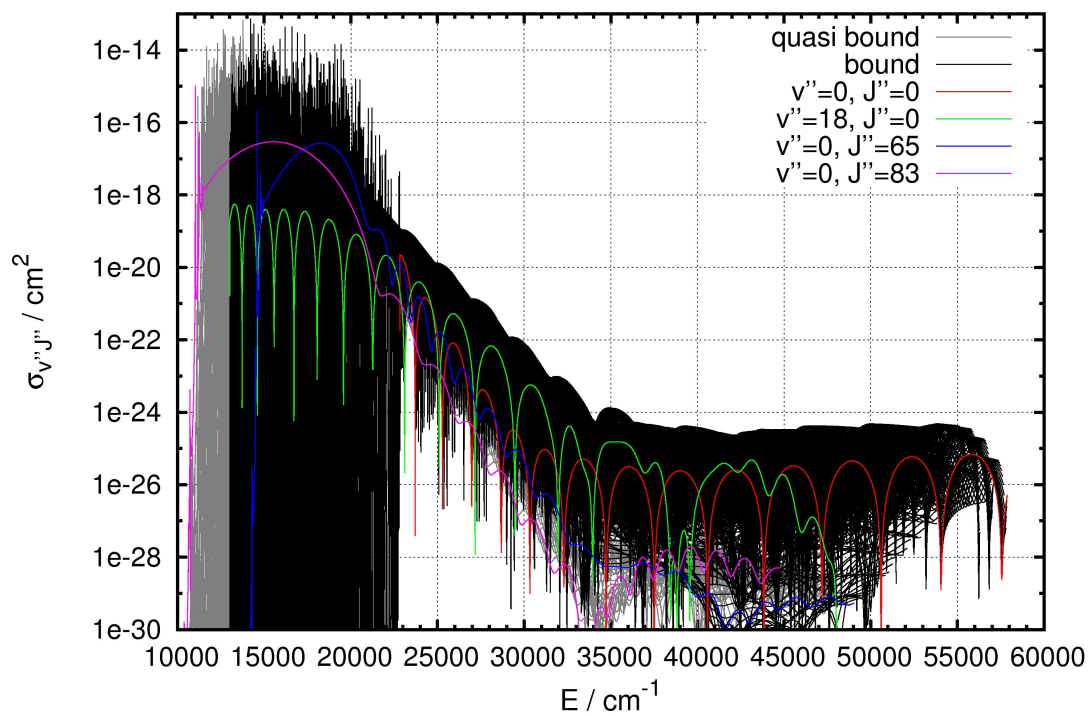
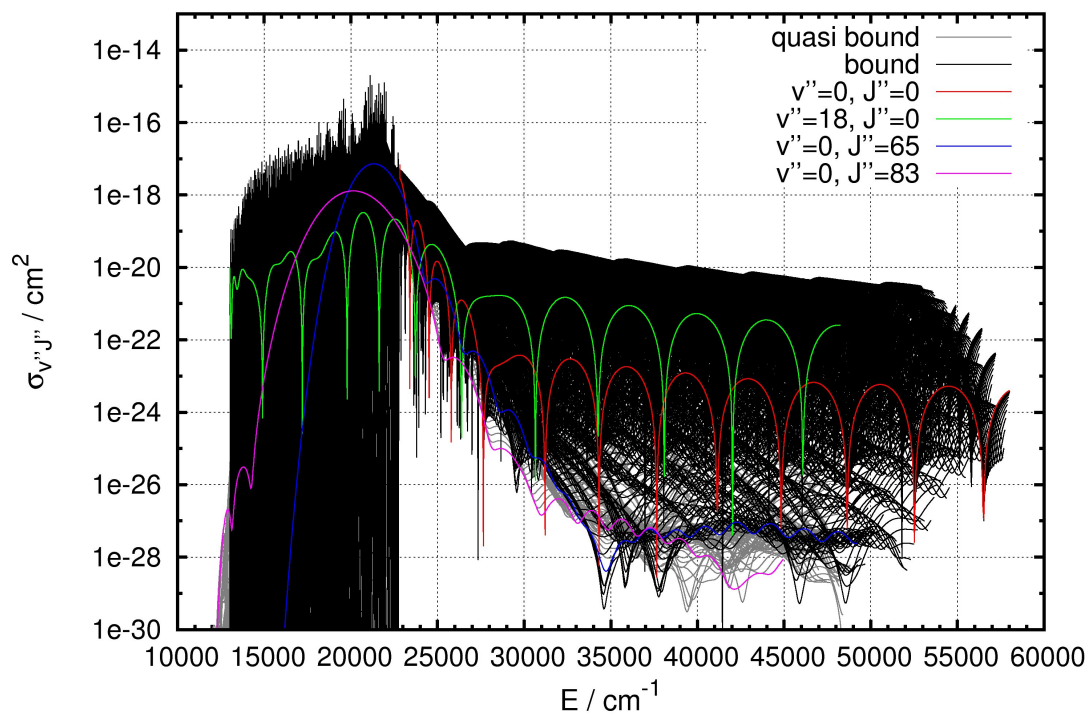


Figure 27: Photodissociation cross sections for $C^2\Pi \leftarrow A^2\Pi$.

Figure 28: Photodissociation cross sections for $B'^2\Sigma^+ \leftarrow B'^2\Sigma^+$.Figure 29: Photodissociation cross sections for $C^2\Pi \leftarrow B'^2\Sigma^+$.

Bibliography

- [1] F. Jensen, *Introduction to Computational Chemistry*, John Willey & Sons, 2nd edn, 2007.
- [2] M. Born and R. Oppenheimer, *Annalen der Physik*, 1927, **389**, 457–484.
- [3] V. Fock, *Zeitschrift für Physik A Hadrons and Nuclei*, 1930, **61**, 126–148.
- [4] J. C. Slater, *Phys. Rev.*, 1930, **35**, 210–211.
- [5] S. Boys, *Proceedings of the Royal Society of London Series A-Mathematical and Physical Sciences*, 1950, **200**, 542–554.
- [6] T. H. Dunning, *Journal of Chemical Physics*, 1989, **90**, 1007 – 1023.
- [7] D. E. Woon and J. Thom H. Dunning, *The Journal of Chemical Physics*, 1995, **103**, 4572–4585.
- [8] J. Čížek, *Journal of Chemical Physics*, 1966, **45**, 4256–4266.
- [9] O. Sinanoğlu, *Journal of Chemical Physics*, 1962, **36**, 706–717.
- [10] T. Lee and P. Taylor, *International Journal of Quantum Chemistry*, 1989, **23**, 199–207.
- [11] P. J. Knowles and H.-J. Werner, *Chemical Physics Letters*, 1985, **115**, 259 – 267.
- [12] H.-J. Werner and P. J. Knowles, *The Journal of Chemical Physics*, 1985, **82**, 5053–5063.
- [13] H.-J. Werner and P. J. Knowles, *The Journal of Chemical Physics*, 1988, **89**, 5803–5814.
- [14] P. J. Knowles and H.-J. Werner, *Chemical Physics Letters*, 1988, **145**, 514 – 522.
- [15] P. J. Knowles and H.-J. Werner, *Theoretical Chemistry Accounts: Theory, Computation, and Modeling (Theoretica Chimica Acta)*, 1992, **84**, 95–103.

- [16] X. Huang, B. J. Braams and J. M. Bowman, *Journal of Chemical Physics*, 2005, **122**, 1–12.
- [17] A. Sharma, J. Wu, B. Braams, S. Carter, R. Schneider, B. Shepler and J. Bowman, *Journal of Chemical Physics*, 2006, **125**, 224306.
- [18] D. Baye, *Journal of Physics B: Atomic, Molecular and Optical Physics*, 1995, **28**, 4399.
- [19] D. O. Harris, G. G. Engerholm and W. D. Gwinn, *The Journal of Chemical Physics*, 1965, **43**, 1515–1517.
- [20] A. S. Dickinson and P. R. Certain, *The Journal of Chemical Physics*, 1968, **49**, 4209–4211.
- [21] J. V. Lill, G. A. Parker and J. C. Light, *Chemical Physics Letters*, 1982, **89**, 483–489.
- [22] J. C. Light, I. P. Hamilton and J. V. Lill, *The Journal of Chemical Physics*, 1985, **82**, 1400–1409.
- [23] C. Schwartz, *Journal of Mathematical Physics*, 1985, **26**, 411–415.
- [24] D. Baye and P. H. Heenen, *Journal of Physics A: Mathematical and General*, 1986, **19**, 2041.
- [25] M. Vincke, L. Malegat and D. Baye, *Journal of Physics B: Atomic, Molecular and Optical Physics*, 1993, **26**, 811.
- [26] T. B. Adler, G. Knizia and H.-J. Werner, *The Journal of Chemical Physics*, 2007, **127**, 221106.
- [27] G. Knizia, T. B. Adler and H.-J. Werner, *The Journal of Chemical Physics*, 2009, **130**, 054104.
- [28] H.-J. Werner, P. J. Knowles, F. R. Manby, M. Schütz, P. Celani, G. Knizia, T. Korona, R. Lindh, A. Mitrushenkov, G. Rauhut, T. B. Adler, R. D. Amos, A. Bernhardtson, A. Berning, D. L. Cooper, M. J. O. Deegan, A. J. Dobbyn, F. Eckert, E. Goll, C. Hampel, A. Hesselmann, G. Hetzer, T. Hrenar, G. Jansen, C. Köppl, Y. Liu, A. W. Lloyd, R. A. Mata, A. J. May, S. J. McNicholas, W. Meyer, M. E. Mura, A. Nicklass, P. Palmieri, K. Pflüger, R. Pitzer, M. Reiher, T. Shiozaki, H. Stoll, A. J. Stone, R. Tarroni, T. Thorsteinsson, M. Wang and A. Wolf, *MOLPRO, version 2010.1, a package of ab initio programs*, 2010, see www.molpro.net.

-
- [29] K. A. Peterson, T. B. Adler and H.-J. Werner, *The Journal of Chemical Physics*, 2008, **128**, 084102.
- [30] J. G. Hill, S. Mazumder and K. A. Peterson, *The Journal of Chemical Physics*, 2010, **132**, 054108.
- [31] S. Alexander, C. McDonald and F. Matsen, *International Journal of Quantum Chemistry*, 1983, -, 407–414.
- [32] P. Bunker, P. Jensen, W. Kraemer and R. Beardsworth, *Journal of Chemical Physics*, 1986, **85**, 3724–3731.
- [33] A. Neugebauer and G. Häfeliinger, *INTERNATIONAL JOURNAL OF MOLECULAR SCIENCES*, 2005, **6**, 157–176.
- [34] R. Dawes, A. F. Wagner and D. L. Thompson, *Journal of Physical Chemistry A*, 2009, **113**, 4709–4721.
- [35] H.-J. Werner, P. J. Knowles, R. Lindh, F. R. Manby, M. Schütz, P. Celani, T. Korona, A. Mitrushenkov, G. Rauhut, T. B. Adler, R. D. Amos, A. Bernhardsson, A. Berning, D. L. Cooper, M. J. O. Deegan, A. J. Dobbyn, F. Eckert, E. Goll, C. Hampel, G. Hetzer, T. Hrenar, G. Knizia, C. Köppl, Y. Liu, A. W. Lloyd, R. A. Mata, A. J. May, S. J. McNicholas, W. Meyer, M. E. Mura, A. Nicklass, P. Palmieri, K. Pflüger, R. Pitzer, M. Reiher, U. Schumann, H. Stoll, A. J. Stone, R. Tarroni, T. Thorsteinsson, M. Wang and A. Wolf, *MOLPRO, version 2009.1, a package of ab initio programs*, 2009, see www.molpro.net.
- [36] J. M. Bowman, S. Carter and X. C. Huang, *International Reviews in Physical Chemistry*, 2003, **22**, 533 – 549.
- [37] S. Carter, J. Bowman and N. Handy, *Theoretical Chemistry Accounts*, 1998, **100**, 191 – 198.
- [38] A. Chakraborty, D. G. Truhlar, J. M. Bowman and S. Carter, *Journal of Chemical Physics*, 2004, **121**, 2071 – 2084.
- [39] J. Y. Wu, X. C. Huang, S. Carter and J. M. Bowman, *Chemical Physics Letters*, 2006, **426**, 285 – 289.
- [40] D. Medvedev, L. Harding and S. Gray, *Molecular Physics*, 2006, **104**, 73–81.
- [41] D. W. Schwenke, *Spectrochimica Acta Part A: Molecular and Biomolecular Spectroscopy*, 1999, **55**, 731 – 738.

- [42] C. Yamada, E. Hirota and K. Kawaguchi, *The Journal of Chemical Physics*, 1981, **75**, 5256–5264.
- [43] M. Jacox, *Journal of Physical and Chemical Reference Data*, 1994, -, 1–461.
- [44] M. Zahedi, J. A. Harrison and J. W. Nibler, *The Journal of Chemical Physics*, 1994, **100**, 4043–4055.
- [45] S. Davis, D. T. Anderson, G. Duxbury and D. J. Nesbitt, *The Journal of Chemical Physics*, 1997, **107**, 5661–5675.
- [46] X. Wang and T. Carrington, *Journal of Chemical Physics*, 2003, **119**, 101 – 117.
- [47] R. Warmbier, R. Schneider, A. R. Sharma, B. J. Braams, J. M. Bowman and P. H. Hauschildt, *Astronomy & Astrophysics*, 2009, **495**, 655–661.
- [48] E. Venuti, L. Halonen and R. Della Valle, *Journal of Chemical Physics*, 1999, **110**, 7339–7347.
- [49] J. Hilico, O. Robert, M. Loete, S. Toumi, A. Pine and L. Brown, *Journal of Molecular Spectroscopy*, 2001, **208**, 1–13.
- [50] R. Georges, M. Herman, J.-C. Hilico and O. Robert, *Journal of Molecular Spectroscopy*, 1998, **187**, 13 – 20.
- [51] P. H. Hauschildt, R. Warmbier, R. Schneider and T. Barman, *Astronomy & Astrophysics*, 2009, **504**, 225–229.
- [52] D. Schwenke and H. Partridge, *Spectrochimica Acta Part A-Molecular and Biomolecular Spectroscopy*, 2001, **57**, 887–895.
- [53] L. Rothman, D. Jacquemart, A. Barbe, D. Benner, M. Birk, L. Brown, M. Carleer, C. Chackerian, K. Chance, L. Coudert, V. Dana, V. Devi, J. Flaud, R. Gamache, A. Goldman, J. Hartmann, K. Jucks, A. Maki, J. Mandin, S. Massie, J. Orphal, A. Perrin, C. Rinsland, M. Smith, J. Tennyson, R. Tolchenov, R. Toth, J. Vander auwera, P. Varanasi and G. Wagner, *Journal of Quantitative Spectroscopy & Radiative Transfer*, 2005, **96**, 139 – 204.
- [54] L. S. Rothman, I. E. Gordon, A. Barbe, D. C. Benner, P. E. Bernath, M. Birk, V. Boudon, L. R. Brown, A. Campargue, J. P. Champion, K. Chance, L. H. Coudert, V. Dana, V. M. Devi, S. Fally, J. M. Flaud, R. R. Gamache, A. Goldman, D. Jacquemart, I. Kleiner, N. Lacome, W. J. Lafferty, J. Y. Mandin, S. T. Massie, S. N. Mikhailenko, C. E. Miller, N. Moazzen-Ahmadi, O. V. Naumenko, A. V. Nikitin,

- J. Orphal, V. I. Perevalov, A. Perrin, A. Predoi-Cross, C. P. Rinsland, M. Rotger, M. Simeckova, M. A. H. Smith, K. Sung, S. A. Tashkun, J. Tennyson, R. A. Toth, A. C. Vandaele and J. Vander Auwera, *Journal of Quantitative Spectroscopy & Radiative Transfer*, 2009, **110**, 533–572.
- [55] R. A. Kendall, J. Thom H. Dunning and R. J. Harrison, *The Journal of Chemical Physics*, 1992, **96**, 6796–6806.
- [56] A. Shayesteh, R. D. E. Henderson, R. J. Le Roy and P. F. Bernath, *Journal of Physical Chemistry A*, 2007, **111**, 12495–12505.
- [57] M. Larsson, *Astronomy and Astrophysics*, 1983, **128**, 291–298.
- [58] H. Hönl and F. London, *Zeitschrift für Physik*, 1925, **33**, 803–809.
- [59] A. Hansson and J. Watson, *Journal of Molecular Spectroscopy*, 2005, **233**, 169–173.
- [60] W. Balfour and H. Cartwright, *Chemical Physics Letters*, 1975, **32**, 82–85.
- [61] W. Balfour and H. Cartwright, *Canadian Journal of Physics*, 1976, **54**, 1898–1904.
- [62] W. Balfour and B. Lindgren, *Canadian Journal of Physics*, 1978, **56**, 767–779.
- [63] S. Skory, P. Weck, P. Stancil and K. Kirby, *Astrophysical Journal Supplement Series*, 2003, **148**, 599–606.
- [64] P. Weck, A. Schweitzer, P. Stancil, P. Hauschildt and K. Kirby, *Astrophysical Journal*, 2003, **582**, 1059–1065.
- [65] R. P. Saxon, K. Kirby and B. Liu, *The Journal of Chemical Physics*, 1978, **69**, 5301–5309.
- [66] P. Weck, A. Schweitzer, P. Stancil, P. Hauschildt and K. Kirby, *Astrophysical Journal*, 2003, **584**, 459–464.
- [67] P. Weck, P. Stancil and K. Kirby, *Astrophysical Journal*, 2003, **582**, 1263–1268.
- [68] E. Picazzio, A. De Almeida, S. M. Andrievskii, K. I. Churyumov and I. V. Luk'yanyk, *Proceedings of Asteroids*, 2002, pp. 713–716.
- [69] A. E. Douglas and G. Herzberg, *Astrophysical Journal*, 1941, **94**, 381.
- [70] B. Godard, E. Falgarone and G. P. des Forets, *Astronomy & Astrophysics*, 2009, **495**, 847–867.
- [71] J. Black, *Faraday Discussions*, 1998, **109**, 257–266.

- [72] T. Stoecklin and P. Halvick, *Phys Chem Chem Phys*, 2005, **7**, 2446–2452.
- [73] P. Halvick, T. Stoecklin, P. Larrgaray and L. Bonnet, *Phys. Chem. Chem. Phys.*, 2007, **9**, 582–590.
- [74] R. Plasil, T. Mehner, P. Dohnal, T. Kotrik, J. Glosik and D. Gerlich, submitted.
- [75] D. Gerlich, G. Borodi, A. Luca, M. C. and M. A. Smith, *Zeitschrift für Physikalische Chemie*, 2011, **225**, 475–492.
- [76] private communication with D. Gerlich.
- [77] R. Warmbier and R. Schneider, *Phys. Chem. Chem. Phys.*, 2011, **13**, 10285–10294.
- [78] K. M. Ervin and P. B. Armentrout, *The Journal of Chemical Physics*, 1986, **84**, 6750–6760.
- [79] C. W. Gear, *Communications of the ACM*, 1966, **9**, 475–&.
- [80] L. Bonnet and J. C. Rayez, *Chemical Physics Letters*, 2004, **397**, 106–109.
- [81] L. Bonnet and J. C. Rayez, *Chemical Physics Letters*, 1997, **277**, 183–190.
- [82] L. Bonnet and C. Crespos, *Phys. Rev. A*, 2008, **78**, 062713.
- [83] L. Bonnet and C. Crespos, *Phys. Rev. A*, 2009, **80**, 059903.
- [84] R. A. Marcus, *The Journal of Chemical Physics*, 1971, **54**, 3965–3979.
- [85] W. H. Miller, *Adv. Chem. Phys.*, 1974, **25**, 69.
- [86] W. H. Miller, *The Journal of Physical Chemistry A*, 2001, **105**, 2942–2955.
- [87] D. Skouteris, J. F. Castillo and D. E. Manolopoulos, *Computer Physics Communications*, 2000, **133**, 128–135.
- [88] G. C. Schatz, *Chemical Physics Letters*, 1988, **150**, 92 – 98.
- [89] G. A. Parker and R. T. Pack, *The Journal of Chemical Physics*, 1993, **98**, 6883–6896.
- [90] L. M. Delves, *Nuclear Physics*, 1958-1959, **9**, 391 – 399.
- [91] R. T. Pack and G. A. Parker, *The Journal of Chemical Physics*, 1987, **87**, 3888–3921.
- [92] D. Neuhasuer and M. Baer, *The Journal of Chemical Physics*, 1989, **90**, 4351–4355.
- [93] N. Sathyamurthy, *Chemical Reviews*, 1983, **83**, 601–618.

- [94] L. B. Harding, R. Guadagnini and G. C. Schatz, *The Journal of Physical Chemistry*, 1993, **97**, 5472–5481.
- [95] A. Luca, G. Borodi and D. Gerlich, *Photonic, Electronic and Atomic Collisions*, 2006, pp. 494–501.
- [96] W. Federer, H. Villinger, F. Howorka, W. Lindinger, P. Tosi, D. Bassi and E. Ferguson, *Phys. Rev. Lett.*, 1984, **52**, 2084–2086.
- [97] W. Federer, H. Villinger, P. Tosi, D. Bassi, E. Ferguson and W. Lindinger, in *Molecular Astrophysics*, ed. G.H.F. Dierksen *et al.*, D. Reidel Publishing Company, 1985, ch. Laboratory studies of ion reactions with atomic hydrogen, p. 649.

Declaration

I hereby declare that this work has so far neither been submitted to the Faculty of Mathematics and Natural Sciences at the Ernst-Moritz-Arndt-University of Greifswald nor to another scientific institution for the purpose of the degree of doctorate. Furthermore, I declare that I have written this work by myself and that I have not used any other resources, other than mentioned earlier in this work.

Hiermit erkläre ich, dass diese Arbeit bisher von mir weder an der Mathematisch-Naturwissenschaftlichen Fakultät der Ernst-Moritz-Arndt-Universität Greifswald noch einer anderen wissenschaftlichen Einrichtung zum Zwecke der Promotion eingereicht wurde. Ferner erkläre ich, dass ich diese Arbeit selbständig verfasst und keine anderen als die darin angegebenen Hilfsmittel benutzt habe.

Robert Warmbier

Curriculum Vitae

Personal Data

Name	Robert Warmbier
Date of Birth	28 August 1984
Place of Birth	Stralsund, Germany
Marital Status	Unmarried
Address	Rossmühlenstrasse 7, 17489 Greifswald, Germany
Email	Robert.Warmbier@ipp.mpg.de

Education

Since 2008	PhD student at the International Max Planck Research School on Bounded Plasmas, Max-Planck-Institute for Plasma Physics, Greifswald, Germany
2003-2008	Study of Physics (Diplom) at the Ernst-Moritz-Arndt University Greifswald, Germany
1995-2003	Ostsee-Gymnasium Sassnitz, Germany

Scientific Career

Since 2008	Research assistant and PhD student at the Max-Planck-Institute for Plasma Physics, Greifswald, Germany
-------------------	--

Acknowledgements

I want to take the chance and thank all the people supporting me in the last three years. First of all, I want to thank my supervisor Ralf Schneider for his advise and the coffee. He was always helpful in discussions and never lost his patience with me. I also want to thank all the members of the COMAS group. A good working atmosphere, help, discussions and procrastination were very important to me.

Working alone is a difficult task. Therefore, I want to give special thanks to my collaborators Amit R. Sharma, Bastiaan J. Braams, Peter Hauschildt, Joel Bowman and Stuart Carter.

Not forgotten shall be my girlfriend Maria, my family and friends who were always supporting me.

And last but not least, I want to thank Ralf, Maria, Abha and Lars for reading the thesis and for their input.